The Dissertation Committee for Tomas Neil Capaldi Certifies that this is the approved version of the following Dissertation:

Stratigraphic response to Cordilleran Processes along the South Central Andean Margin

Committee:

Brian Horton, Supervisor

Peter Flaig

Mark Helper

Ryan McKenzie

Ronald Steel

Daniel Stockli

Stratigraphic response to Cordilleran Processes along the South Central Andean Margin

by

Tomas Neil Capaldi

Dissertation

Presented to the Faculty of the Graduate School of

The University of Texas at Austin

in Partial Fulfillment

of the Requirements

for the Degree of

Doctor of Philosophy

The University of Texas at Austin

AUGUST, 2019

Dedication

This work is dedicated to the late Mavis Archer.

She knew this was going to happen before any of us did.

Acknowledgements

There are many people to thank in inspiring and helping me through the challenging but rewarding years of my PhD. My drive to understand Earth's long and complicated history is thanks to Mike and the Creation Study group and their welcoming setting to deliberate Earth's origin. I thank Sinan Akciz, Ray Ingersoll, Ed Rhodes, and An Yin for being supportive, imaginative mentors at UCLA, who pushed me to be the best scientist I could. Additionally, to all the 4th and 5th floor ESS grad students: Dallon Stang, Peter Haproff, Nate Brown, Kevin Coffey, Andrew Zuza, Robbin Zuza, Mike Lawson, Evan Wolf, John Merring, and Chris McGuirre and for all the roof top conversations, dark lab help, and tricking me into graduate school. My mapping partner Bill Pepper who got me through the Poleta summer. At Texas I was around some of the greatest people and minds who have built a community I am so lucky to be a part of. This includes thanking the Stratigraphy and Tectonics grad students Kelly Thomson, Emily Cooperdock, Cody Lee Colleps, Evan Ramos, Ben Smith, Jake Makis, Michelle Gevedon, Mike Prior, Nikki Seymour, Renas Koshnaw, Ben Cardenas, Spencer Semen, Nick Perez, Edgardo Pujols, Scott Eckley, Jasmin Mason, Cullen Kortyna, Carolyn Tewksbury-Christle, Peter Gold, Sam Robbins, Sol Cooperdock, Alissa Kotowski, Hima Gutipadi, and Adam Goldsmith, whose scientific debates at Double Dave's and Crown shaped my PhD ideas. To the many excellent faculty, I interacted and taught with over all those summers, especially Mark Helper who has shown me how to me an effective teacher and leader. My committee members Ryan McKenzie, Danny Stockli, Peter Flaig, Ron Steel, and Mark Helper for letting me run wild with ideas but also for keeping me grounded and sane. I thank a thousand times over my academic sisters Meredith Bush, Kristina Butler, Amanda Calle, Sarah George, Gabby Gutierrez, Lily Jackson, and Chelsea Mackaman-Lofland for all the

help and conversations in Monday group meetings, at Growler, in Barbs, and on mountains. A special thanks to my advisor Brian Horton who gave me shot when no one else would, and showed me how to be a researcher, field geologist, writer, instructor, public speaker, but not a punker. I thank my family for all their love and always encouraging me to follow my passion. But none of this would have been possible without my better half Margo. She spent countless days helping me in the spooky sections, being a plasma whisperer, editing and reediting word docs, being my cheerleader, and traveling across the world with me. I will forever and always thank her for all her love.

Abstract

Stratigraphic response to Cordilleran Processes along the South Central Andean Margin

Tomas Neil Capaldi, Ph.D.

The University of Texas at Austin, 2019

Supervisor: Brian K. Horton

Subduction zones along convergent plate margins are fundamental components of Earth systems that link mountain building, magmatism, lithospheric dynamics, surface processes, and climate-carbon cycles. Resolving the feedbacks and relationships among these components has been a longstanding challenge in Earth science with broad implications for understanding coupling among rheology, deformation, and erodibility. The sedimentary record within convergent systems provide a unique opportunity to understand long-lived Cordilleran processes between subduction, magmatism, erosion, sediment routing, and deposition. This dissertation investigates the Phanerozoic to present sedimentary record to address the dynamic interactions among Earth-surface processes and lithospheric processes throughout a complex tectonic history along the Andean Cordilleran margin of Argentina.

Chapter 1 applies detrital zircon U-Th-Pb and Lu-Hf isotopic datasets as a powerful methods for evaluating long-term, regional geologic patterns and the processes of crustal addition, removal, and recycling to help resolve the onset of Andean subduction, and the

relationships and feedbacks among upper-and lower-plate processes, and the timescales of Cordilleran evolution. A large Phanerozoic compilation of new and published zircon data provides new insights into how changes in the subducted lower-plate are fundamental drivers to magmatism composition, spatial patterns, and deformation. This chapter will be submitted to *Geosphere* with coauthors Ryan McKenzie, Brian Horton, Chelsea Mackaman-Lofland, and Daniel Stockli.

Chapter 2 integrates field measurements with a large detrital geochronology datasets to establish a lithostratigraphic and chronostratigraphic record of Neogene Andean flat-slab subduction. Coeval cycles of upward coarsening stratigraphic trends, erosional unroofing, deformation, and magmatic high flux events provides new evidence of upper-plate Cordilleran feedbacks driven by changes in subduction regime. This chapter will be submitted to *Tectonics* with coauthors Brian Horton, Chelsea Mackaman-Lofland, Ryan McKenzie, Daniel Stockli, Gustavo Ortiz, and Patricia Alvarado.

Chapter 3 uses detrital zircon from modern river sands to understand how landscapes respond to variation in bedrock erosion, structural setting, drainage network, and transport processes. This chapter provides new tools and geologic understandings to arm future researchers attempting to studying sedimentary provenance in convergent margins settings. This chapter was published in *Earth and Planetary Science Letters* in December, 2017 with coauthors Brian Horton, Ryan McKenzie, Daniel Stockli, and Margo Odlum.

Table of Contents

List of Tables

List of Figures

CHAPTER 1: CORDILLERAN MAGMATISM AND GEODYNAMIC EVOLUTION OF THE WESTERN SOUTH AMERICAN PLATE MARGIN

ABSTRACT

Phanerozoic subduction along the western South American margin provides valuable insights into the temporal and spatial distribution of magmatism and associated isotopic patterns during major shifts in Cordilleran plate dynamics. Detrital zircon U-Th-Pb and Hf isotopic results throughout the continental arc systems of Chile-Argentina (28-33°S) are integrated with bedrock geochronology to define distinct spatial and isotopic trends synchronous with changes in continental margin configuration during (1) Cambrian to Ordovician terrane accretion, (2) mid-Paleozoic arc-cessation, (3) Carboniferous-Permian subduction initiation, (4) Permian-Jurassic continental back-arc rifting, (5) Cretaceous-Paleogene Andean retro-arc shortening, and (6) Neogene flat-slab subduction. The 550 Myr record of arc magmatism provides new constraints on radiogenic isotopic trends, patterns in arc tempo, and role of subduction angle on over-ridding plate processes. Magmatism east of -69 longitude exhibit radiogenic isotopic signatures indicative of reworked continental lithosphere with evolved (negative) εHf values, low (< 0.65) zircon Th/U ratios during phases of contraction. In contrast, magmatism west of -69 long displays juvenile (positive) εHf values and high (>0.7) zircon Th/U values recording increased asthenospheric contribution during extension. Progressive continental arc broadening and subduction angle shallowing initiated by the Late Cretaceous, and corresponds with an

increase in arc magmatism tempo from Paleozoic-Mesozoic 45-60 Myr phases of high arc activity and 25 Myr lulls, to Cenozoic 25 Myr magmatic flare ups and negligible magmatic lulls (<5 Myr). New temporal, spatial, and isotopic constraints on Phanerozoic subduction indicate a complex geodynamic evolution that includes (1) accelerated relative convergence following the Jurassic to Cretaceous opening of the South Atlantic; (2) far field effects from the subduction of positively buoyant oceanic lithosphere; with (3) implications for Cordilleran cyclicity and prolonged (>200 Myr) slab anchoring into the lower mantle. New constraints from detrital zircon radiometric isotopes from the Andean subduction margin can provide tools to test proposed tectonic models of ancient subduction settings.

INTRODUCTION

Subduction zones along convergent plate margins are fundamental components of Earth systems that link mountain building, magmatism, lithospheric dynamics, surface processes, and the climate-carbon cycles. In Cordilleran or Andean orogenic systems, the dynamics of ocean-continent subduction can induce coupled interactions between the subducting lower plate and overriding upper plate, with implications for tectonic regime, deformation modes, and associated sedimentary basin evolution (Dickinson, 2004; Ramos, 2009; Ingersoll, 2011; Yonkee and Weil, 2015; Horton, 2018a; Fig. 1). Recent studies describing the mechanism that drive Cordilleran evolution include Cordilleran Cyclicity Model involving feedbacks among magmatism and the orogenic wedge to occur cyclically over 30-40 Myr (Haschke et al., 2002; 2006; DeCelles et al., 2009; 2015). Recent

geodynamics models predict overriding plate response to the down-going plate interacting and anchoring into the lower mantel by shortening progressively on 50 to 200 myr timescales from anchoring to orogenesis. (Faccena et al., 2017; Schellart et al., 2017; Chen et al., 2019). The relative angle of subduction dictates the degree of mechanical coupling between the over-ridding plate and down-going plate (Heuret and Lallemand, 2005; Ramos, 2010; Martinod et al., 2010; Horton, 2018b).

The evolution of Cordilleran-type orogens is sensitive to variations in both lower plate and upper plate processes, and manifest as spatial, temporal, and compositional changes in continental arc magmatism (Kay and Mpodozis, 2002; Haschke et al., 2002, 2006; Kirsch et al., 2016; deSilva and Kay; 2018). Combined detrital zircon U-Th-Pb and Hf isotopic datasets, represent powerful tools for evaluating long-term, regional geologic patterns and the processes of crustal addition, removal, and recycling that, in turn help resolve the onset of Andean subduction, the relationships and feedbacks among upper-and lower-plate processes, and the timescales of Cordilleran evolution (Fig. 1). Evaluating the operative spatial and temporal scales of arc magmatism provides a means to test proposals of high-flux events (HFEs) and magmatic lulls that may generate cyclical or punctuated arc tempos at regular or irregular recurrence intervals (deSilva et al., 20; Patterson, et al.,). Zircon Th/U values can serve, in part, as proxies for tectonic regime, with elevated Th/U (>1.0) broadly correlative with extensional phases and low Th/U (0.1-1.0) correspond to contractional phases of orogenesis (Barth et al., 2013; McKay et al., 2018). Additionally, studies have shown that low zircon Th/U ratios (<0.10) are likely associated with metamorphic crystallization, and that zircon Th/U increases with decreasing host rock

SiO2 content, such that zircon from granitic rocks have distinctly lower (between 0.55 and 0.80) ratios, whereas zircon from gabbroic rocks has Th/U ratios that are largely higher (between 0.8 and 1.2; Kirkland et al., 2015; Yakymchuk et al., 2018). Zircon Hf isotopic signatures can record positive εHf values that reflect juvenile crustal material originating from melts of primitive mantle origin, or negative εHf values indicative of melts derived from older recycled crustal material (Hildreth and Moorbath, 1988; Belousova et al., 2002; Kemp et al., 2009). Using magmatism bedrock age and location datasets provides constraints on continental arc width which can be inverted to calculate an estimate on subduction angle width (Fig. 1).

The Andes represent one of the few places on Earth where a long-lived (>200 Myr) continuous subduction has provided the geologic record necessary to constrain the spatial and temporal relationships among geodynamic processes, upper-plate deformation, and magmatism. Previous studies have focused on Andean magmatic records that span from inferred Early Jurassic (~200 Ma) initiation to present (Haschke et al., 2002, 2006; Folguera and Ramos, 2011; Kirsch et al., 2016; Balgord, 2017; Butler et al., in press; George et al., in press). This study presents and leverages a comprehensive detrital zircon geochronological and isotopic dataset for grains ranging in age from Neoproterozoic to Neogene to evaluate a longer magmatic record that spans the entire Phanerozoic. These data allow for assessment of: (1) the timing of subduction initiation and Cordilleran-type margin development along the Central to Southern Andean segment of western South America and (2) the feedbacks and relationships among subduction processes, upper-plate deformation, and isotopic signatures, and (3) the timescales of Cordilleran evolution. We

investigated the detrital zircon record from strata in the southern Central Andes of Argentina and Chile to determine how the Andean margin evolved through time (Fig. 1).

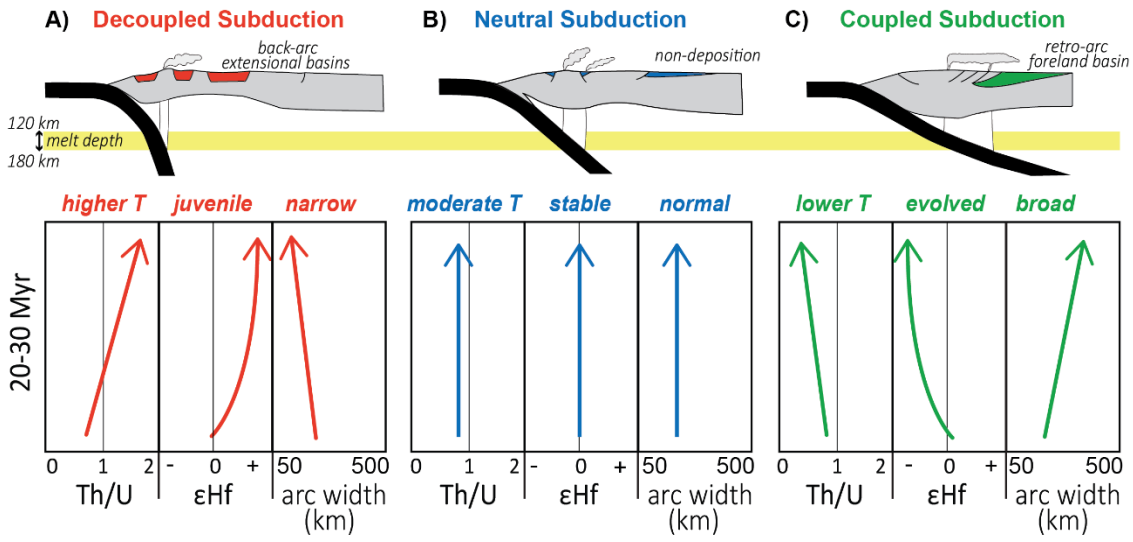

Figure 1.1: Comparison diagrams for schematic lithospheric-scale cross-sections for contrasting subduction regimes across a Cordilleran margin, with variable tectonic setting, subduction angle, continental arc width, and zircon radiogenic isotopic signatures (i.e. Th/U and ƐHf values). (A) Slab steepening settings are predicted to exhibit back-arc extension over 20-30 Myr with magmatic zircons to yield high (>1) Th/U values and juvenile (positive) ƐHf values across a narrow (<100 km) continental arc. (B) Neutral subduction over 20-30 Myr have predicted magmatic zircons to yield moderate (0.6-1) Th/U values and stable (positive-negative) ƐHf values across a normal continental arc width (~100 km). (C) Coupled subduction during slab shallowing over 20-30 Myr is predicted to yield crustal shortening with magmatic zircons (< 0.8) Th/U values and evolved (negative) ƐHf values across a broad continental arc width (>200 km).

GEOLOGIC FRAMEWORK

The Andes of west-central Argentina and Chile (28-33°S) record long-lived magmatism along the western margin of the South American plate (Fig. 2). The corresponding rock record can be divided into three distinct groups: (1) Precambrian-Ordovician; (2) Carboniferous-Triassic, and (3) Jurassic-Neogene igneous and associated metamorphic rocks.

(1) Precambrian to Ordovician igneous and metamorphic belts are preserved in the Andean foreland in eastern Sierras Pampeanas. Crystallization ages ranging from Pampean (555-515 Ma) and Famatinian (495-460 Ma) arc magmatism during eastward dipping subduction of oceanic crust (Ramos et al., 1989; Bahlburg et al., 2009). Subduction initiated by 555 Ma generated a calc-alkaline magmatic belt (555-525 Ma) that intruded quartzo-feldspathic metasedimentary rocks and semi-pelitic schist. After a proposed ridge trench collision (~525 Ma), arc magmatism shut off and hot asthenospheric mantle juxtaposed against the base of the accretionary prism produced short-lived, mafic volcanism followed by intrusions of peraluminous granitoids (525-515 Ma) into amphibolite to granulite facies metasedimentary rocks (Schwartz et al., 2008). The Cambrian-Ordovician Famatinian arc (495-460 Ma) produced intermediate to felsic calc-alkaline magmas from hybridization with mantle-derived melts and supra-crustal components (Ducea et al., 2010). Theses Precambrian to Ordovician belts have been interpreted as the product of accretion of Laurentian derived terranes to the Gondwana margin (Schwartz et al., 2008; Ducea, et al., 2010; Thomas et al., 2015; Rapela, et al., 2016).

(2) Carboniferous-Triassic igneous complexes form a large component of the High Andes, including the Choiyoi igneous complex that spans the Principal Cordillera along the Chile-Argentina border, as well as flanking regions to the west (Chilean Precordillera) and east (Frontal Cordillera and parts of the Andean foreland). Crystallization ages from Frontal Cordillera Elqui–Limarí and Chollay batholiths yield four discrete pulses Mississippian (330-326 Ma), early Permian (300-285 Ma), late Permian-Middle Triassic (265-242 Ma) and Upper Triassic (225-215 Ma) (Hervé et al., 2014). Additionally, concurrent Choiyoi Igneous Province volcanism range from 280 to 248 Ma (Kleinman and Japas, 2009). Late Carboniferous to Early Permian subduction initiation is synchronous with the San Rafael orogeny that generated compressional structures along a NW-NNW-trending orogenic belt and peraluminous plutons and mid-Permian calc-alkaline continental arc magmas (Hervé et al., 2014; Giambiagi et al., 2014). Emplacement of calc-alkaline to alkaline bi-modal intrusive suites and exceptionally thick (>5-10 km) ignimbrites after the cessation of shortening and crustal thickening associated with the late Paleozoic Gondwanide orogeny is consistent with crustal melting and possible post-orogenic collapse prior to and during the earliest stages of Gondwana breakup (Mpodozis and Kay, 1992; Kleinman and Japas, 2009).

(3) Jurassic-Neogene igneous arc rocks across Chile and western Argentina include principally granitic and granodioritic intrusions and andesite extrusive counterparts associated with development of the Andean magmatic arc. Mesozoic magmatism in Chile is recorded by the Early Jurassic Limarí and Papudo-Quintero complexes (200-165 Ma), the Cretaceous Illapel Complex (130-90 Ma), the Paleocene to Eocene Cogotí Supergroup

(67-38 Ma), the Eocene to Oligocene Doña Ana Group (27-18 Ma), and the volcanic rocks of the Miocene Cerro de las Tortolas Formation (17-10 Ma) (Parada et al., 1988; 1999; Kay et al., 1991; Jones et al., 2016). The igneous rocks occupy an area from the present-day coastal regions to the Neogene magmatic arc along the Chile-Argentina border, and show a systematic decrease in age from west to east (Haschke et al., 2006). The location, composition, and age patterns are consistent with arc magmatism linked to east-dipping subduction of oceanic plates of Pacific affinity. In this segment of western South America, Cordilleran magmatism was generated during fluctuating phases of extension, stasis, and shortening (Charrier et al., 2015; Horton and Fuentes, 2016; Mackaman-Lofland et al., 2019).

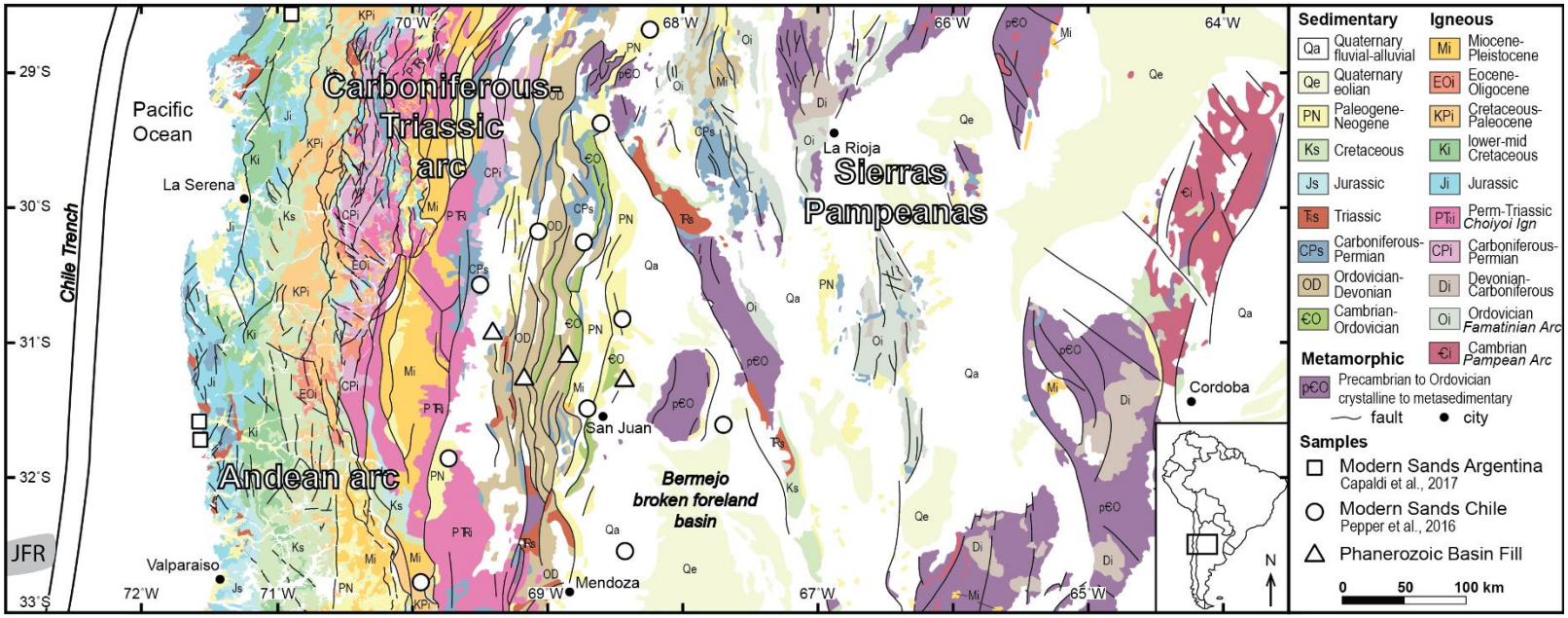
Pacific Ocean
Chile Trench
JFR
Carboniferous-Triassic arc
Andean arc
Sierras Pampeanas
Bermejo broken foreland basin
La Serena
Valparaiso
San Juan
La Rioja
Mendoza
Cordoba
29°S
30°S
31°S
32°S
33°S
72°W
71°W
70°W
69°W
68°W
67°W
66°W
65°W
64°W
N
0 50 100 km
Sedimentary
Qa Quaternary fluvial-alluvial
Qe Quaternary eolian
PN Paleogene-Neogene
Ks Cretaceous
Js Jurassic
Ts Triassic
CPs Carboniferous-Permian
OD Ordovician-Devonian
€O Cambrian-Ordovician
Igneous
Mi Miocene-Pleistocene
EOi Eocene-Oligocene
KPi Cretaceous-Paleocene
Ki lower-mid Cretaceous
Ji Jurassic
PTri Perm-Triassic Choiyoi Ign
CPi Carboniferous-Permian
Di Devonian-Carboniferous
Oi Ordovician Famatinian Arc
€i Cambrian Pampean Arc
Metamorphic
p€O Precambrian to Ordovician crystalline to metasedimentary
fault
city
Samples
Modern Sands Argentina
Capaldi et al., 2017
Modern Sands Chile
Pepper et al., 2016
Phanerozoic Basin Fill

Figure 1.2: Geologic map of Argentina and Chile (-28.5 to -33˚S) displaying sample locations, and major Phanerozoic magmatic provinces. JFR = Juan Fernandez Ridge

METHODOLOGIES

In order to define the ages and isotopic signatures of Andean arc magmatism, we present a compilation of new detrital zircon U-Pb ages and Hf isotopes results from modern river sands and ancient sandstones throughout the retroarc region of central Argentina (Figs. 2 and Fig. 3; Tables DR1and DR2 in the GSA Data Repository1). Zircon U-Pb data were acquired using laser-ablation inductively-coupled-plasma mass-spectrometry (LA-ICP-MS) at the University of Texas at Austin, following methods outlined in previous studies (Levina et al., 2014; Horton et al., 2016; Hart et al., 2016; Mackaman-Lofland et al., 2019). Zircon Hf isotopic analyses were conducted by laser ablation multicollector inductively-coupled-plasma mass-spectrometry (LA-MC-ICP-MS) at the University of Hong Kong, following methods outlined in previous studies (Xia et al., 2011).

Combined new U-Pb–εHf data are plotted as two-dimensional (2D) bivariate kernel density estimates (KDEs) using 10 Myr and 2 ε unit set kernel bandwidths for ages <550 Ma εHf values, for *Hafnium Plotter* software details and methodologies see Sundell et al., 2019. The bivariate KDE is contoured based on 95% from peak density contour interval and viewed as a color-coded intensity plot (Fig. 3).

These data are integrated with previously published U-Pb ages and Hf isotope results from modern river and beach sands of the central and Southern Andes (Fig. 4; Pepper et al., 2016; Capaldi et al., 2017). Our compilation of new and published detrital zircon U-Pb and Hf results is compared to existing bedrock zircon U-Pb–εHf data from several sources (e.g. Dahlquist et al., 2013; Herve, 2014; Jones et al., 2015) and to the regional spatial context for 1348 bedrock radiometric ages across central Argentina and

Chile (Fig. 4; Pilger, 2019; DR3 in the GSA Data Repository1). General agreement between the detrital zircon and bedrock compilation for central Argentina and Chile indicate that U-Th-Pb and Lu-Hf datasets derived from detrital samples provide a powerful tool for rapidly interrogating long-lived records of magmatism and effectively fill potential data gaps in the available bedrock record (Pepper et al., 2016; McKenzie et al., 2016). This approach is especially well suited to the transition region from the central to southern Andes, where nearly continuous Mesozoic and Cenozoic records of basin evolution in retro-arc regions provide a long-lived record of Andean arc magmatism (Uliana and Biddle, 1988; Mpodozis and Ramos, 1990; Horton et al., 2016; Horton, 2018b).

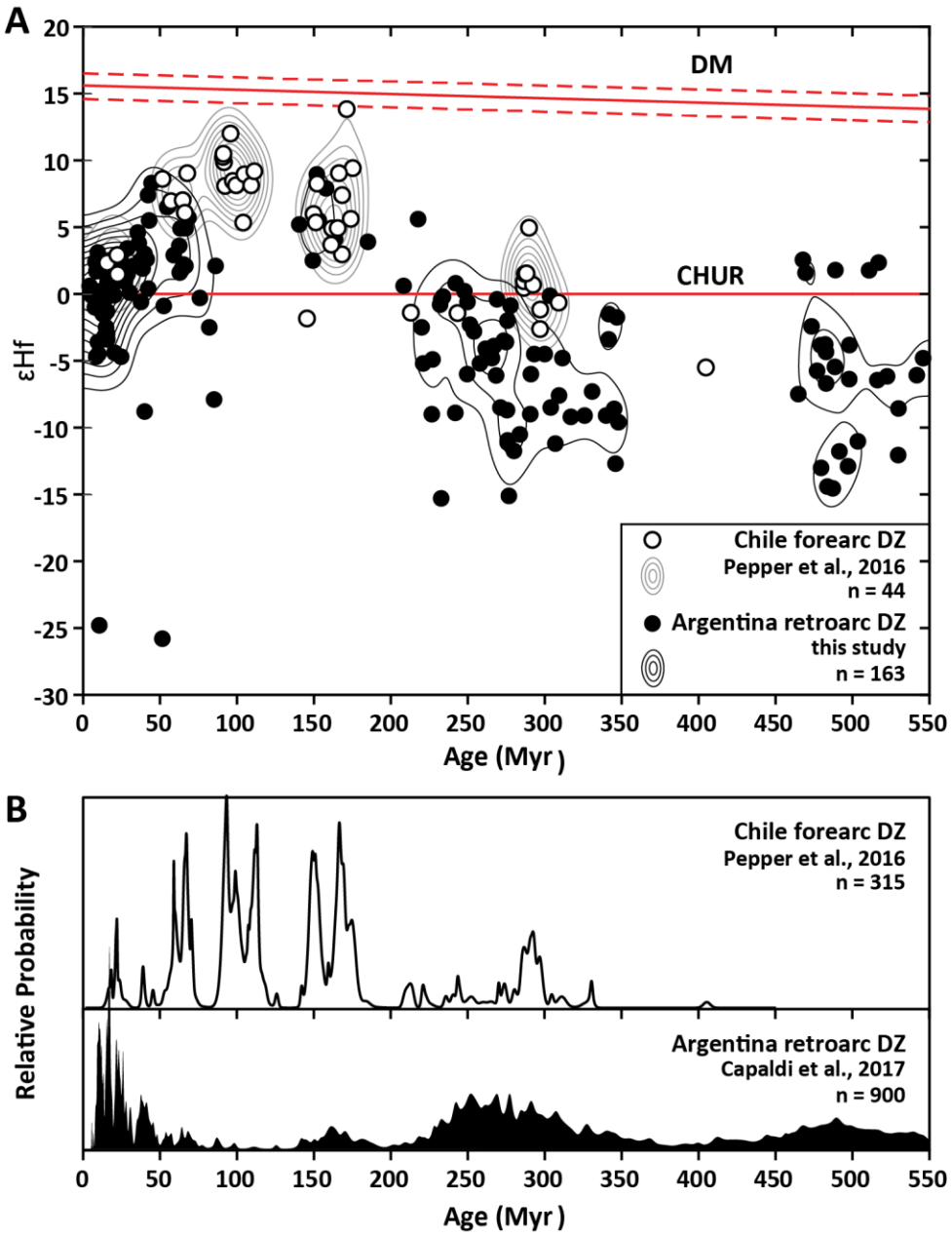

Figure 1.3: Two-dimensional (2D) view of combined U-Pb–εHf(t) results plotted as bivariate kernel density estimates for zircons <550Ma (10Myr and 2ε unit set kernel bandwidths). DM=depleted mantle, CHUR = Chondritic uniform reservoir. Intensity contour plot represent 95% of the maximum intensity.

PHANEROZOIC MAGMATISM AND ASSOCIATED TECTONIC HISTORY

Coupled zircon U-Th-Pb and Hf isotopic results integrated with bedrock geochronology to provide valuable insights into the temporal and spatial distribution of continental arc magmatism and associated isotopic patterns during major shifts in Cordilleran plate dynamics along the western margin of South America (Fig. 4). In order to facilitate a direct comparison between the different datasets and arrive at a unified interpretation, we present an integrated synthesis of U-Pb age distributions for 1773 detrital zircon grains of Phanerozoic age (550-0 Ma), and corresponding Th/U ratios (Fig. 4A), a synthesis of 634 zircon Hf isotopic results from detrital and bedrock samples (Fig. 4B), a summary of 1348 igneous bedrock radiometric ages showing the time-space variations in Phanerozoic arc magmatism (Fig. 4C) to reconstruct key steps in the geodynamic evolution of the plate margin (Fig. 5). We seek to correlate radiogenic isotopic signatures and the tectonic evolution along the southern Central South American margin during (1) Cambrian-Ordovician Collision, (2) Carboniferous Ocean-Continent Convergence, (3) Permian-Triassic Subduction and back-arc extension, and (4) Jurassic to Present continental arc, to help address processes that drive Cordilleran type-subduction and upper-plate tectonics.

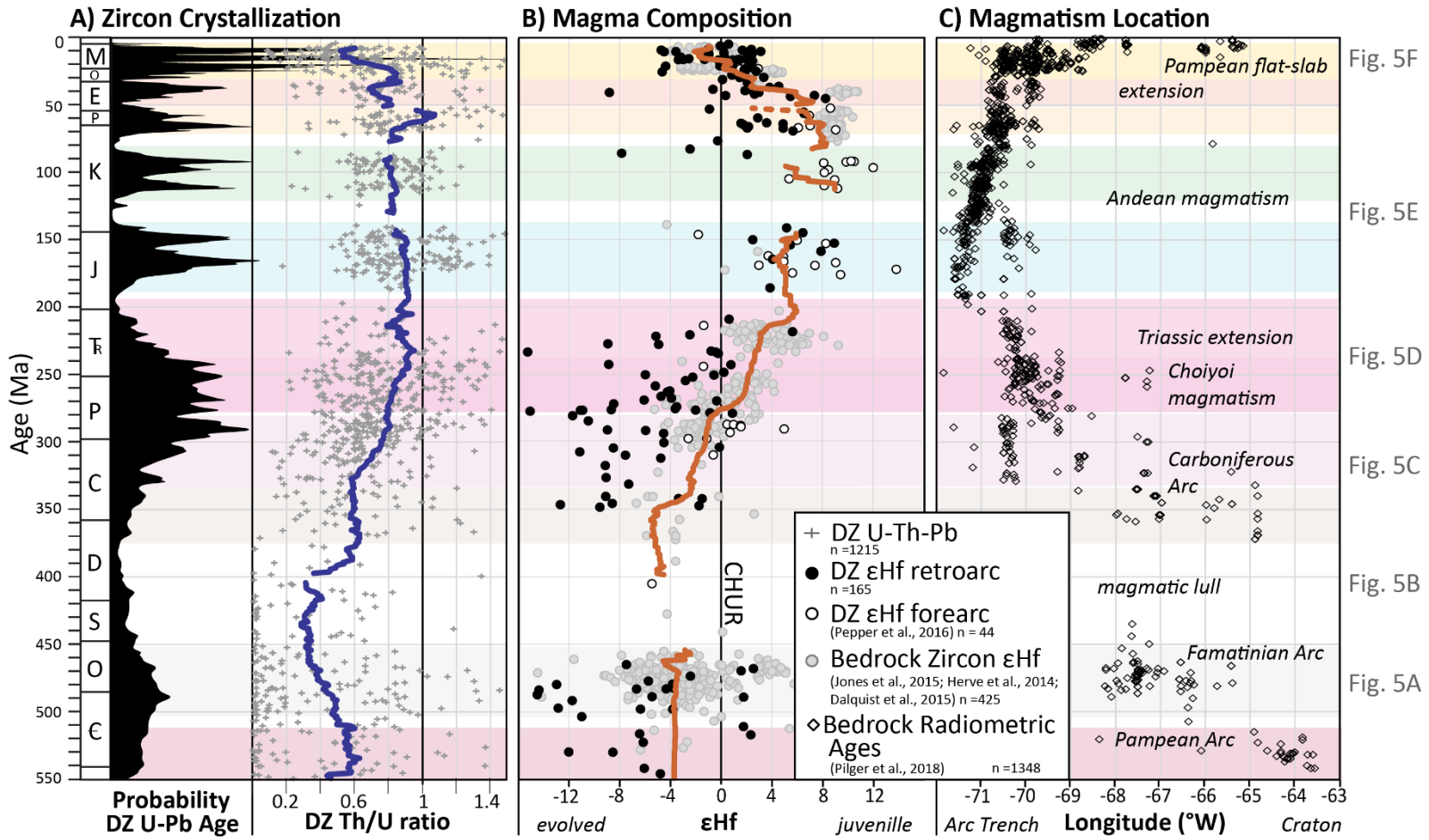
A) Zircon Crystallization
B) Magma Composition
C) Magmatism Location
Age (Ma)
Probability
DZ U-Pb Age
DZ Th/U ratio
εHf
evolved
juvenille
CHUR
Arc Trench
Longitude (°W)
Craton
DZ U-Th-Pb
n =1215
DZ εHf retroarc
n =165
DZ εHf forearc
(Pepper et al., 2016) n = 44
Bedrock Zircon εHf
(Jones et al., 2015; Herve et al., 2014; Dalquist et al., 2015) n =425
Bedrock Radiometric Ages
(Pilger et al., 2018)
n =1348
Pampean flat-slab extension
Andean magmatism
Triassic extension
Choiyoi magmatism
Carboniferous Arc
magmatic lull
Famatinian Arc
Pampean Arc
Fig. 5F
Fig. 5E
Fig. 5D
Fig. 5C
Fig. 5B
Fig. 5A

Figure 1.4: Phanerozoic magmatism dataset comparison plots for the western South American margin (-28.5 to -33 ˚S) see Figure 1 for sample locations. (A) Detrital zircon U-Pb age distributions of Phanerozoic age (550-0 Ma) and corresponding zircon Th/U ratios. (B) Synthesis of detrital and bedrock zircon Hf isotopic results in ƐHf notation. Grey trend lines are 2 Myr moving average windows. (C) Summary of bedrock radiometric ages showing the time-space variations by sample longitude (˚W) location (Pilger, 2018). Colored horizontal bars highlight the duration of regional tectonic events and corresponding lithosphere-scale cross-sections in Figure 5)

Cambrian-Ordovician Collision

Cambrian-Ordovician (550-440 Ma) detrital zircon U-Pb ages yield relatively negative εHf values (mean of -5.7), with broad U-Pb age peaks at 550-520 and 490-465 Ma, with corresponding mean εHf values of -7.5 and -5.9, respectfully. Zircon grains of this age display a considerable range in Th/U ratios and a greater proportion of low Th/U ratios (< 0.5) than subsequent younger magmatic phases. The average Th/U ratios and εHf isotopic values are among the lowest for all Phanerozoic results considered in this study (Fig. 4B).

Zircon isotopic signatures derived from the Cambrian-Ordovician igneous and metamorphic belts exhibit evolved magmatic patterns (mean εHf values of -5.7) and metamorphic zircon growth (< 0.5 Th/U ratios) that correspond to the collision of continental blocks of Laurentian affinity with the Gondwanan margin of South America (Fig. 5A; Schwartz et al., 2008; Ducea et al., 2010; Rapela et al., 2016). Dramatic, step-wise trenchward shifts in early Paleozoic magmatism (>300 km westward shift in ~30 Myr), suggest that subduction driven magmatism rapidly jumped westward to the new continental margin following continental terrane accretion events. In addition, the relative negative εHf isotopic signatures are indicative of evolved magma generation through thick continental crust, a pattern consistent with considerable shortening and crustal thickening during the 525-515 Ma Pampean and 460-440 Ma Famatinian orogenesis (Coira et al., 1982; Astini et al., 1996; Ramos, 2004; Schwartz et al., 2008; Charrier et al., 2015). Relative lull in arc magmatism at 515 Ma spanned ~10 Myr, followed by arc cessation that

occurred at 440 Ma immediately following the accretion of the continental terranes (Fig. 5A).

Silurian-Devonian (450-370 Ma) Peri-Gondwana arc magmatism is less well characterized by limited zircon isotope data, which may be associated with a magmatic lull during continued accretion of Cuyania, MARA, and Chilenea terranes prior to renewal of Paleozoic convergence between South America and oceanic lithosphere (Figs. 5B and 5C). Other models to explain Silurian-Devonian magmatic quiescence include the possible accretion of exotic terranes, prolonged episode of flat slab subduction, or development of a passive margin (Ramos, 1988; Giambiagi et al., 2014; Rapalini et al., 2018; Cawood, 2005; Ramos, 2009; Dahlquist et al., 2018). The mid-Paleozoic (Silurian-Devonian) lull in igneous activity was followed by late Paleozoic arc magmatism linked to the (re)establishment of a long-lived convergent margin along the western margin of South America (Fig. 5C).

Carboniferous Ocean-Continent Convergence

Magmatic activity since the Carboniferous has been well documented for the South American margin, but the mechanism(s) driving magmatism during Carboniferous-Triassic extension are debated. The Permian-Triassic Choiyoi magmatism in Chile and Argentina exhibits a transition from calc-alkaline affinities and intermediate to rhyolitic, to subsequent bimodal basalt-rhyolite magmatism. Previous models interpreted magmatic compositional changes to signal a change from subduction-related magmatism to

subduction shutoff and an intraplate anorogenic or extensional tectonic setting, invoking crustal melting for initial Choiyoi magmatism and decompression melting of asthenospheric mantle for the post-Choiyoi magmatism (Kay et al., 1989; Mpodozis and Kay, 1992; Llambías and Sato, 1995; Martin et al., 1999; Kleiman and Japas, 2009). This interruption to subduction during the Carboniferous to Jurassic Pre-Andean cycle has been recently questioned by studies of the origin and geochemistry of Late Paleozoic-Early Mesozoic magmatic rocks exposed along the Cordilleras of Northern Chile and Argentina, that suggest subduction to be continuous since the Late Paleozoic (Maksaev et al., 2014; Herve et al., 2014; del Rey, et al., 2016; Oliveros et al., 2018). Since isotopic signatures alone can produce non-unique interpretations of tectonic setting, additional temporal-spatial constraints are necessary to resolve whether subduction was a continuous since initiation in the late Paleozoic. Our results confirm the notion that Cordilleran subduction was temporally continuous, yet variable tectonic processes likely influenced the nature and composition of magmatism and isotopic variations since the late Paleozoic. As discussed below, these are represented by four distinct phases of late Paleozoic, Pre-Andean subduction: (1) Early Carboniferous initial slab-rollback and back-arc extension, (2) Carboniferous continental arc formation and punctuated Gondwanide contraction related to low-angle subduction, (3) Permian-Triassic silicic volcanism during slab-roll back and intra-arc extension, and (4) latest Triassic reestablishment of the continental arc.

Carboniferous to middle Permian (360-265 Ma) zircon grains are characterized by relatively negative εHf values (mean of -2.5), similar to early Paleozoic signatures, and dominant U-Pb age modes at 360-330 Ma and 330-305 Ma, with mean εHf values -5.2 and

-6.1, respectively (Fig. 4B). Early Carboniferous magmatism is widely distributed (>500 km; Fig. 5C) over the margin and expressed as isolated, inboard granitic plutons emplaced during extensional conditions, consistent with isotopically evolved magmatism (mean εHf value of -5.2) linked to reworking of a thick continental crust within and inboard of the foreland (Dahlquist et al., 2013). Subduction initiation is here interpreted to begin by the latest Devonian to Carboniferous (360-335 Ma) and is recorded by a migration of distal magmatism westward (trenchward). Isotopic signatures during this interval are characteristic of magmas derived from enriched lithospheric mantle and recycled continental crust sources that homogenized in the lower crust and/or were contaminated in the upper crust during shallow pluton emplacement (Dahlquist et al., 2013). These modes of magmatism have been interpreted as related to incipient subduction driving upper-plate extension during slab rollback (Alasino et al., 2012; Dahlquist et al., 2013; del Rey, 2016).

The relatively outboard location of the Carboniferous arc, and the increasing time-averaged isotopic trends in both zircon εHf units (from-6 to > -4) and Th/U ratios (>0.6) (Fig. 4B) suggest that magmas were emplaced into thinner juvenile crust, outboard of the thicker craton. Carboniferous-Early Permian continental arc magmatism is shown to be relatively fixed along the convergent margin by ~335 Ma (Figs. 4C and 5C). Early Carboniferous subduction is supported by petrographic and metamorphic age relationships within Paleozoic fore-arc deposits that record convergence initiating at a minimum between 343 and 310 Ma (Willner et al., 2012). Carboniferous magmatism is interrupted by the punctuating San Rafael compressional event (284-270 Ma), which is marked by intense folding and thrusting along a NW-NNW trending orogen in the Argentinian Frontal

Cordillera and San Rafeal uplift further south (Llambias and Sato, 1990; Kleinman and Japas, 2009; Ramos and Folguera, 2009; del Rey, 2016). The San Rafael tectonic phase has been interpreted to be associated with the shallowing of subduction during the latest Carboniferous-Early Permian final phases of the Gondwanide orogeny and assembly of Pangea (Kleinman and Japas, 2009; Ramos and Folguera, 2009). This episode of shallowing subduction angle is supported by the abrupt cratonward (eastward) broadening of volcanism and arc front migration (>250 km) (Fig. 4C; Ramos et al., 1989; Giambiagi et al., 2014; Hervé et al., 2014). Though not evident at these latitudes the broadening of magmatism eastwards during San Rafeal orogenic event ca. 300 to 290 Ma was driven by non-uniform slab shallowing between 31°S and 39°S with interpreted progressive slab shallowing south of 31°S to 36°S and complete flat slab between 36°S and 39°S (Kleiman and Japas, 2009).

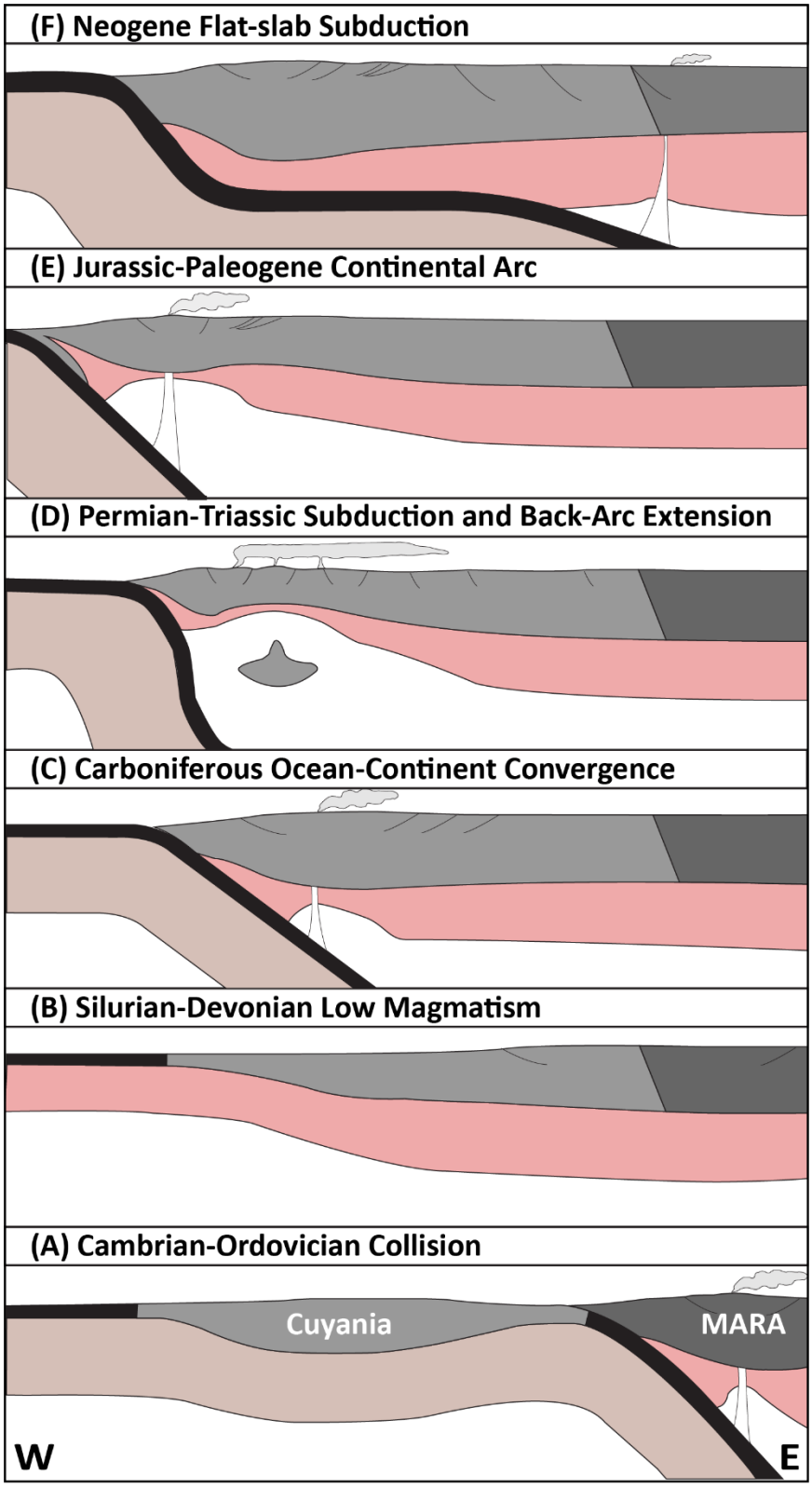
(F) Neogene Flat-slab Subduction
(E) Jurassic-Paleogene Continental Arc
(D) Permian-Triassic Subduction and Back-Arc Extension
(C) Carboniferous Ocean-Continent Convergence
(B) Silurian-Devonian Low Magmatism
(A) Cambrian-Ordovician Collision
Cuyania
MARA
W
E

Figure 1.5: Tectonic models for key Phanerozoic events along western South American margin. (A) Cambrian-Ordovician collision. (B) Silurian-Devonian igneous lull. (C) Carboniferous ocean-continent convergence. (D) Permian-Triassic subduction and back-arc extension. (E) Jurassic-Paleocene continental arc. (F) Eocene-Present Andean orogenesis.

Permian-Triassic Subduction and Back-arc Extension

Permian-Triassic magmatism is exemplified by the extensive Choiyoi igneous complex, a combined intrusive and extrusive suite associated with an ignimbrite flareup (Fig. 1; Kleinman and Japas, 2009). Results from Permian-Triassic zircons (275-215 Ma) reveal a pronounced shift from negative to positive εHf values (mean εHf values of 1.9), and systematic increase in Th/U ratios from ~265 to 240 Ma (Fig. 4B). These geochemical trends are accompanied by some of the most voluminous pulses of magmatism as identified by the dominant age peaks of 305-285, 285-265, 265-245 and 245-215 Ma with corresponding εHf values -1.9, -1.9, 0.6 and 2.4, respectfully.

The Choiyoi igneous complex progressed from granitic/dacitic magmas during convergent arc magmatism (290–265 Ma) towards intermediate or bimodal compositions during extensional magmatism (265–250Ma) as the upper-plate transitioned to a post-orogenic collapse magmatic setting (Fig. 2; Kay et al., 1989; Mpodozis and Kay, 1992; Kleiman and Japas, 2009). The Th/U values of Permian-Triassic (265–230 Ma) zircon grains increase to > 1 and positive εHf values in response to an increase in juvenile components related to asthenosphere upwelling triggered by extensional thinning. Mechanisms that generate spatially broad volcanism that migrates towards the trench include subduction slab-rollback and/or slab breakoff and lithosphere delamination beneath Gondwana, with resulting crustal thinning and upper-plate extension driving ignimbrite flare-up phases (Fig. 3D; Kay et al., 1989; Pankhurst et al., 2006). In this manner, a combination of post-orogenic collapse and back-arc extension during slab roll-back is considered to govern regional tectonics and mark the onset of a principally

extensional tectonic regime that characterized much of western South America during the Mesozoic. A similar scale and magnitude of broad silicic volcanism related to upper-plate extension and lithosphere delamination following a shallow subduction compressional event has been recorded by the Sierra Madre Occidental Cenozoic Silicic Large Igneous Province in Mexico (Murray et al., 2013; Ferrari et al., 2018).

Late Triassic zircons yield Th/U ratios with values predominately < 1 to 0.6, which are lower than the Permian-Triassic suite and indicative of typical continental arc values. The return to lower Th/U ratios similar to those in the Carboniferous implies re-establishment of classic Andean-style subduction along the South American convergent margin by the late Triassic (Fig. 5E). The observed trends in positive εHf values is associated with continental rifting involving the Cuyo and Ischigualasto systems. Petrography, geochemistry and isotopic composition of Triassic volcanic rocks show progressive changes over time, yet indicate a dominant subduction-related features that suggest continuous subduction along the western margin of South America from Late Paleozoic to Present (Vasquez et al., 2011; Barredo et al., 2012; Poma et al., 2014; del Rey et al., 2016; Coloma et al., 2017; Oliveros et al., 2017; Gonzales et al., 2018).

Jurassic to Present Continental Arc

Jurassic-Eocene zircon ages (210-50 Ma) display three magmatic phases that span 25-45 Myr and appear to be separated by 10-15 Myr magmatic lulls (Fig. 4A). The major zircon age modes include: Jurassic age cluster at 185-160 Ma and 160-138 Ma with mean

εHf values 6.0, and 4.4, respectively; a Cretaceous age cluster at 125-105 Ma and 100-80 Ma with mean εHf values 7.9 and 5.9, respectively; and a Paleocene age cluster at 75-50 Ma with mean εHf value of 8.1 (Fig. 4B). Notably, Jurassic-Eocene zircon εHf is consistently positive (mean εHf value of 7.2) and corresponding mean Th/U value range from 0.8 to 1 throughout this 150 Myr long phase of continental arc magmatism (Fig. 4A). Jurassic-Eocene continental arc magmatism is characterized by ~100 km of cratonward advance of the locus of arc magmatism during 140 Myr (Fig. 4C).

An Early Jurassic (200-185 Ma) lull in magmatism, as evidenced by a relative paucity of zircon generation and trenchward migration of diffuse magmatism are suggestive of slab roll back and trench retreat until subduction spatially stabilized along the western flank of South America by 185 Ma (Fig. 4C and 5E). Jurassic-Paleogene Andean arc magmatism was highlighted by ~20-30 Myr phases of juvenile (highly positive, mean εHf 6.0) indicative of slab-dehydration magmatism derived from the upper mantle. Zircons associated with Cretaceous arc magmatism display the most positive Hf values of the Phanerozoic suggesting thin crust during a neutral to decoupled slab system (Fig. 5E; Mackaman-Lofland et al., 2019). The latest Cretaceous to Eocene detrital zircons displays an initial decrease in εHf and slight eastward migration of the arc during the opening of the south Atlantic and increased plate velocities (Charrier et al., 2015).

The Eocene-Present (47-6 Ma) zircon age population defines a significant magmatic phase with age peaks at 47-26 Ma, 24-13 Ma, and 12-6 Ma (Fig. 4A). Zircon isotopic ratios shows a shift from Paleocene magmatism with mean εHf values of 8.1, to Eocene-Oligocene (45-26 Ma) phase with mean εHf values of 4.0, to low Miocene (24-6

Ma) negative mean εHf values of -0.1. The corresponding Th/U values display very high variability throughout the Cenozoic spanning from 0.2 to 2, with Late Miocene-Pliocene (12-6 Ma) mean Th/U ratio of 0.5 and an overall absence of Th/U values >1.

Eocene-Oligocene (45-24) magmatism exhibits an isotopic pull down of 6.0 εHf units, synchronous with Andean shortening within the Frontal Cordillera as documented by thermochronometric cooling ages (Lossada et al., 2017). Miocene zircon εHf values decrease synchronous with a broadening of the magmatic arc that corresponds to initiation of shallow-angle subduction, increased plate coupling and shortening (Figs. 4C, 5F). The rapid thickening of the Andean crust and relative advancement of the arc in the late Miocene produces more evolved arc magma generation as the flat slab propagated eastward post 12 Ma (Fig. 5F; Mpdozis and Kay, 2002; Almendinger and Judge, 2014; Jones et al., 2016).

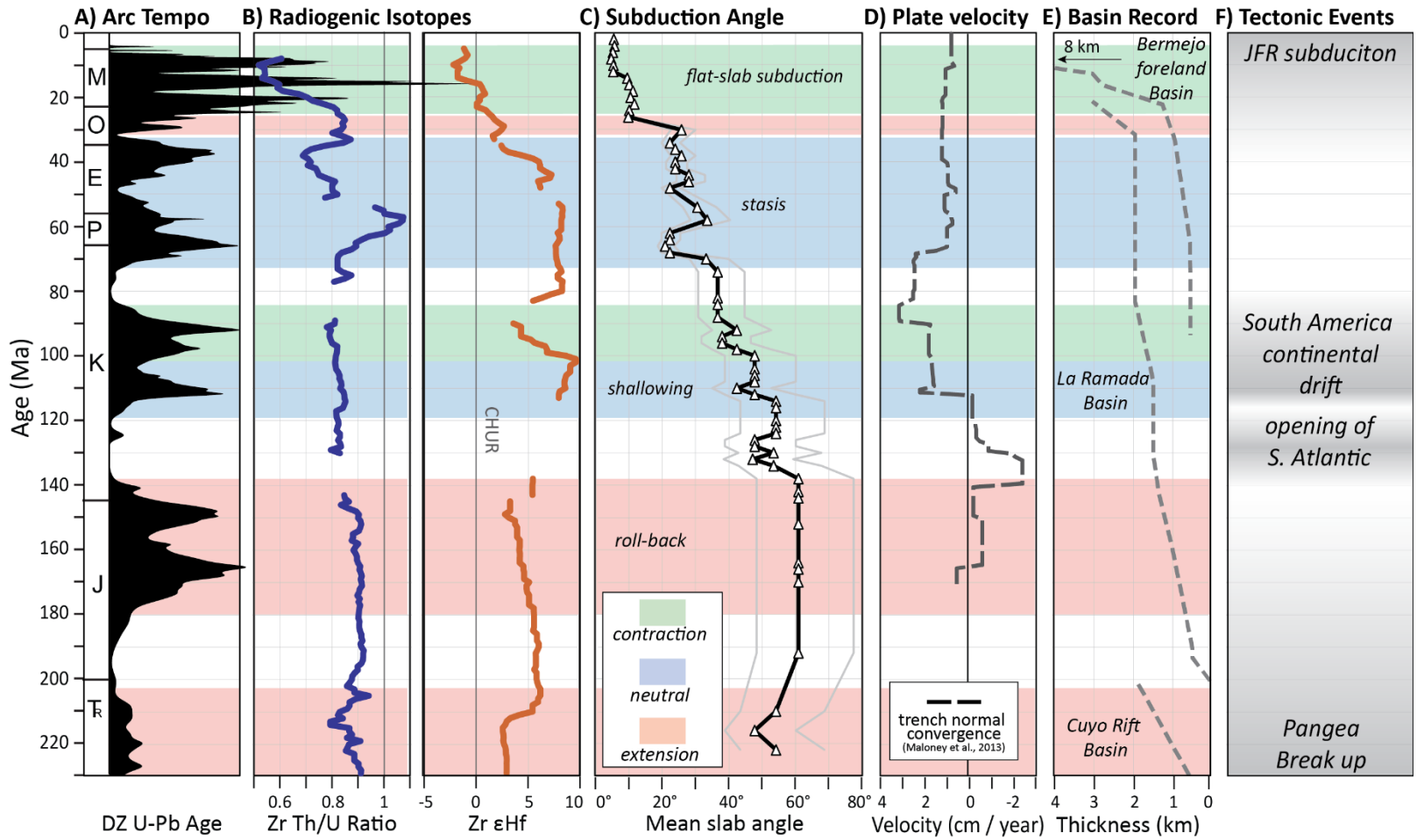
A) Arc Tempo
B) Radiogenic Isotopes
C) Subduction Angle
D) Plate velocity
E) Basin Record
F) Tectonic Events
Age (Ma)
M
O
E
P
K
J
Tr
flat-slab subduction
stasis
shallowing
roll-back
contraction
neutral
extension
CHUR
8 km
Bermejo foreland Basin
La Ramada Basin
Cuyo Rift Basin
trench normal convergence (Maloney et al., 2013)
JFR subduciton
South America continental drift
opening of S. Atlantic
Pangea Break up
DZ U-Pb Age
Zr Th/U Ratio
Zr εHf
Mean slab angle
Velocity (cm / year)
Thickness (km)

Figure 1.6: Triassic to present magmatism, continental arc width, subduction angle, and plate velocity models dataset comparison plots for the western South American margin (-28.5 to -33 ˚S; Fig. 2). (A) Detrital zircon U-Pb geochronology age distributions displaying high flux events and lulls, see Figure 1 for sample locations. (B) Detrital zircon U/Th ratios and ƐHf values. (C) Calculated Subduction angle change for the Jurassic to modern Andes. (D) Plate velocity model result for 32 ˚S, notice convergent velocities initiated in the Cretaceous (Maloney et al., 2013). (E) Retroarc basin subsidence plots highlighting phases of extensional to flexural sediment accommodation. (F) Key geodynamic events impacting the South American plate.

DISCUSSION

Cordillera-style orogenic systems involve the subduction of oceanic plates along significant lengths (4,000-7,000 km) of convergent margins and exhibit a range of upper-plate responses; from slab roll-back and associated upper-plate extension; to shallow-angle subduction driving orogenesis (e.g. Dickinson, 2004, Ramos, 2009, Schellart et al, 2007; Horton, 2018). Reconstructed subduction angle estimates from the Late Triassic to Present magmatic record can address potential linkages between (1) temporal frequency of magmatic high flux events and lulls, (2) spatial and temporal trends in zircon isotopic signatures, (3) changes in subduction angle, (4), plate velocity models, and (5) upper-plate deformation. The integration of U-Th-Pb and Lu-Hf isotopic datasets, Phanerozoic zircon U-Pb age distributions, and a spatially constrained magmatic record (Fig. 6), provides new insights into the feedbacks and relationships between upper-plate magmatism, deformation and linkage to possible lower-plate geodynamic drivers.

Andean Arc Tempo

Continental arcs experience episodic magmatism involving high flux events (HFE) within a ~30 Myr window followed by lulls in which volumetrically little magma is added to the arc (Patterson and Duecea, 2015; Kirsch et al., 2016). Recent models have shown that similar temporal patterns exist in other processes such as mantle convection, melting, deformation, magma ascent, erosion, sedimentation, and mountain building, which together are called arc tempos (Ducea, 2001; DeCelles et al., 2009; 2015; Karlstrom et al., 2014). Episodic HFE magmatism may result from external forcing of arc systems (e.g.

plate reconfigurations, mantle dynamics, collisions), and/or result from internal cyclic processes driven by feedback between linked tectonic and magmatic processes. Evaluating the operative spatial and temporal scales of arc magmatism provides a means to test proposed high-flux events and magmatic lulls that may generate cyclical or punctuated arc tempos at regular or irregular recurrence intervals. The magmatic record of Argentina and Chile (28-33˚S) displays a characteristic 20-30 Myr temporal recurrence of high flux events and lulls in zircon age distribution during continental arc magmatism (230-0 Ma), which appears to be superimposed on a longer >200 Myr spatial trend in arc location (Figs. 6A and 7). During the 230 Myr span of Triassic to Present arc magmatism, 8 HFEs are recorded by zircon U-Pb age peaks: Triassic (230-200 Ma), Jurassic (185-160 Ma), Late Jurassic-Early Cretaceous (160-138 Ma), late Early Cretaceous (128-105 Ma), Late Cretaceous (102-80 Ma), latest Cretaceous to Early Eocene (75-50 Ma), Eocene to Oligocene (47-26 Ma), and Oligocene- Miocene (24-12 Ma) (Fig. 7). The HFEs typically span 20-30 Myr with the exception of the Neogene HFEs that are < 15 Myr, and are interrupted by magmatic lulls that decrease in duration through time from Jurassic (15 Myr) to Miocene (< 2 Myr) (Fig. 7). Change in subduction angle, (both increase and decrease) is a common process occurring between each HFE, with the exceptions being the two Jurassic HFEs. Even small variations in slab angle < 10° may drive tectonic reorganization and structural configurations that can induce changes to bulk compositions of the lower crust–mantle lithosphere regions beneath arcs that lead to rejuvenation of melting and HFE. Particularly, during phases of lower subduction angle (< 40°) each interpreted shortening event (i.e. Late Cretaceous, Paleocene, and Eocene) is followed by a subsequent phase of

extensional or neutral stress conditions during the same magmatic HFE (Fig. 6). The spatial-temporal association among deformation, magmatism, and subduction angle over cyclical frequencies of 20-30 Myr has the potential to be the external catalyst that drives internal tectonic feedbacks within the upper-plate Cordilleran cyclicity models (DeCelles et al., 2009; 2015).

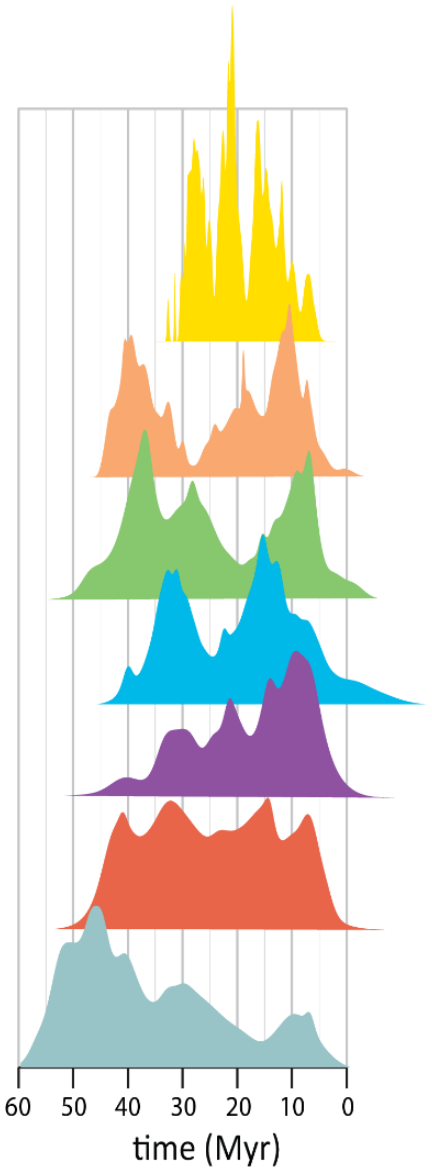

Figure 1.7: Detrital zircon age distributions from key phases of Phanerozoic magmatism recording differentiation in arc tempo. Colors represent Neogene (yellow), Paleogene (orange), Cretaceous (green), Jurassic (blue), Triassic (purple), Permian-Triassic (red), and Carboniferous (grey).

Radiogenic Isotopic Trends

Both radiogenic U-Pb-Th and Lu-Hf isotope systems in zircon shows a strong spatial correlation between cratonward advance of magmatism and a decreasing (more evolved) isotopic signature. The spatial drivers of magmatism migration in the zircon isotopic systems are sensitive to upper-plate tectonic processes (extension-shortening) that are linked proposed variation in subduction angle.

Changes in radiogenic isotopic signatures in zircon have been interpreted to distinguish magmatism derived from the mantle or recycled crustal sources and to link how upper-plate processes of contraction to extension facilitate magma generation. Studies have argued that relative increase in zircon εHf is indicative of an extensional arc system associated with an outboard migration of subduction zone magmatism during slab rollback and associated crustal extension and thinning (Kemp et al. 2009). Additionally, zircons with wide a range of Th/U values, including significant populations of elevated Th/U zircon (>1.0) and very few zircons with Th/U <0.5, are associated with extensional tectonism that tends to produce hotter magmas (700->1000˚C), increased fractionation, and more primitive mafic melts (Kirkland et al., 2015; McKay et al., 2018). Conversely, during times of convergence, collision, and terrane accretion contractional arc systems show a decrease in zircon εHf during an inboard migration of magmatism, increased crustal assimilation during crustal thickening and underthrusting of fertile crust to the melt source region, which is more conducive to producing low zircon Th/U ratios (<1.0) with little geochemical variability (Kemp et al., 2009; McKay et al., 2018). However, resultant temporal shifts in radiometric isotope compositions have also been shown to simply reflect

the composition of deep lithosphere, rather than crustal deformation processes (Chapman et al., 2017). In this case, trenchward (westward) magmatism correlates with increase in zircon εHf by reducing assimilation due to magma ascent through thinner, possibly juvenile crust and/or melting of upwelling depleted asthenospheric mantle. Conversely, a cratonward (eastward) shift of the arc magma source region would correlate with decrease in zircon εHf due to increased melting of ancient enriched lithospheric mantle (Chapman et al., 2017). Here we discuss the degree to which upper-and lower-plate tectonics influence observed temporal isotopic shifts and associated patterns of arc migration, temporal variability, and angle of subduction.

Phanerozoic magmatism in Argentina and Chile (28.5°-33° S) extends to >800 km from the subduction trench, including the Chilean forearc, Andean arc, Argentina foreland, and into the eastern craton region of the Sierras Pampeanas (Fig. 2). Zircon radiogenic isotopic compositions display a spatial trend, from west to east landward of the trench, of decreasing, evolved isotopic variation encompassing ~24 εHf units and 1.6 units of spread in Th/U ratios (Fig. 8). A strong correlation exist between low 0 to -12 εHf units and Th/U ratios across eastern longitudes (-68 to -63° W), supporting the idea that inboard magmatism is generated at the base of thickened lithosphere that is deriving crustal isotopic signatures and cooler crystallization temperatures. The Devonian to Carboniferous magmatism records evolved isotopic signatures as plutonism initiated eastward from the trench within relatively thickened of the crustal craton region, which subsequently migrates trenchward coeval with an increase in zircon εHf units and Th/U ratios (Fig. 2). However, deviations from the observed spatial trend are most notable proximal to the trench (-72 to

-68° W), where zircon radiogenic isotopes display a greater dispersion in εHf values (-4 to 10) and Th/U ratios (0.5 to 1.5) (Fig. 8). Variability in Th/U ratios are indicative of the prolonged Permian-Triassic magmatic phase with high (>1) Th/U ratios superimposed by Mesozoic Andean arc magmatism with typical (Th/U ratios 0.6 to 1) (Fig. 7). There is a somewhat better fit to the observed negative correlation with location from west to east by zircon εHf data suggesting that the Lu-Hf system is more sensitive to inherited lithospheric architecture established by preceding tectonic events. For example, lithosphere within the eastern regions (-68 to -63° W) are intrinsically more isotopically evolved since Early Paleozoic subduction and accretion generated thickened lithosphere. Subsequent magmatism in the eastern craton region occurred during key contraction events that also record evolved isotopic signatures, with the exception of Carboniferous subduction. Conversely, western, trenchward lithosphere was spatially overprinted during predominately arc retreat and extension related magmatism (e.g. Carboniferous, Permian-Triassic, Triassic-Jurassic phases) establishing an isotopic signature indicative of thinner crust and juvenile mantle derived magmatic sources. Our new Phanerozoic magmatism compilation from Argentina and Chile highlights how isotopically evolved signatures involve positive feedbacks among subduction angle decrease and associated crustal thickening and magmatism that intruded thicker continental lithosphere towards the craton. In contrast, juvenile isotopic magmatic signatures are a combination of high subduction angle that is associated with crustal extension, with magmatism located in thinner lithosphere proximal to the subduction trench. Spatial magmatic patterns of zircon εHf and

Th/U ratios provides new insights into the architecture of convergent margins mantle lithosphere and tectonic temporal patterns of Cordilleran orogens.

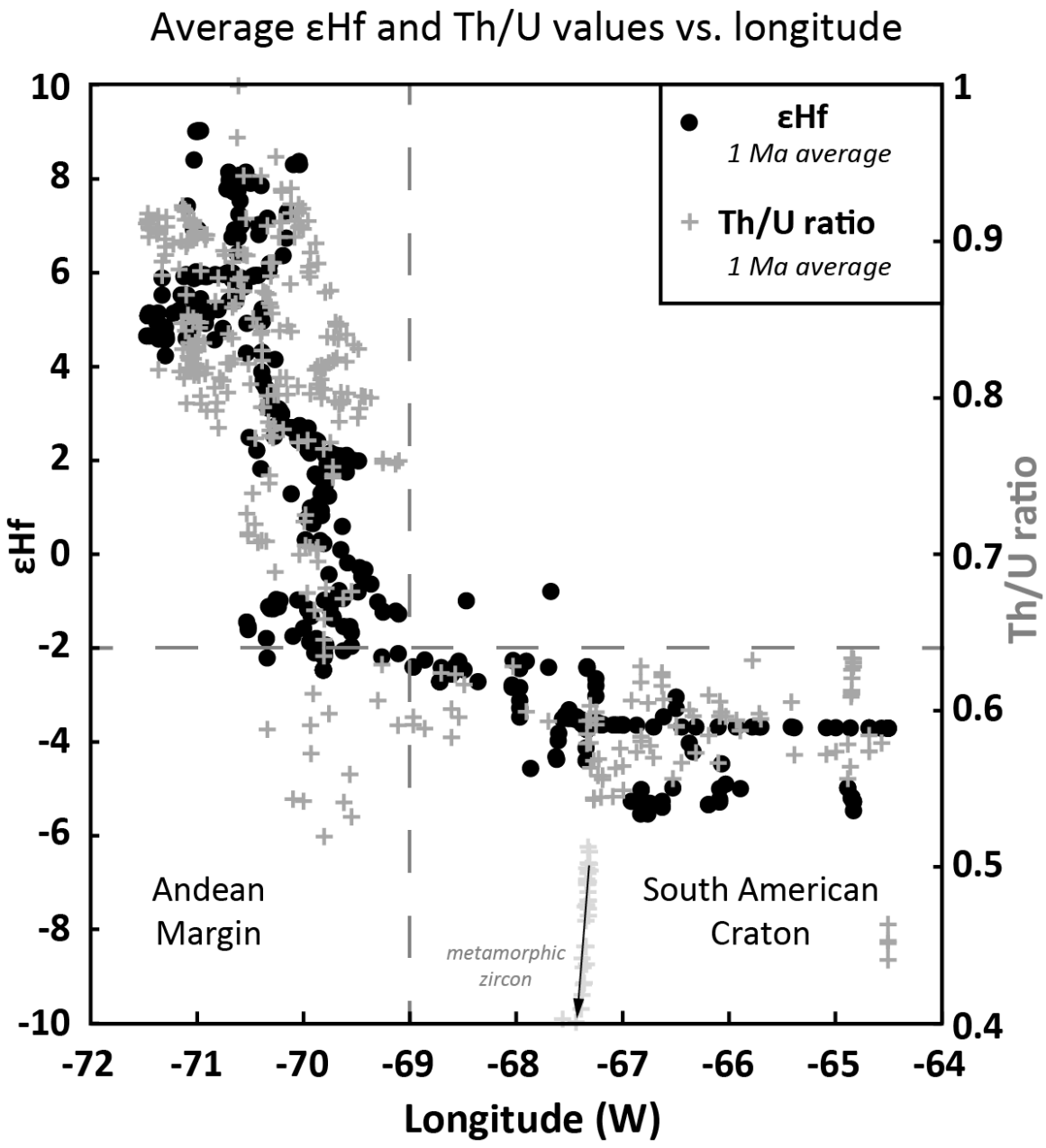

Figure 1.8: Phanerozoic radiogenic isotope spatial trends from Argentina and Chile (-28.5 to -33˚S). Plotted zircon εHf and Th/U values and corresponding location are generated from a 2 Myr average moving window for Phanerozoic (0-550 Ma) isotope values and location (Fig. 2). Spatial trends display composition of magmatism becomes more isotopically evolved (-εHf) and toward lower Th/U ratio (< 0.8) landward (eastward) of the trench.

Subduction Angle

Establishing long-term estimates of subduction angle change is critical to address the spatial-temporal relationships and feedbacks among lower-plate variation, Mesozoic and Cenozoic magmatism, and upper-plate stress (Coney and Reynolds, 1977). A highly simplified approach to determining the angle of the down-going plate can be calculated assuming subduction driven hydration melting occurs between 120-180 km depth (Kessel et al., 2005); calculating the width of arc magmatism from the bedrock radiometric age database (Pilger, 2018); and palinspastically restoring arc width by calculating Cenozoic Andean shortening estimates from the Argentina retro-arc region (Fig. 9). Cenozoic shortening includes 100 km in the Precordillera fold-thrust belt, 10 km from the Frontal Cordillera, 15 km within the Principal Cordillera, and 10 km along the Coastal Cordillera (Cristallini and Ramos, 2000; Farías et al., 2008; Allmendinger and Judge, 2014). Late Triassic to Jurassic slab angle appears to have increased from 50° to 60° as magmatism migrates trenchward (Fig. 6C). Lower Cretaceous slab angle decreased to 45°-55° and with no clear evidence for arc migration. Late Cretaceous slab angle decreases to ≤ 40° as the arc migrates steadily towards the craton until the Paleogene when subduction angle has decreased to 25°. Drastic broadening of the Neogene magmatic arc (> 700 km) was associated with the shallowing of subduction angle to 10° and to 5° by the Upper-Miocene. Changes in subduction angle appears to have operated over two different temporal timescales, a longer >200 Myr temporal decrease in angle through the Mesozoic-Cenozoic exhibiting a range in values from 60° to 5°, and shorter superimposed 10 Myr change in subduction angle with magnitudes of < 10° (Fig. 6C).

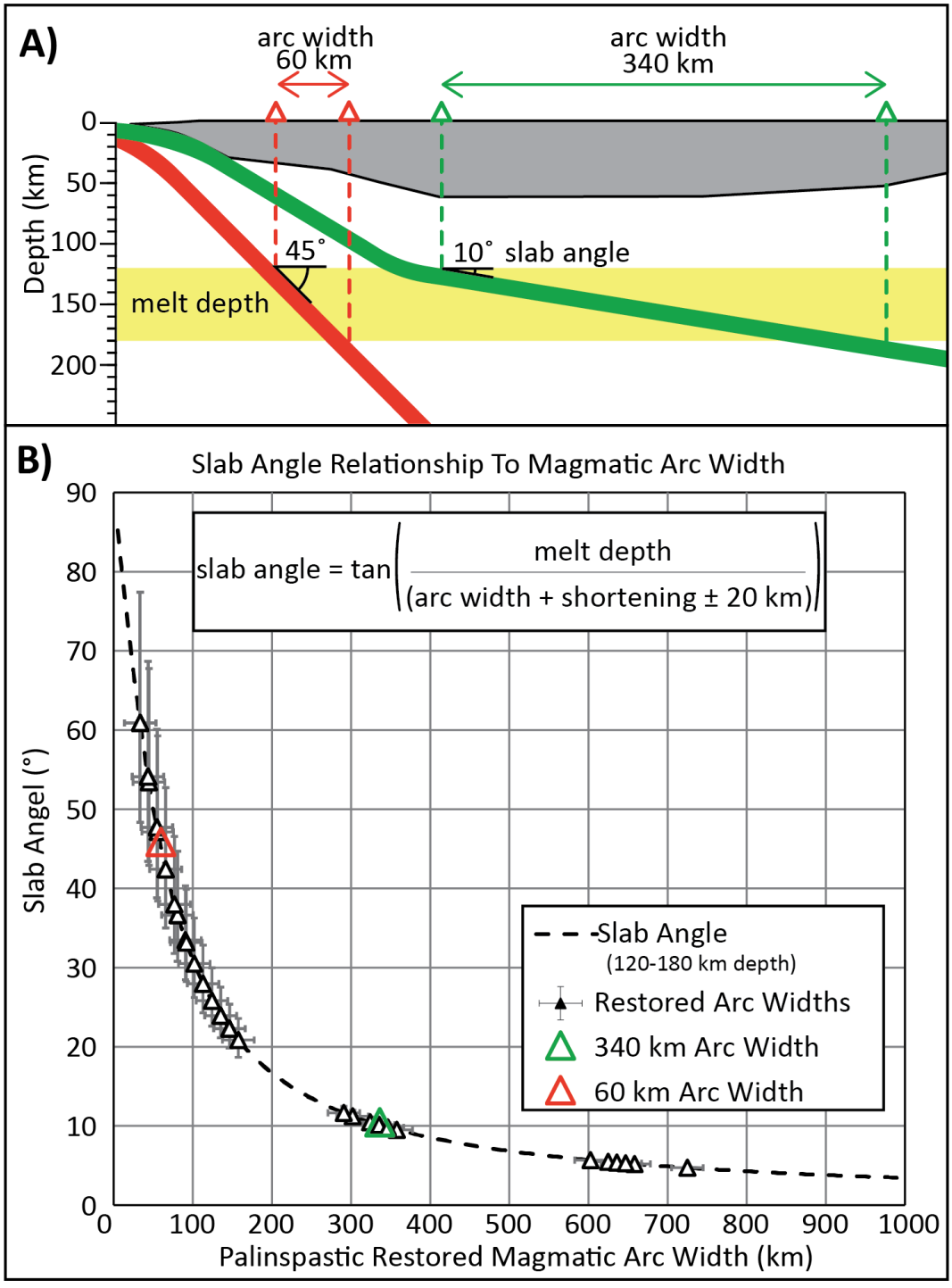
A)
arc width
60 km
arc width
340 km
Depth (km)
0
50
100
150
200
45˚
10˚ slab angle
melt depth
B)
Slab Angle Relationship To Magmatic Arc Width
slab angle = tan (melt depth / (arc width + shortening ± 20 km))
Slab Angel (°)
90
80
70
60
50
40
30
20
10
0
0
100
200
300
400
500
600
700
800
900
1000
Palinspastic Restored Magmatic Arc Width (km)
Slab Angle
(120-180 km depth)
Restored Arc Widths
340 km Arc Width
60 km Arc Width

Figure 1.9: Calculating subduction angle from continental arc width. (A) The palinspastic restored continental arc width is a function of the oceanic crust subduction angle passing through a dehydration melt window at 120-180 km depth in the asthenosphere. (B) Slab angle relative to arc width (grey dashed line) for 45° slab angle (red triangle) and 10° (green triangle), calculated Triassic to Quaternary slab angle from palinspatic restored arc widths from the western South American margin (black triangles) with ± 20 km error bars highlighting the increased uncertainty with steeper slab angle.

Plate Velocity

Geochronology and radiogenic isotope signatures are sensitive to changes within the over-riding plate in Cordilleran-type subduction, whereas spatial patterns of magmatism from radiometric igneous ages serves as a proxy for lower-plate subduction angle variability. Possible driving mechanisms that control subduction angle along the Andean margin include absolute plate velocities, oceanic crustal thickness (i.e. asperities), slab length, and mantle dynamics. Integrating magmatism location and calculated subduction angle with isotopic signatures recorded along Phanerozoic margin of South America points to variable mechanical coupling between the subducting and overriding plates (Horton 2018).

Recent geodynamic models predict that upper-plate stress regime is directly related to the subducting lower plate interacting with mantle 660km discontinuity where increased viscosity contrast induces a subduction impedance (Faccena et al., 2017; Schellart, 2017; Chen et al., 2019). The geodynamic models broadly predict an initial phase of upper-plate extension related to slab roll-back within the upper-mantle, followed by upper-plate contraction as the down going plate penetrates the 660 km discontinuity and anchors into the lower mantle. However, issues arise when comparing geodynamic model predictions on subduction duration and initiation of Andean orogenesis. Numerous geodynamic models imply Andean orogenesis occurs over much fast time periods (45 – 90 Myr) (Faccena et al., 2017; Chen et al., 2019), which occur over much shorter timeframes than what is observed by the geologic record (> 200 Myr) (Fig. 6). Our results highlight the synchronous nature of subduction angle change over similar timescales with deformation

of particularly short lived (<15 Myr) phases of shortening and shallower subduction angle (40 to 5°) during the Cretaceous and Paleogene (Figs. 6). Potential driving mechanism for the calculated decrease in subduction angle involves long lived subduction (>100 Myr) and slab anchoring into the lower mantle in the Jurassic. Cyclical behavior (20-30 Myr) in arc tempo involves reoccurring inboard sweep arc magmatism and shortening during slab shallowing, and neutral to extensional conditions during slab re-steepening (Haschke et al., 2002, 2006; Ramos, 2009; Ramos et al., 2014). Recent geodynamic modelling has suggested that slab folding and deformation at the 660 km mantle discontinuity is a potential mechanism for periodic short-term (~20–30 Myr) changes in slab dip angle which are superposed on the long-term trend of slab dip angle (Fig. 6; Schellart et al., 2017). The correlation between magmatic activity and isotopic changes over 20-30 Myr timescales is similar to what is predicted by variation in slab angle, which in turn drive changes among decoupled, neutral, and coupled subduction settings (Horton and Fuentes, 2016; Horton, 2018; Mackaman-Lofland et al., 2019).

Andean Geodynamic processes

The temporal variation among Mesozoic to Cenozoic Cordilleran subduction processes exhibit a pronounced 100 Myr trend in magmatism broadening and magmatic front advance associated with subduction angle decrease, superimposed on 20-30 Myr variation in magmatic high flux events and lulls associated with lower-plate-mantle interactions and/or upper-plate Cordilleran cyclicity.

Geodynamic responses within the overriding plate have been linked to feedbacks between crustal shortening and under-thrusting, and magmatism, leading to the removal of dense lithospheric instabilities and extensional collapse, which potentially operate on frequencies of 25-50 Myr over the duration of subduction (Haschke et al., 2006; DeCelles et al., 2009, 2015; Karlstrom et al., 2014; Ramos et al., 2014).

Variation in Mesozoic to Cenozoic subduction angle estimates correspond with changes in upper-plate deformation regimes. The relationship between slab angle and upper-plate strain shows that the Triassic to Jurassic (230-140 Ma) high subduction angle calculated by the method above and displayed in Figure 4, which is greater than 55°, is synchronous with back-arc extension and volcanism. Zircon isotopes during this period have highly positive εHf and variable Th/U ratios (0.6 to 1.6), indicating an extensional continental arc within thinner lithosphere. Magmatism that migrated towards the trench from the Triassic to the Jurassic indicates arc retreat during a phase of slab roll-back that drives extensional tectonic regime with known retro-arc rifting and thermal sag deposits (Charrier et al., 2015).

Moderate slab angle (55°-40°) is associated with neutral coupling between the upper- and lower-plates during much of the Cretaceous. Late Early Cretaceous magmatism (128-105 Ma) is constrained to the Chilean arc region and synchronous with zircon Th/U ratios between 0.6 and 1, which are indicative of continental arc activity. The relatively invariant radiogenic isotopes, moderate subduction angle, and spatially stable arc location suggest the Early Cretaceous Cordilleran system is neither contractional nor extensional,

rather the boundary conditions reflect a neutrally coupled system (Horton and Fuentes, 2016; Mackaman-Lofland, 2019).

Two known flat-slab phases along the South American margin (Late Paleozoic and Late Cenozoic) are shown to be fundamental process in convergent margin subduction, magmatism, and upper-plate deformation. Recognizing the impact of ancient flat-slab subduction along-strike and in other Cordilleran systems will lead to better characterization of the effect that external drivers such as oceanic asperities, have on long-lived subduction systems. Punctuated phases of crustal shortening occurred when slab angles were lower than 40° (Fig. 10D). The Cretaceous to Paleogene decrease in subduction angle to less than 40° was associated with punctuated volcanism broadening phases and decreases in subduction angle by ~10° during the Late Cretaceous (~105-90 Ma), Late Cretaceous to Paleocene (68-62 Ma), and Late Eocene (45-35 Ma) (Fig. 4). Shortening was synchronous with minor latest Cretaceous arc broadening during structural inversion of early Cretaceous depocenters along the Coastal Range, which are recorded by syntectonic deposits in the retroarc foreland (Cembrano et al., 2003; Pineda and Emparán, 2006; Rodríguez, 2013; Reat and Fosdick, 2018; Mackaman-Lofland et al., 2019). Minor phases of arc broadening (subduction angle to 20- 30°) and zircon isotopic decreases during the Late-Cretaceous to Paleocene (68-62 Ma) and Late Eocene (45-35 Ma) are potentially associated with shortening in the arc proximal regions (Fig. 4B and 4C). Angular unconformities within the Principal Cordillera fold-thrust belt and magmatic arc correspond to two minor shortening events within the Late-Cretaceous and Late Eocene (Rivano et al., 1993; Cristallini and Ramos, 2000; Segemar, 2000; Sernageomin, 2003; Jara and Charrier, 2014).

Paleocene to Eocene shortening has been recorded by cooling ages in the High Andes and associated deposits in the retroarc incipient foreland (Lossada et al., 2017; Reat and Fosdick, 2018).

Phases of flat-slab subduction are well recognized to correlate with spatial variations in Andean magmatism and deformation (Gutscher et al., 2000; Jordan et al., 1983; Ramos et al., 2002; Ramos and Folguera, 2009). Early Miocene subduction shallowing to 10° is synchronous with a sharp decrease in zircon εHf to negative values and corresponding decrease in zircon Th/U ratios towards <1. By 12 Ma the margin has progressed to flat-slab subduction conditions (<5°) characterized by waning magmatism, extremely broad volcanism (800 km), and isotopic pull down in both zircon εHf and U/Th ratios (< 0.6). The Miocene phase of flat-slab magmatism is concurrent with significant shortening (~150 km) across the retroarc region of Argentina (Jordan et al., 1993; Allmendinger et al., 1990; Fosdick et al., 2014; Capaldi et al., in press). The spatial, temporal, and isotopic constraints on magmatism exhibits a strong correlation between upper-plate deformation and subduction angle (Horton, 2018).

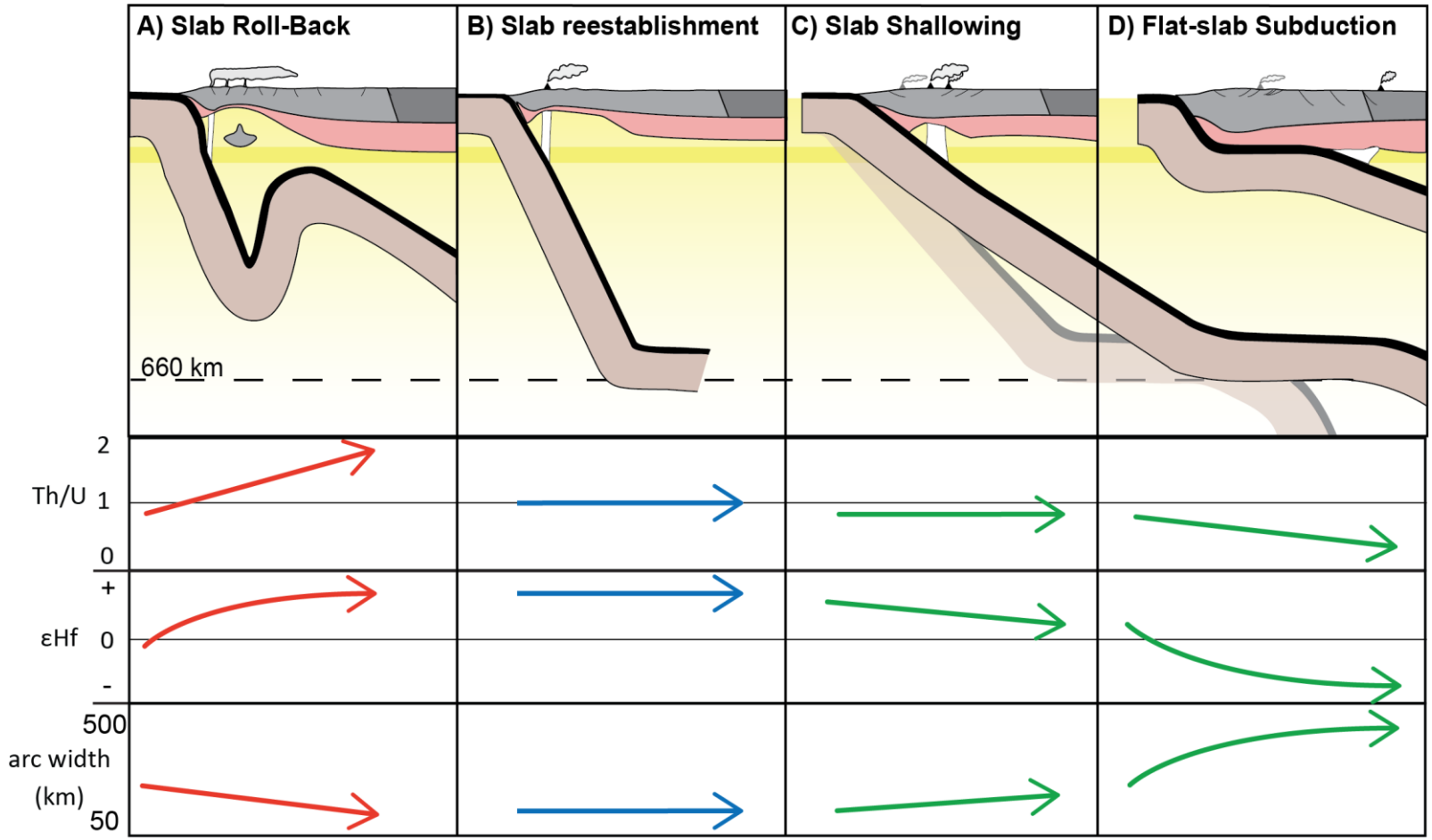
A) Slab Roll-Back
B) Slab reestablishment
C) Slab Shallowing
D) Flat-slab Subduction
660 km
Th/U
2
1
0
εHf
+
0
-
arc width
(km)
500
50

Figure 1.10: Schematic diagram highlighting variation in geodynamic setting, predicted continental arc width, and zircon isotopic values. (A) Slab roll-back settings with large subduction angle produce narrow continental arcs, and juvenile zircon εHf and high >2 Th/U values. (B) Slab reestablishment into mantle transition zone with be indicated by normal arc widths and stable εHf and Th/U values. (C) Slab shallowing to lower subduction angles are associated with increase arc width, and decrease in εHf towards moderately evolved composition. (D) Flat-slab subduction is associated with large arc widths, highly evolved εHf and low Th/U values.

CONCLUSIONS

We investigated the detrital zircon record from strata in the southern Central Andes of Argentina and Chile to determine how the Andean margin evolved through time (Fig. 1). This study presents and leverages a comprehensive detrital zircon geochronological and isotopic dataset for grains ranging in age from Neoproterozoic to Neogene to evaluate a longer magmatic record that spans the entire Phanerozoic.

(1) the timing of subduction initiation and Cordilleran-type margin development along the Central to Southern Andean segment of western South America. Andean Cordilleran subduction, initiated in the Carboniferous, is characterized by trenchward (westward) migration in magmatism, which was interrupted by Permian-Triassic flat-slab subduction and post-orogenic collapse. Subduction continued through the Mesozoic as a cratonward (eastward) advance of the trench that was interrupted by Miocene-present flat-slab subduction.

(2) Combined detrital zircon U-Th-Pb and Hf isotopic datasets, represent powerful tools for evaluating long-term, regional geologic patterns and the processes of crustal addition, removal, and recycling that, in turn help resolve the onset of Andean subduction, the relationships and feedbacks among upper-and lower-plate processes, and (Fig. 1). Evaluating the operative spatial and temporal scales of arc magmatism provides a means to test proposals of high-flux events (HFEs) and magmatic lulls that may generate cyclical or punctuated arc tempos at regular or irregular recurrence intervals (deSilva et al., 20; Patterson, et al.,). Zircon Th/U values can serve, in part, as proxies for tectonic regime, with elevated Th/U (>1.0) broadly correlative with extensional phases and low Th/U (0.1-

1.0) correspond to contractional phases of orogenesis (Barth et al., 2013; McKay et al., 2018). Additionally, studies have shown that low zircon Th/U ratios (<0.10) are likely associated with metamorphic crystallization, and that zircon Th/U increases with decreasing host rock SiO2 content, such that zircon from granitic rocks have distinctly lower (between 0.55 and 0.80) ratios, whereas zircon from gabbroic rocks has Th/U ratios that are largely higher (between 0.8 and 1.2; Kirkland et al., 2015; Yakymchuk et al., 2018). Zircon Hf isotopic signatures can record positive εHf values that reflect juvenile crustal material originating from melts of primitive mantle origin, or negative εHf values indicative of melts derived from older recycled crustal material (Hildreth and Moorbath, 1988; Belousova et al., 2002; Kemp et al., 2009). Using magmatism bedrock age and location datasets provides constraints on continental arc width which can be inverted to calculate an estimate on subduction angle width (Fig. 1).

(3) In Cordilleran or Andean orogenic systems, the dynamics of ocean-continent subduction can induce coupled interactions between the subducting lower plate and overriding upper plate, with implications for tectonic regime, deformation modes, and associated sedimentary basin evolution (Dickinson, 2004; Ramos, 2009; Ingersoll, 2011; Yonkee and Weil, 2015; Horton, 2018a; Fig. 1). Recent studies describing the mechanism that drive Cordilleran evolution include Cordilleran Cyclicity Model involving feedbacks among magmatism and the orogenic wedge to occur cyclically over 30-40 Myr (Haschke et al., 2002; 2006; DeCelles et al., 2009; 2015). Recent geodynamics models predict overriding plate response to the down-going plate interacting and anchoring into the lower mantel by shortening progressively on 50 to 200 myr timescales from anchoring to

orogenesis. (Faccena et al., 2017; Schellart et al., 2017; Chen et al., 2019). The relative angle of subduction dictates the degree of mechanical coupling between the over-ridding plate and down-going plate (Heuret and Lallemand, 2005; Ramos, 2010; Martinod et al., 2010; Horton, 2018b).

CHAPTER 2: NEOGENE RETROARC FORELAND BASIN EVOLUTION, SEDIMENT ROUTING, AND MAGMATISM IN RESPONSE TO FLAT-SLAB SUBDUCTION, WESTERN ARGENTINA

ABSTRACT

The effects of flat-slab subduction on mountain building, arc magmatism, and basin evolution are fundamental to convergent-margin tectonics, with implications for potential feedbacks among geodynamic, magmatic, and surface processes. New stratigraphic and geochronological constraints on sedimentation and magmatism in the southern central Andes of western Argentina (30.5°S) reveal Neogene shifts in volcanism, foreland/hinterland deposition, sediment provenance, and basin accumulation rates as the retroarc region was structurally partitioned before and during slab flattening. Detrital zircon U-Pb age distributions from the western (Calingasta hinterland basin), central (Talacasto and Albarracín wedge-top basins), and eastern (Bermejo foreland basin) segments of the retroarc basin system in western Argentina record syndepositional volcanism and unroofing of multiple tectonic provinces. Initial shortening-related exhumation of the Principal Cordillera at 24-17 Ma is represented in the Talacasto basin by accumulation of distal eolian deposits bearing Oligocene-Eocene detrital zircons derived from the Andean magmatic arc. The Calingasta basin recorded volcanism and basement-involved shortening of the Frontal Cordillera at ~17-11 Ma, as marked by an upward coarsening succession of fluvial to alluvial-fan deposits with a sustained zircon age component that matches pervasive Permian-Triassic bedrock in the hinterland. Subsequent thin-skinned shortening in the Precordillera fold-thrust belt at 11-5 Ma exhumed Calingasta

and Talacasto basin fill and induced cratonward (eastward) advance of flexural subsidence into the Bermejo foreland basin. The continuous Bermejo foreland basin was structurally partitioned as the Sierras Pampeanas basement-involved foreland uplifts transformed the large Andean sourced fluvial megafan sediment routing network to a series of smaller proximal alluvial fan systems along the uplift flanks. Sequential unroofing of the Principal Cordillera (24-17 Ma), Frontal Cordillera (17-11 Ma), Precordillera (11-5 Ma), and Sierras Pampeanas foreland uplifts (5-0 Ma), was marked at 12-10 Ma by significant changes in depocenter location, and sediment provenance, along with an eastward inboard sweep of volcanism (~400 km), that coincided with the inception of flat-slab subduction at -31° latitude. Collectively, shifting patterns of Andean erosion and sedimentation recorded the late Miocene initiation of shallow to flat-slab subduction and increased plate coupling, as expressed in the intensification and eastward advance of magmatism, shortening, and foreland basin subsidence.

INTRODUCTION

Geodynamic models and past geologic examples suggest that many ocean-continent convergent plate boundaries experience shifts to near-horizontal or flat subduction at some point during their history (Gurnis, 1992; Dickinson and Snyder, 1978; Ramos et al., 2002). Potential drivers of flat slab subduction are numerous, and include accelerated relative convergence, rapid trenchward advance of the overriding plate, mantle wedge dynamic pressure (slab suction), and subduction of positively buoyant oceanic lithosphere of anomalously low density, large thickness, or young age (Jarrard, 1986; van

Hunen, et al., 2002; Iaffaldano et al., 2006; Guillaume et al., 2009; Schellart et al., 2007). Many studies have observed temporal relationships among shallowing subduction, inboard advance of arc magmatism, and shutoff of the former magmatic arc (e.g., Coney and Reynolds, 1977; Coney, 1978; Dickinson and Snyder, 1978; Humphreys, 1995; Constenius, 1996; Saleeby, 2003). This time-space record of subduction-related volcanism has enabled researchers to track the locus of dehydration melting and thereby the geometry and location of the inboard hinge of the slab (marking the boundary between flat and steep slab subduction).

The Pampean flat-slab subduction system of Chile-Argentina is a segment of the Nazca-South American plate boundary that is characterized by modern shallow subduction angle, a spatial gap in active Andean volcanism (27-33˚S), and distal foreland basement uplifts of the Sierras Pampeanas potentially driven by subduction of the Juan Fernandez ridge (Fig. 1; Barazangi and Isacks, 1976; Cahill and Isacks, 1992; Jordan et al., 1983; Alvarado et al., 2009). Remaining questions focus on the impact of shallow subduction on the retroarc processes of magmatism, deformation, and basin evolution.

For example, does the record of arc magmatism support proposed/theoretical models of inboard advance/sweep of magmatism and abandonment of the former arcs? This issue is fundamental to evaluating plate reconstructions (Yanez et al., 2001; Ramos et al., 2002; Ramos and Folguera, 2009) and possibly complicated by the role of inherited structures.

Further, how do hinterland records of deformation and exhumation compare to the sedimentary record of the foreland? Previous studies have suggested accelerated shortening

in the Precordillera as a response to slab shallowing (Jordan et al., 1993; Hilley et al., 2004; Allmendinger and Judge, 2014; Levina et al., 2014; Fosdick et al., 2015). There remain uncertain temporal relationships among slab position, slab dip, shortening rate, and uplift of the Sierras Pampeanas (Ortiz et al., 2015; Goddard-Stevens and Carrapa, 2018). Whether these structural domains formed in response to coeval or discrete phases of shortening is fundamental to understanding the effect of flat-slab subduction and the process of mechanical coupling between the subduction plate and deformation history and strain accommodation in the overriding plate.

Finally, what was the response of foreland basin system to Andean deformation? There is an active debate as to whether the foreland basin records increased subsidence (largely dynamic), diminished subsidence, or even uplift (largely dynamic) (Davila et al., 2010; Finzel et al., 2011).

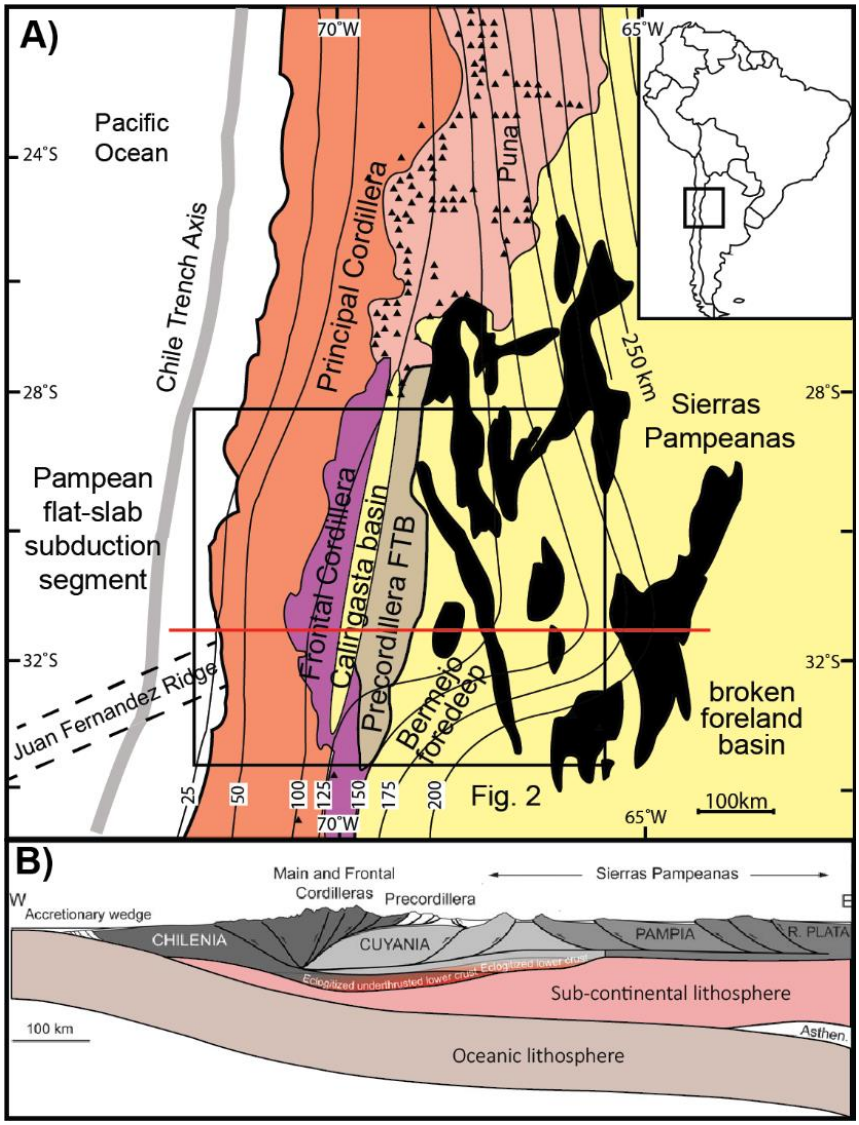

Figure 2.1: (A) Tectonic map of the southern Central Andes displaying major geologic provinces in the Pampean flat-slab segment of western Argentina and Northern Chile, with contoured depths (in kilometers) to the subducted Nazca plate (after Ramos et al., 2002). (B) East-west crustal cross section showing various Andean ranges and proposed basement terranes of the South American plate at this latitude (from Bellahsen, et al., 2016).

This study presents new stratigraphic, sedimentologic, and geochronometric constraints on Cenozoic magmatism, foreland basin evolution, and upper crustal exhumation in the southern central Andes of western Argentina (30.5°S) to evaluate Neogene changes in volcanism, depositional systems, sediment routing, basin subsidence accumulation rates, and deformation patterns in the retroarc region. We focus on the Argentina retroarc basins that are situated above the Chilean-Pampean flat slab segment of the southern Central Andes ~28-33°S (Fig. 1). The sedimentary record spans along a 175 km west-east transect that involves four key basin systems: 1) the hinterland Calingasta basin setting between the thick-skinned Principal Cordillera and thin-skinned Precordillera, 2) the wedge-top in the Precordillera fold-thrust belt and Eastern Precordillera back-thrust, 3) the Bermejo foreland depocenter between the Precordillera and Sierras Pampeanas basement uplifts, and 4) broken foreland basin adjacent to Sierras Pampeanas ranges (Fig. 2). Constraining changes to sediment routing among these nonmarine basins affords the opportunity to identify the structural partitioning of the retroarc region during slab flattening. The retroarc foreland basin record of Argentina, combined with a suite of new detrital zircon U-Pb geochronological results, provides a chronostratigraphic framework to track shifts in Andean arc magmatism, shortening, and erosion during a Neogene phase of Andean flat-slab subduction.

GEOLOGIC FRAMEWORK

Various tectonic events along the western South American margin at 33°S are expressed in the geologic record as four tectonic provinces from west to east: (1) Principal

Cordillera of the High Andes, (2) Frontal Cordillera (3), Precordillera fold-thrust belt, and (4) Sierras Pampeanas (Fig. 1).

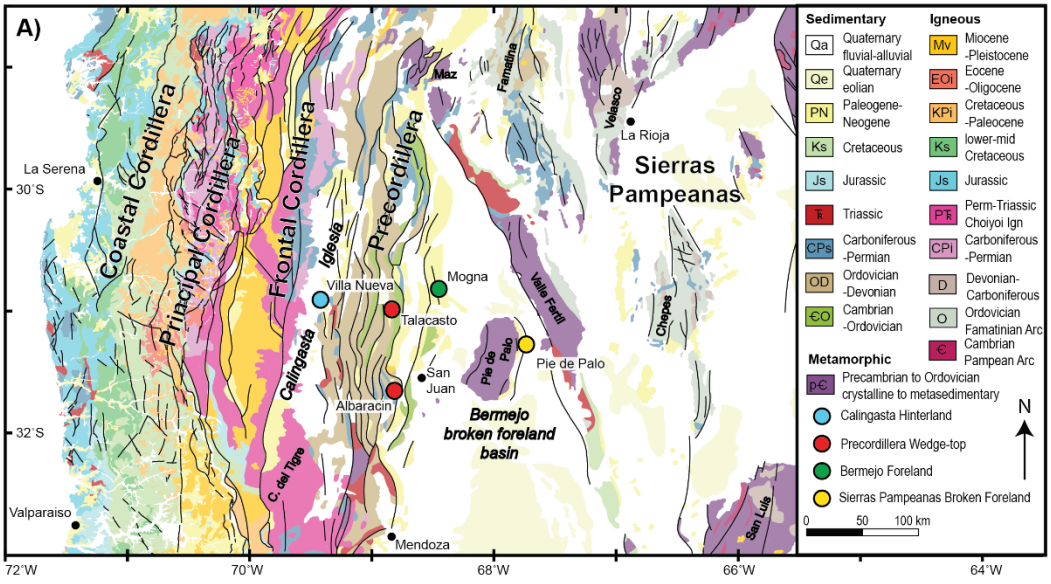

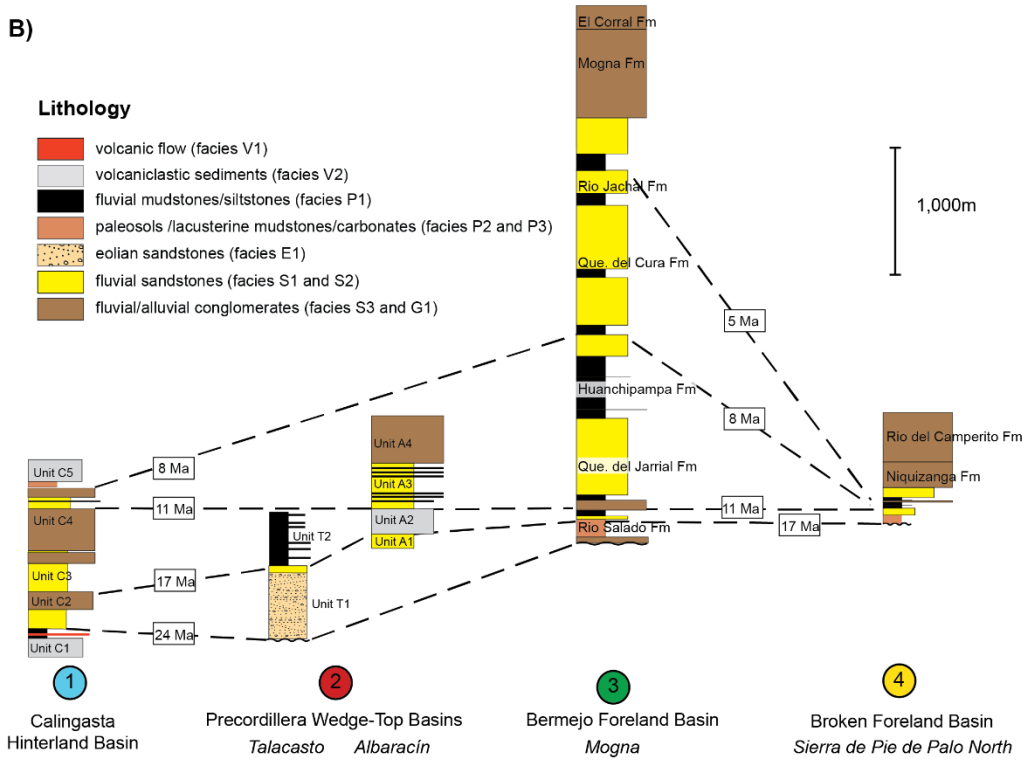

Figure 2.2: Geologic map of Argentina and Chile (-28.5 to -33˚S) displaying major tectonic provinces (Coastal Cordillera, Principal Cordillera, Frontal Cordillera, Calingasta-Iglesia hinterland basin, Precordillera fold-thrust belt, Bermejo foreland basin, and Sierras Pampeanas uplifts). (B) Schematic stratigraphic sections and correlated timelines across the Argentina retroarc basin system.

(1) Jurassic to Paleogene (201-24 Ma) igneous arc rocks across Coastal Cordillera in Chile and Carboniferous to Triassic (350-225 Ma) include principally granitic/granodioritic intrusions and their andesite extrusive counterparts, both associated with development of the Andean magmatic arc (Haschke et al., 2006; Charrier et al., 2015).

(2) The Calingasta-Iglesia hinterland basin system (Fig. 2B) is structurally bound to the west by the Frontal Cordillera along the western alluvial-valley margin (Beer et al., 1990; Ramos et al., 1996; Cristallini and Ramos, 2001; Fig. 2). The Carboniferous-Triassic (330- 242 Ma) igneous complexes, which form a large component of the High Andes and within the Frontal Cordillera including the Elqui–Limarí and Chollay batholiths (Herve et al., 2014). Subsequent Permian-Triassic (280 to 248 Ma) magmatism, represented by intrusive and extrusive units of the Choiyoi Igneous Province, marks post-orogenic extension and ignimbrite flareup (Kay et al., 1989; Mpodozis and Kay, 1992; Kleinman and Japas, 2009).

(3) The Calingasta basin is structurally bound in the east and separated from the Bermejo Basin (eastern foreland) by the Argentina Precordillera fold-thrust belt involving a > 6 km thick Cambrian to Devonian marine clastic and carbonate succession (Fig. 2; von Gosen, 1992; Ramos, 1999). Over 100 km of E-W shortening was accommodated by imbricate thrust sheets above a ~12 km deep decollement (von Gosen, 1992; Cristallini and Ramos, 2000; Allmendinger and Judge, 2014; Fosdick et al., 2015). Within the Precordillera thrust sheets are intervening wedge-top basins (Talacasto and Albaracín) that were once apart of a continuous retroarc foreland basin prior to mid Miocene deformation across the Precordillera (Fig. 2B; Verges, et al., 2001; Levina et al., 2014). The Bermejo

Basin to the east has been extensively studied as a classic retroarc flexural foreland basin, and contains thick sedimentary deposits of mostly Oligocene-Miocene non-marine strata (Fig. 2; Johnson et al., 1986; Jordan et al., 1993; 2001). The Bermejo basin strata outcrop along a north trending, west verging fold-thrust belt of the Eastern Precordillera that includes the Mogna anticline and type stratigraphic section (Fig. 2B; Zapata and Allmendinger, 1996; Milana et al., 2003).

(4) To the east, the Bermejo Basin is bounded by the Sierras Pampeanas, a series of roughly north-trending basement-involved uplifts, including the Sierra de Valle Fértil and Sierra de Pie de Palo at 30° to 32°S latitude (Fig. 2; Jordan and Allmendinger, 1986; Ortiz et al., 2015). On the eastern flank of Sierra Pie de Palo are exposures of Neogene strata incorporated in complex hanging wall back thrust structures that kinematically link to deep (~30 km) basement involved structures (Cuerda et al., 1983; Bellahsen, et al., 2016). Precambrian to Ordovician igneous and metamorphic belts preserved across the Sierras Pampeanas developed during eastward subduction and related arc magmatism and tectonism during the Pampean (555-515 Ma) and Famatinian (495-460 Ma) phases, interpreted as resulting from the of accretion of Laurentian derived terranes (MARA, Cuyania, and Chilenea) to the Gondwana margin (Schwartz et al., 2008; Ducea, et al., 2010; Thomas et al., 2015; Rapela, et al., 2016).

ANDEAN RETROARC BASIN STRATIGRAPHY

We conducted field mapping and sedimentary facies analysis of a 1580 m thick composite stratigraphic section measured in two localities in the hinterland Calingasta

basin (Villa Nueva section, Figs. 2 and 3a) and a 750 m thick section (northern Sierra Pie de Palo, Figs. 2 and 4b) measured in the distal Bermejo Basin within the Sierras Pampeanas province of basement-involved uplifts. Lithologic descriptions, bed thicknesses, facies, and sedimentary structures were described at decimeter scale. These new stratigraphic sections are compared with previous descriptions from Precordillera wedge-top basins in the Talacasto and Albarracín section localities (Figs. 2, 3b, 3c; Vergés et al., 2001; Levina et al., 2014), and Bermejo foreland basin section across the Mogna anticline (Figs. 2, 4a; Milana et al., 2003). Sandstone samples from new and previously studied Calingasta, Bermejo and Sierras Pampeanas sections were collected for detrital zircon U-Pb geochronology, and where preserved, paleoflow directions were determined from imbricated conglomerate clasts and the limbs of trough cross stratification in each section (plotted as rose diagrams, Figs. 3 and 4; Supp Data 1). Characteristic lithofacies for the strata were compiled from Miall (1978), Milana, (1991), Horton and DeCelles, (2001), Milana et al., (2003), Vergés et al., 2001, and Levina et al., (2014) (Fig. 5; Table 1).

Table 1: Summary of facies associations and interpretations

Facies Association	Lithofacies	Description	Occurrence
V1: Volcanic flow, surge, and fall deposits	Pm, Ps	Primary volcanic deposits	Units C1, C5
V2: Hyperconcentrated sheet flows from Lahars	Sm, Sh, Gmg, Ss, Sl, Sm	White to gray tuffaceous beds strucutreless to horizontally bedded, normally gradded. Outsized cobble to boulder clast. Laterally continuous over 10's m with scour surfaces uncommon. Local clast-supported streamlined lags.	Units C1, C5, A2 and Huachipampa Fm.
P1: paleosols in overbank area	Fm, Fl	reddish marron to moderate pink mudstone and siltstone; beds 0.1-3 m thick; no primary sedimentary structures; highly bioturbated; gypsum veins, minor root traces, mudcracks, and carbonate nodules.	Calingasta:Unit C2 Bermejo: Middle Rio Salado fm, L Quebrada del Jarillal
P2: playa lake deposits	Fl	thinly laminated to structureless limestone and gypsum beds 0.2 to 1.5 m thick.	Units C5, T3 and A1, Huachipampa fm, Quebrada del Cura, M Rio Jachal Fm.
P3: Overbank Floodplain	Fl, Fr	laminated, green to reddish orange, thinly interbedded clays, silts, and sands 0.1-0.3 m thick;basal contacts gradational with underlying unit (facies S1 and S2)	Units C5, T3 and A1, Huachipampa fm, Quebrada del Cura, M Rio Jachal Fm.
E1: Eolian deposits	St	Tan pinkish to greenish, thick sandstone deposits with large-scale cross stratification.	Unit T1 and T2
S1: Crevasse splay deposits	Sr, Sh, Ss, St, St, Sl, Sp	Thin, laterally continuous, tan-brown, fine- to medium grained sandstone; beds 0.1-0.5 m thick; interbedded non erosional basal contacts; ripple cross-stratified and low-angle cross stratification.	T3 and A1, Huachipampa fm
S2: Fluvial channel deposits; fluvial-mega fan	Sp, Gt	1-10 m thick bodies of lenticular, buff tan, medium to coarse grained or conglomeratic sandstone; beds 0.8-4.0 m thick; erosional basal contacts (commonly lined by siltsone intraclast); upward fining; trough cross-stratification; parallel lamination; ripple lamination; soft sediment deformation and dewatering structures; local bioturbation; commonly occurs as basal unit of basal unit of fining-upward packages capped by units of facies 2 and 3.	Quebrada del Jarillal Fm, Quebrada del Cura Fm, and Rio Jachal
S3: Large fluvial channel deposits	Sl,Ss,St Gp, Gh, Gm	2-50 m thick bodies of well-organized, sandy, pebble to small boulder conglomerate; beds 0.5-12 m thick; erosional basal contacts; upward fining; cross-stratified or sub horizontally stratified and imbricated	Units C2, C3, A3, L and U Rio Salado Fm, and Mogna Fm
G1: Proximal alluvial fan deposits	Gm	Pebble to cobble clast and matrix supported conglomerates with silt to medium sand matrix and pebbly sandstone lenses. Sub-angular clast	Unit A4 and El Corral Fm

Calingasta Hinterland Basin

Basal Volcaniclastic and Volcanic unit C1

A basal sequence of volcaniclastic deposits is locally found in the Calingasta section The lower Calingasta Unit C1 is characterized by a 200m upward fining sequence of volcaniclastic deposits that nonconformably overlie Permian Choiyoi group rhyolite, and the contact displays ~5 m of erosional relief. The lower 120 m are volcaniclastic clast- to matrix- supported pebble to cobble conglomerates that are weakly bedded, 0.5 to 0.8 m thick, with predominantly non-imbricated clasts. Matrix supported conglomerates are well cemented with weak to planar bedding and planar to locally erosive bases (Fig. 5A; facies association V2). These lower 120 m thick volcaniclastic deposits display a spectrum of matrix-supported debris flow to planar clast-supported hyperconcentrated sheet flows deposited during lahar transport (c.f. Smith and Lowe, 1991). In the upper Unit C1 section, a sequence of fine-grained, orange and grey silts with poorly developed and reworked bedding to planar lamination (Fl) represent highly bioturbated floodplain to paleosol facies (Facies association P1 and P3). Above this is a 5 m thick vesicular andesitic-basalt flow with a baked soil margin beneath, indicating Unit C1 preserves primary volcanic flows (Fig. 5B; Facies association V1). The Unit C1 volcaniclastic sequence may be the proximal equivalents to the Upper Puesto la Flecha Fm. playa lacustrine to fluvial facies in the Bermejo basin north of 33.5°S (Reat and Fosdick, 2018).

Braided Fluvial Deposits in units C2, C3, and C4

Calingasta Unit C2 is composed of an upward coarsening sequence (230 m) of stacked upward finning fluvial deposits (~20 m) that are brown-tan to grey-light grey. The base of the upward fining fluvial deposits consists of 5 to 2m thick, clast supported cobble conglomerates and poorly sorted silt to very coarse sand matrix, with common scour bases that normally grade to fine-medium sand (Fig. 5I; Facies association S3). These deposits show an up-section increase in grainsize and repeated strata of distal to proximal braided fluvial systems. Calingasta Unit C3 (Fig. 3) is 725 m thick with lithofacies similar to that of Unit C2 (Facies association S3), but preserving significantly more silt- to mud-dominated, planar laminated, fluvial overbank facies (facies association P3) in lower unit. Upper Calingasta Unit C3 (Fig. 3) exhibits similar facies to that of Unit C3 but lacks significant silt overbank and sand channels and composed of 1 to 3 m thick, normal graded, subangular to subrounded sandy conglomerate beds showing crude cross stratification with medium- to coarse-grained pebbly sandstone lenses, cobble conglomerates with subtle horizontal bedding, and matrix-supported pebble- to cobble-conglomerates with large angular clasts and significant tuffaceous matrix (Facies association S3).

Internally to externally drained basin: Unit C5

In the Calingasta basin the lower Unit C5 (Fig. 3) display interbedded laminated silts and thin, 0.3 m, buff grey carbonate layers with internally wavy geometry, and woody organic matter (Fig. 5C). The carbonate deposits are interpreted as an internally drained lacustrine system (Lithofacies association P2). Up section, Unit C5 transitions into a coarse-grained volcaniclastic sequence of light-grey medium sandstone, 0.7 to 1.2 m thick,

normal graded, with localized pebble to boulder lag of dominantly andesite clasts but containing gravel-sized pumice, that reaches 3m long and has 0.8m relief (Fig. 5A; Lithofacies association V1 and V2). The volcaniclastic sequence is capped by braided river deposits and alluvial fan gravels that are covered by younger Quaternary deposits (Fig. 5I).

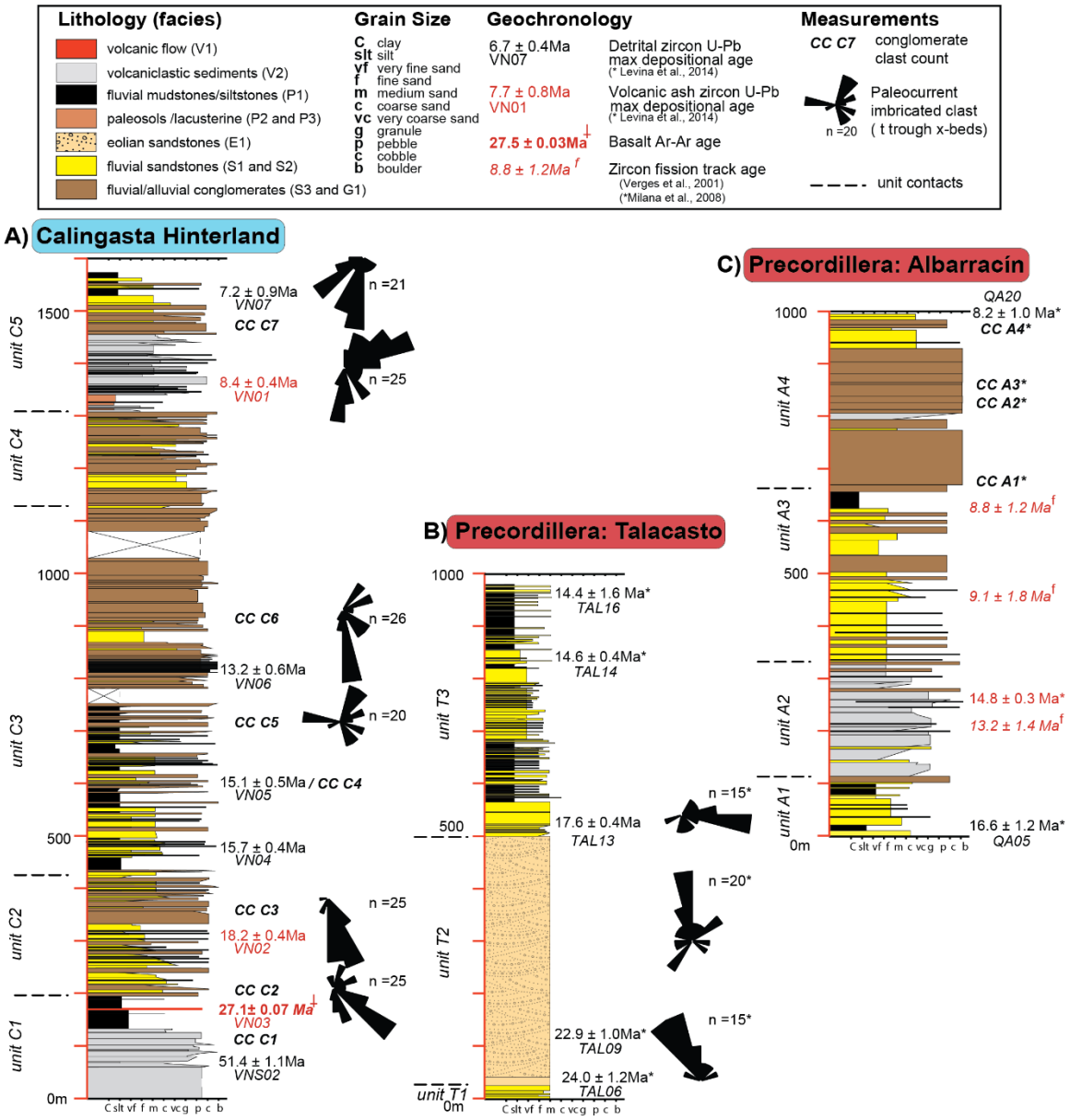

Figure 2.3: Stratigraphic sections from Argentina retroarc basins with paleocurrents, detrital zircon sample locations, clast count stations, and volcanic samples. (A) Calingasta hinterland, Villa Nueva measured section. (B) Precordillera wedge-top, Talacasto section (modified from Levina et al., 2014). (C) Precordillera wedge-top, Albarracín section (from Vergés et al., 2001; Levina et al., 2014). See Figure 2 for locations.

Precordillera Wedge-top Basins

Incipient Eolian system

Within the Precordillera, the sharp lower contacts of Talacasto Unit T2 is marked by very large scale cross-stratified sandstone, representing an abrupt change to a fully developed eolian system recorded by ~400–500m thick sequence of ~2–10 m thick cross beds with 1–25 cm thick foresets (Fig. 5G; Facies association E1; Milana et al. 1993, Levina et al., 2014). Paleoflow measurements from dune forecepts record a predominately northern paleowind direction (Fig. 3B). The Talacasto eolian deposits are sharply capped by fluvial deposits of unit T3, including a 1m mudstone and a 66m interval of medium- to coarse-grained, cross-bedded sandstone and interbeds of thin, dark red mudstone (Facies association S3 and P3).

Fluvial deposition

The Precordillera Talacasto Unit T3 (Fig. 3) consists of poorly lithified, thinly interbedded, poorly sorted red claystone, siltstone, and sandstone with small-scale cross lamination (lithofacies association P3). Interbedded sandstones include isolated channel deposits, cross-bedded sandstones with pebbly erosional bases, and mud rip-up clasts representing channel scours, and tabular, parallel-laminated sandstones representing distal crevasse splay deposits (Lithofacies association S1). Unit A1 in the Albarracín area has a higher proportion of thinly bedded, very fine-grained sandstones that represent deposition in distal fluvial floodplains, equivalent with Unit T2 (Figs. 3 and 7). Up section in Unit A2, a >200m interval of grayish white volcaniclastic deposits include thick-bedded, poorly sorted pyroclastic surge and ash flow deposits derived from nearby igneous centers and

intervals of ashfall deposits (Facies association V1; Levina et al., 2014). Additionally, fluvially reworked epiclastic sediment with sandy and pebbly detritus, and oversized boulder clast are common (Facies association V2). In upper Unit A2, gravel channel lenses and tabular pebbly sandstones become increasingly common as the volcaniclastic system transitioned to a fluvial environment (Figs. 3B and 7). Precordillera Units A3 and A4 (Fig. 3) attain a thickness of ~660 m and record the progradation of fluvial systems that contain volcaniclastic intervals toward the top (Vergés et al., 2001, Levina et al., 2014). These deposits are indicative of gravelly stream flows, sheet flows, and debris flows in an alluvial fan setting. The lack of upper Miocene (<8 Ma) deposits in the Precordillera sections (Fig. 3; Albarracin and Talacasto) suggest depositional waning and eventual shut-off as the Precordillera fold-thrust belt cannibalizes Cenozoic basin deposits as deformation propagates eastward (Jordan et al., 1993; Levina et al., 2014).

Bermejo Foreland Basin

Paleoflow reversal in Rio Salado Formation

Distally, the Bermejo foreland section in the Mogna anticline contains the lower Rio Salado Formation, which consists of a basal coarse-grained gravel to cobble, clast supported, imbricated deposit with lenses of sandstone with trough cross-bedding (Fig. 5H; Facies association S3). These fluvial deposits are characterized by W-NW paleocurrents and conglomerate composed of basement and Paleozoic clasts derived from the Sierras Pampeanas (Fig. 8). Overlying the basal Rio Salado conglomerates are reddish maroon, structureless muds and silts, with few desiccation cracks and abundant bioturbation,

interbedded with light green to white thin carbonate banks, in which stromatolytic structures have been described (Cuerda et al., 1979; Milana et al., 2003). Bioturbation is intense and creates homogeneous mudstones with some original structures preserved in silt with planar and ripple laminations (Fig. 5E; Facies association P1, P2, and P3), and interbedded bentonite ash layers (Facies association V1). The middle Rio Salado Formation is interpreted as a silty-playa lake depositional environment with periods of flooding and ash input, and interfingering floodplain facies of muddy plains and silty fluvial deposits (Milana et al., 2003). Up section the distal floodplain deposits transition to 2-3 m thick, laterally continuous, fine- to medium-grain sand complexes, with internal erosive bases and dominantly planar laminated and low-angle cross-beds (facies association S2). The upper Rio Salado Formation show a prominent upward coarsening sequence from flood plain and subordinate lacustrine facies to large gravel-rich fluvial systems and paleocurrent measurements from trough-cross strata that indicate a flow reversal to E-SE paleoflow (Fig. 4).

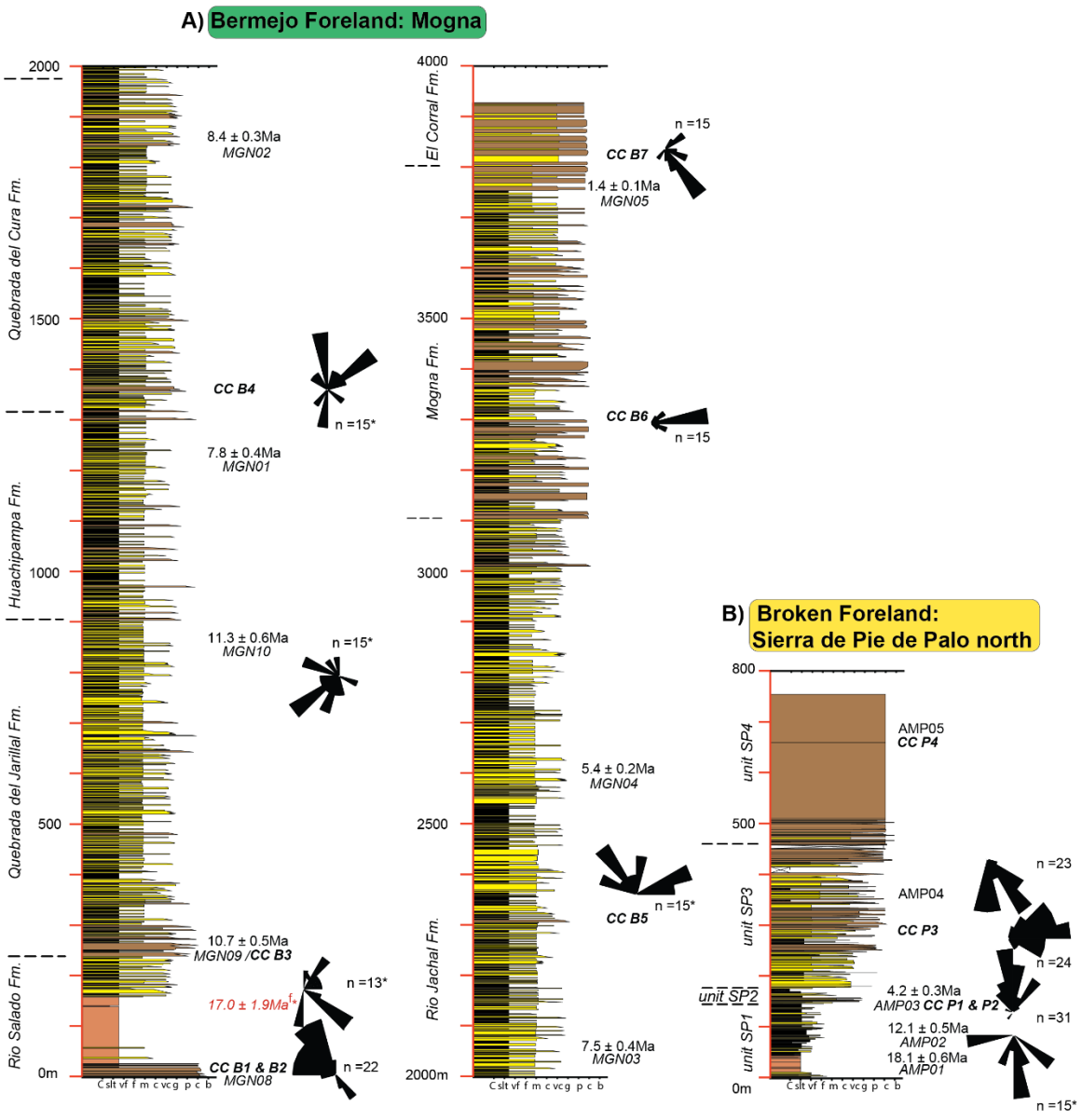

Figure 2.4: Stratigraphic sections from Argentina retroarc basins with paleocurrents, detrital zircon sample locations, clast count stations, and volcanic samples. (A) Bermejo foreland, Mogna measured section (from Milana et al., 2003). (B) Broken Foreland, Sierra Pie de Palo North section. See Figure 2 for locations.

Fluvial meganfan distributive system

The Quebrada de Jarillal Formation records a thick (650 m) sequence of medium sand comprising 3-4 m thick beds that can be amalgamated as 12-15 m multistoried sands, and is well sorted, low angle cross-bedded with frequent internal erosion surfaces with pebble to cobble lag (Fig. 5F; Facies association S2). The thick sand complexes are interbedded with up to 0.5m thick laterally continuous tabular sand bodies to 200m (Fig. 5F; lithofacies association S1) and homogenous mudstone with significant gypsum beds. The Quebrada de Jarillal Formation of the Bermejo basin (Fig. 4) records a key change in depositional environment, from a migrating braided-fluvial system to a large distributive fluvial mega-fan system.

Up section the Huachipampa Formation is dominantly highly bioturbated clayey-silt and silty-sand, completely homogenized with floating clasts, interbedded with channelized brown sand 2 to 3 m thick and 10-15 m to km wide, intense bioturbation, planar laminations, ripples, and rare low-angle cross beds (Facies association S2; Milana et al., 2003). The Huachipampa Formation records the first volcaniclastic sand in the section, comprised of interbedded tuffaceous sandstone, reworked pyroclastic material from upstream (Facies association V2).

The thick Bermejo foreland deposits (1800 m) comprising the upper Quebrada de Cura Fm. and lower Rio Jachal Fm. (Fig. 4) record similar distributive fluvial mega-fan facies as those within the Quebrada del Jarillal and Huachipampa Formations. The presence of green silts and fine sands, low gypsum content, and high bioturbation suggest minor playa lake deposition with good drainage and low evaporation rates (Milana et al., 2003).

Rio Jachal and Mogna Formations, consists of poorly sorted gravels with significant sandy matrix and planar laminated beds with oversized (25-30 cm) clasts. Sand intervals exhibit 0.3-0.4 m thick structureless to planar beds that amalgamate to form 2 to 6 m thick bodies with planar bases and gravel channel lag. Conglomeratic units have 2 to 12 m thick beds that are well sorted with imbricated, rounded clasts, and are laterally continuous >1 km, with interbedded minor sand trough and lenses (Milana et al., 2003). Sequences are typically normally graded with capping 1-2m fine sandy-silt that are laminated to structureless. The multistoried channels represent avulsion of ephemeral rivers with gravel units representing flooding events, indicative of main channels within the fluvial mega-fan system (Facies association S3 and G1; Horton and DeCelles, 2001; Milana et al., 2003). Up section, the El Corral Formation conglomerates were characterized by poorly sorted oversized clasts generated by hyperconcentrated flow along a steep depositional slope, with absent matrix having been cleared by residual currents (Facies association G2).

Broken Foreland Basin

Distal axial fluvial system

Eastward, deposition initiates in the Sierras Pampeanas depocenter, as recorded by stratigraphically condensed (100 m), upward coarsening trend similar to that in the proximal Bermejo foreland (Fig. 4). The basal Unit SP1 (90 m; Fig. 4) is dominantly tan-red-green silty-mudstones with planar lamination and common gypsum beds similar to that of the middle Rio Salado Formation (Fig. 5D; Lithofacies association P1 and P2). The silty floodplain and playa lake deposits are interbedded with 0.2 m silty-fine sands with ripple

and planar laminations, capped by 3 m thick amalgamated fine to medium sand bodies with trough-cross beds, normal grading and scour bases. Distally in the Sierras Pampeanas, upper Unit SP1 (Fig. 4) is a thin condensed sequence (50 m) of maroon-gray-tan silt composed of 1 m thick intervals of poorly sorted, very fine sands and silts with planar laminations, normally graded to red muds. (Facies association P1 and P2). The fine-grained deposition and thin tabular sand beds suggest that distributive fluvial system terminated into a distal axial river floodplain that flowed S-SE (Fig. 4B). Unit SP2 overlies the fine grained fluvial succession of Unit SP1, and is the first appearance of (m) well-rounded pebble to gravel conglomerates with paleoflow measurements towards the north.

Proximal alluvial deposits

Units SP3 and SP4 (Fig. 4) consist of normally graded, 5 to 7m thick composite sequences of 1.5 m thick basal brown-grey, poorly-sorted and lithic rich pebble to cobble conglomerate with cm-scale scour surfaces that are laterally continuous over 10's m. These grade into 0.3 to 0.5 m thick, medium to coarse sand that is planar to low-angle cross-bedded, and capped by poorly-sorted silts (Facies association S3). Uppermost Unit SP4 consist of sub-angular, poorly sorted, cobble to boulder conglomerates from debris flow dominated transport, that represent the progradation of proximal alluvial fans derived from the nearby Sierra de Pie de Palo basement uplift (Figs. 3 and 7).

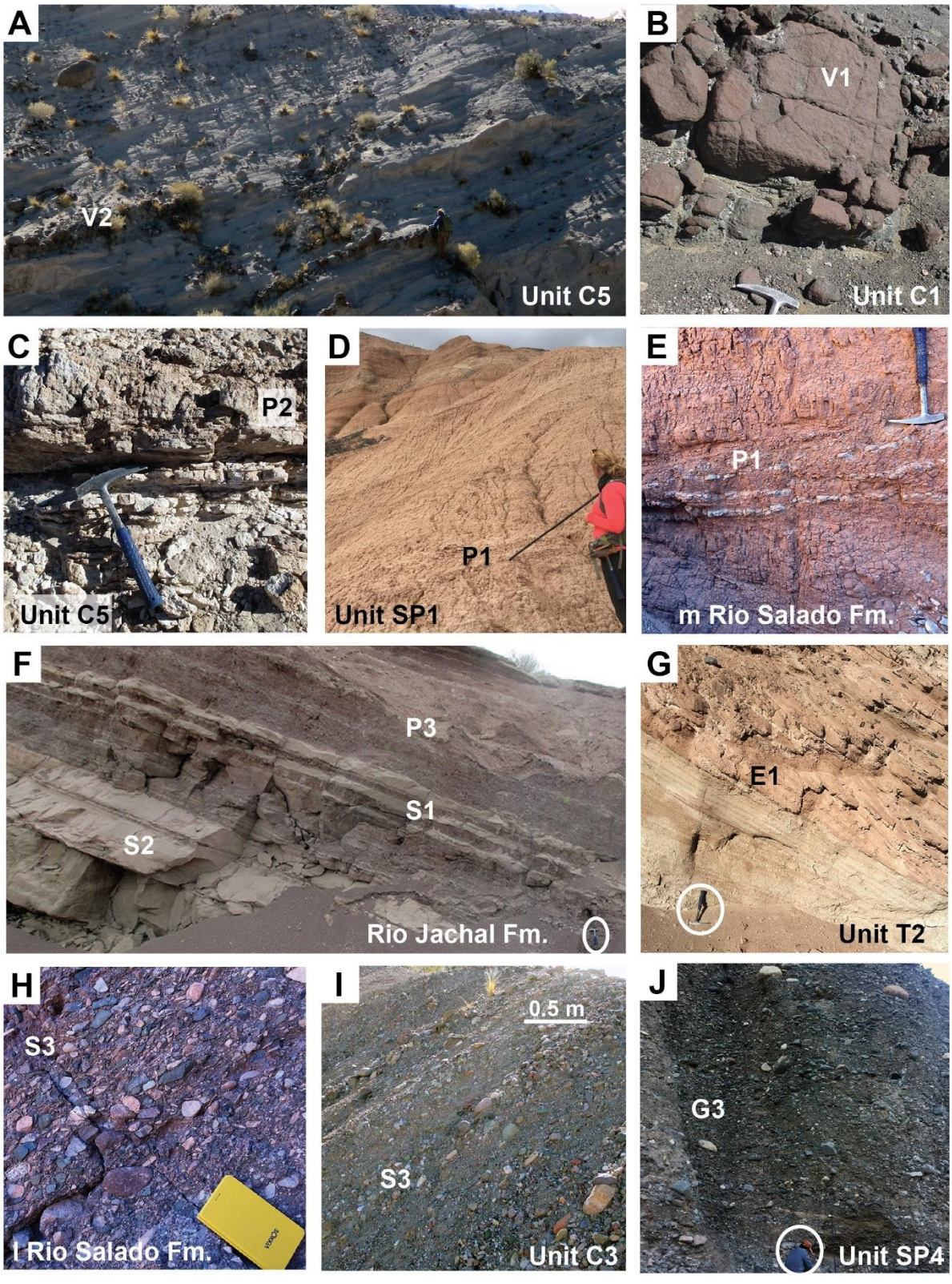
A
V2
Unit C5
B
V1
Unit C1
C
P2
Unit C5
D
P1
Unit SP1
E
P1
m Rio Salado Fm.
F
P3
S1
S2
Rio Jachal Fm.
G
E1
Unit T2
H
S3
l Rio Salado Fm.
I
0.5 m
S3
Unit C3
J
G3
Unit SP4

Figure 2.5: Field photographs of sedimentary deposits of the Calingasta, Precordillera, Bermejo, and Sierras Pampeanas sections. (A) White, buff-grey volcanoclastic sequence of normally graded, laminated medium sandstone, with localized pebble to boulder lag that reach 3m long and 0.8m thick comprised of andesite clasts composition, and gravel sized pumice clast. (B) Basalt flow sample VN03 and interbedded siltstones. (C) Interbedded laminated silts and thin 0.3 m buff grey carbonate layers with internally wavy geometry, and woody organic matter. (D) Tan-red-green silty-mudstones with planar lamination and common gypsum beds. (E) Red-maroon massive and bioturbated muds with abundant gypsum intervals with small carbonate concretions. (F) Tan-brown amalgamated sand channels (facies association S2), laterally continuous tabular crevasse splay sand bodies (facies association S1), and interbedded overbank fine laminated silts and muds (facies association P3). (G) Large cross-bedded eolian sandstones. (H) Clast-supported gravel-cobble conglomerate of metamorphic clast. (I) Normal graded sandy conglomerate beds with crude stratification (Unit C3; facies association S3). (J) Poorly sorted cobble-boulder conglomerate debris flow deposits (Unit SP4; facies association G1).

CHRONOSTRATIGRAPHY

Basalt Flow ^{40}Ar-^{39}Ar Geochronology

A single andesitic basalt flow was sampled (VN03; Fig. 5B) from the basal section of the Calingasta basin (Unit C1) and analyzed by the $^{40}Ar/^{39}Ar$ step-heating method. The groundmass VN03 age spectrum displays an initial apparent age of ~40 Ma for the lowest temperature step during which limited gas (<15%) was released. The remaining 12 steps show a sharp decrease in apparent age, yielding consistent ages in the 26-30 Ma range. A uniform flat segment defined by the final 7 steps yields a weighted mean plateau age of 27.05 ± 0.07 Ma (see Supplemental Material). The K/Ca spectrum is typical of groundmass with values near 1 for the first half of the spectrum before diminishing to values near 0.1 for the higher temperature steps. The isochron suggests excess argon for steps A-E with an initial $^{40}Ar/^{36}Ar$ trapped component of 312 ± 1 Ma and an isochron age of 27.5 ± 0.03 Ma (Supplemental Table 2) that is near the weighted mean plateau age and the integrated (total gas) age of 27.65 ± 0.02 Ma. Therefore, the initial old ages (>28 Ma) from the step-heat analyses are considered the probable result of excess argon and the plateau age of 27.05 ± 0.07 Ma represents the more accurate age for emplacement of the basalt flow within the Calingasta basin.

Detrital Zircon U-Pb Geochronology

We collected and completed U-Pb geochronological analyses of 19 Cenozoic sandstones and 2 ash fall tuff samples from the Calingasta, Precordilleran, Bermejo basins (Figs. 3 and 4). Standard mineral separation techniques included crushing and grinding, water table, heavy-liquid density, and magnetic susceptibility separations for all samples.

Nonmagnetic heavy mineral separates were poured onto double sided tape on 1" epoxy resin mounts, then zircon grains were chosen randomly for analysis by laser ablation–inductively coupled plasma–mass spectrometry (LA-ICP-MS) to obtain zircon U-Pb ages. At least 120 zircon grains were analyzed per sample to resolve significant age components (Vermeesch, 2012). For volcanic samples, ~30 analyses were carried out on euhedral, inclusion- and fracture-free zircon grains that were individually picked and mounted (e.g., Levina et al., 2014). Sample mounts were loaded into a large-volume Helex sample cell and analyzed with a single-collector, magnetic sector Element2 ICP-MS with a PhotonMachine Analyte G.2 excimer laser (Hart et al., 2016; Horton et al. 2016). Corrections for depth-dependent, elemental and isotopic fractionation were performed using zircon standards GJ1 (600.4 ± 0.1 Ma; Jackson et al., 2004), and secondary standards Plesovice (PL-1; 337.2 ± 0.4 Ma; Slama et al., 2008) and 91500 (1065 Ma; Wiedenbeck et al., 1995; Supplemental Table 3).

Zircon U-Pb ages and 2σ errors are reported for analyses with less than 10% $^{206}Pb/^{238}U$ uncertainties, less than 20% discordance, and less than 5% reverse discordance. Reported dates and percent discordance for grains younger than 850 Ma are $^{206}Pb/^{238}U$ ages and discordance $^{206}Pb/^{238}U$ vs. $^{207}Pb/^{235}U$ and for grains older than 850 Ma ages are $^{207}Pb/^{206}Pb$ dates with $^{206}Pb/^{238}U$ vs. $^{207}Pb/^{206}Pb$. Discordance filters for Miocene zircon dates (<23 Ma) were expanded to incorporate ages with less than 20% $^{206}Pb/^{238}U$ uncertainties, and less than 50% discordance $^{206}Pb/^{238}U$. The 50% discordance filter was applied to prevent biasing of the age distribution due to preferential exclusion of young grains with higher ^{207}Pb and associated calculated $^{207}Pb/^{235}U$ which is systematically older

than measured $^{206}Pb/^{238}U$ (Supp material 3). Results are organized in stratigraphic order and U-Pb ages for individual samples are displayed as a probability density plots (PDP) with histogram age bins. Cenozoic, Paleozoic, and Neo-Mesoproterozoic ages dominate (>95%) the zircon age components. The Neogene sandstone samples are displayed as probability density functions from 0 to 66 Ma with 5 Myr histogram age bins to discern diagnostic Andean arc zircon age components and syndepositional ages, and zircon ages 200 to 1500 Ma are plotted with 25 Myr histogram age bins exhibiting sediment recycling from older bedrock units.

Maximum Depositional Age

A maximum depositional age (MDA) for each detrital sandstone sample and two tuffaceous samples are derived from the calculated weighted mean age of the youngest grain cluster overlapping by 2σ concordant U-Pb ages following established approaches (Dickinson and Gehrels, 2009; Couts et al., 2019). When no two or more grains overlapped by 2σ, then the youngest single grain was selected as the maximum depositional age (Supp material 4). All MDA results are labeled with sample name at the sampled stratigraphic level (Figs. 3 and 4). Neogene sandstone samples with no Cenozoic grains include MGN08 from lower Rio Salado Formation conglomerates in Bermejo Foreland section (Fig. 4A) and samples AMP04 and AMP05 from unit SP3 and SP4 in Broken Foreland section (Fig. 4B). Sandstone samples that yielded Cenozoic grains but not in a predicted younging up section trend are only found in the Bermejo foreland section and include samples MGN10 (11.3±0.6 Ma), and MGN02 (7.8±0.4 Ma) (Fig. 4A).

Zircon Th/U Ratios

Zircon radiogenic isotopes such as Th/U system provide constraints on crystallization conditions and magmatic sources, which are sensitive proxies to upper-plate stress regimes. Zircon Th/U ratios have been shown to be associated with tectonic stress-regime, where elevated Th/U ratios (>1.0) broadly correlate with extensional magmatism and low Th/U ratios (0.1-1.0) correspond to contractional orogenesis (McKay et al., 2018). Additionally, tracking arc width through time provides a general estimate of subduction angle to constrain spatial-temporal relationships among lower-plate variation and upper-plate processes (i.e. deformation, erosion, and sediment routing). We incorporate all Cenozoic age DZ results into a spatial-temporal compilation to better understand feedbacks and relationships among subduction, arc magmatism, Andean orogenesis, and basin evolution.

SEDIMENT PROVENANCE

Conglomerate Clast Composition

Clast compositional data were measured at 18 stations within the Calingasta, Bermejo, and Sierras Pampeanas sections and compared to clast compositions from Albarracín section by Vergés and others (2001) and Levina and others (2014). Clast are grouped into seven lithologic categories: (1) Maroon to red-orange felsic volcanic rock from the Permian-Triassic rhyolite suite; (2) Leucocratic granite to diorite Carboniferous to Triassic and Cenozoic arc rocks; (3) Grey to melanocratic, fine-grained to porphyritic, intermediate volcanics from Cenozoic volcanic sequences; (4) Green to tan metamorphosed sandstone and siltstone from Silurian to Devonian marine stratigraphy; (5)

Red to brown siltstone and sandstones from non-marine Carboniferous to Triassic non-marine stratigraphy; (6) Blue-grey limestones, buff grey-white dolostones, and black chert from Cambrian-Ordovician carbonate platform sequences; (7) Metamorphic lithologies, including green-grey feldspathic amphibolite gneisses, green-grey muscovite-biotite-feldspar schist, white marbles, and vein quartz from Precambrian to Ordovician basement assemblages.

Conglomerate clast counts in the hinterland Calingasta basin section display a continuous bi-modal distribution of felsic and intermediate volcanics throughout the section with the appearance of Paleozoic metasedimentary lithologies (station C4) by the middle Miocene (Fig. 8A). Precordillera clast counts from Albarracín unit A4 display change from dominantly Paleozoic metasedimentary clast to an increase in felsic volcanic clasts, which records increased input form Frontal Cordillera sources within the upper-Miocene stratigraphic interval (Fig. 8B; Levina et al., 2014). Bermejo basin clast compositions from the Oligocene to Lower Miocene Rio Salado Formation (stations B1 and B2) exhibit mixed metamorphic (32%), red sandstone (24%), green-brown metasedimentary rocks (23%), and blue-grey carbonates (19%) indicative of sources from eastern igneous-metamorphic basement and overlying Paleozoic to Triassic strata. Up section, in the middle to upper Miocene Quebrada del Jarillal, Huachipampa, Quebrada del Cura and Rio Jachal Formations (station B3, B4, and B5), the clast composition is dominated by bimodal distribution of felsic volcanic (30-49%) and metasedimentary (34-54%) clasts, and minor contributions of intermediate/mafic volcanics (11-14%) and vein quartz (2-11%) clast (Fig. 8C). Appearance of volcanic and metasedimentary lithologies

indicates erosional unroofing of both Frontal and Precordilleran sources. The Pliocene Mogna and El Corral formations (stations B6 and B7) exhibit dominant abundance of felsic volcanic clasts (38-44%), subordinate (30-36%) metasedimentary clasts, minor (8-9%) carbonate clasts, felsic intrusive (6-8%), and intermediate volcanics clasts (3-12%). The appearance of carbonate clasts records erosion from Cambrian-Ordovician strata found in proximal Eastern Precordillera thrust sheets. Sierras Pampeanas Upper-Miocene conglomerate composition (station SP1) initially contains felsic and intermediate volcanic clasts (38%) derived from Andean sources that shifts in the Pliocene to igneous and metamorphic (dominantly amphibolite gneiss) clast (>80%), recording the erosion of metamorphic and igneous basement sources from the proximally uplifting Sierra de Pie de Palo (Fig. 8D).

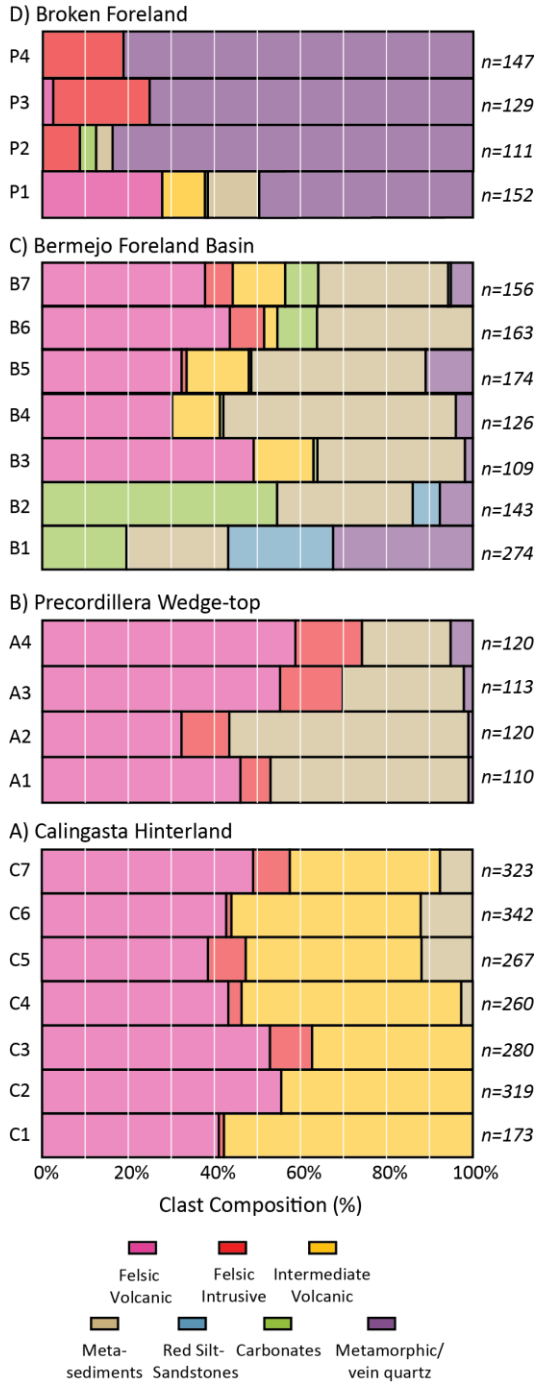
D) Broken Foreland
P4
P3
P2
P1
n=147
n=129
n=111
n=152
C) Bermejo Foreland Basin
B7
B6
B5
B4
B3
B2
B1
n=156
n=163
n=174
n=126
n=109
n=143
n=274
B) Precordillera Wedge-top
A4
A3
A2
A1
n=120
n=113
n=120
n=110
A) Calingasta Hinterland
C7
C6
C5
C4
C3
C2
C1
n=323
n=342
n=267
n=260
n=280
n=319
n=173
0%
20%
40%
60%
80%
100%
Clast Composition (%)
Felsic Volcanic
Felsic Intrusive
Intermediate Volcanic
Meta-sediments
Red Silt-Sandstones
Carbonates
Metamorphic/ vein quartz

Figure 2.6: Conglomerate clast compositions and lithologic groups from Cenozoic Argentina retroarc deposits, see figures 3 and 4 for sample locations. (A) Calingasta hinterland. (B) Precordillera Albarracín section. (C) Bermejo foreland basin. (D) broken foreland.

Detrital Zircon U-Pb Geochronology

The complex Phanerozoic history along the Argentina and Chile South American margin resulted in numerous igneous and metamorphic events that generated distinct lithological and radiogenic isotopic signatures throughout the region (Fig.2). Detrital zircon (DZ) U-Pb provenance analyses from modern river sands draining main sediment source regions of the Principal Cordillera, Frontal Cordillera, Precordillera, and Sierras Pampeanas have been completed by Pepper et al., 2016; and Capaldi et al., 2017 (Fig. 9). This modern river dataset from the retroarc region of Argentina specifically characterizes the sediment provenance in numerous modern basin settings (i.e. hinterland, wedge-top, foreland, and broken foreland), allowing understanding of how variations in erosion, zircon fertility, and lithologic erodibility impacts provenance signatures in the sedimentary record (Capaldi et al., 2017). Zircon U-Pb age distributions are described in terms of specific age components or modes, which include, from oldest to youngest (Fig. 9):

(1) Proterozoic 1450-925 Ma basement ages have a minor component of 1450–1350 Ma ages and dominate 1200-925 Ma Sunsás (Grenville) age component were recycled from the Laurentian-derived Cuyania terrane and metamorphic basement in the western Sierras Pampeanas (Ramos, 2004, 2009; Bahlburg et al., 2009; Rapela et al., 2016).

(2) Eastern Sierras Pampeanas 725-510 Ma age group is composed of minor 725-540 Ma age component sourced from metasedimentary sequences (Puncoviscana Formation) and dominant 538-515 Ma age peak from Pampean arc magmatism both derived from the eastern Sierras Pampeanas (Rapela et al., 2007; Schwartz et al., 2008).

(3) Western Sierras Pampeanas 510-380 Ma age group is derived from sources throughout the western Sierras Pampeanas involving 495-440 Ma Famatinian continentatl arc rocks and subsequent 460-385 Ma metamorphic assemblages (Mulcahy et al., 2014; Otamendi et al., 2017).

(4) Cordillera Late Paleozoic 350-280 Ma zircon ages are from minor 350-335 Ma igneous suite spanning the western Sierras Pampeanas to eastern Frontal Cordillera and dominate 340–280 Ma Carboniferous arc rocks of the Principal and Frontal Cordilleras (Mpodozis and Kay, 1992; Dahlquist et al., 2013).

(5) Cordillera Permian-Triassic 280-225 Ma age group includes dominate Choiyoi Igneous Complex (280-240 Ma) and subsequent Triassic plutons exposed in the Frontal Cordillera (Fig. 1; Mpodozis and Kay, 1992; del Rey et al., 2016).

(6) Chilean Andean Arc 201-23 Ma Jurassic to Paleogene Andean arc volcanic and volcanic rocks of the Chile Coastal and Principal Cordilleras (Parada, 1990; Kay et al., 2005; Mackaman-Lofland et al., 2019).

(7) Argentina Andean Arc 23-0 Ma Miocene to Quaternary Andean arc volcanism and volcaniclastic rocks of the Principal Cordillera, Frontal Cordillera, and isolated volcanic centers spanning the Precordillera, and Sierras Pampeanas (Fig. 2A; Jones et al., 2014; Kay and Mpodozis, 2001).

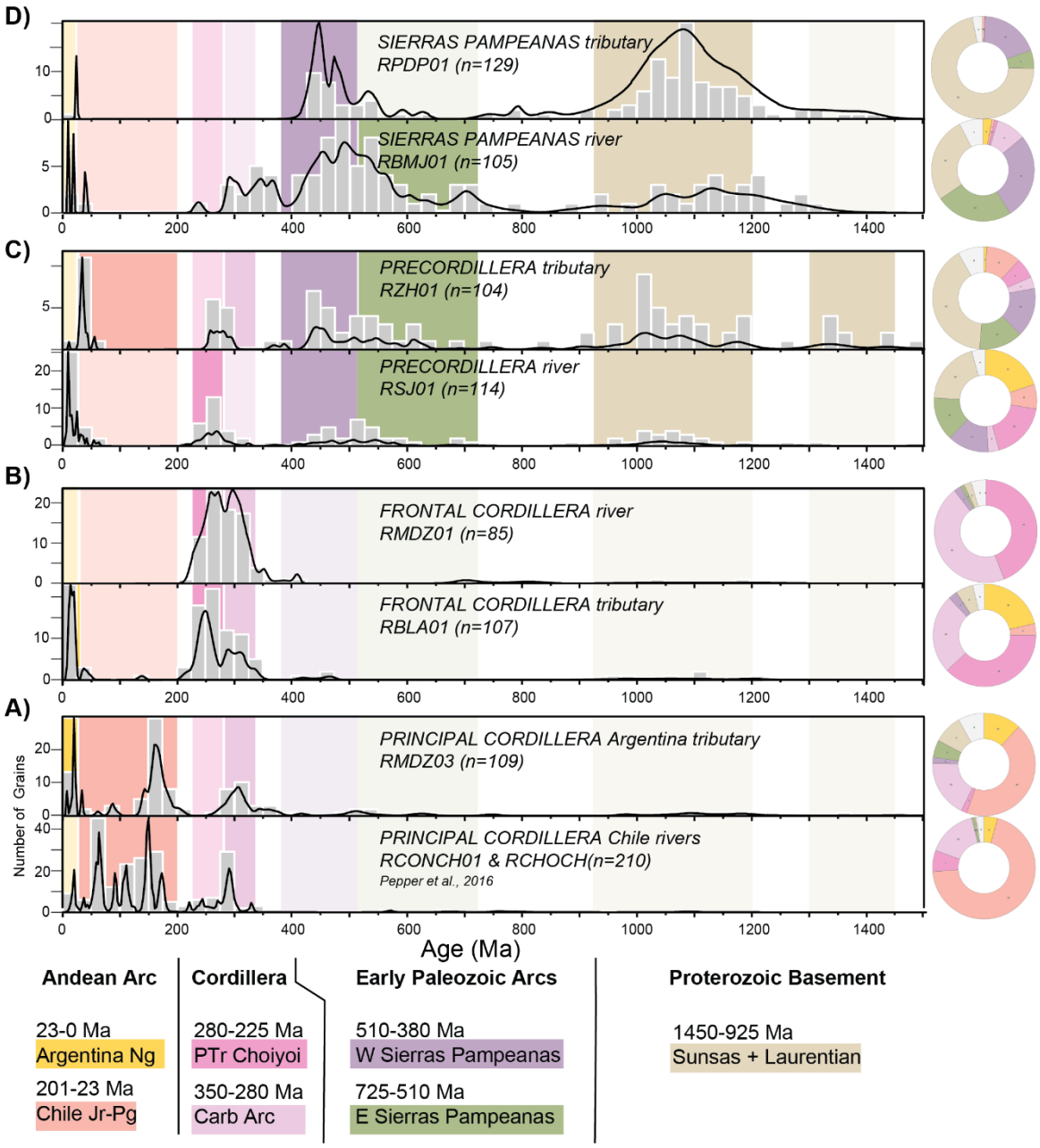
D)
SIERRAS PAMPEANAS tributary
RPDP01 (n=129)
SIERRAS PAMPEANAS river
RBMJ01 (n=105)
C)
PRECORDILLERA tributary
RZH01 (n=104)
PRECORDILLERA river
RSJ01 (n=114)
B)
FRONTAL CORDILLERA river
RMDZ01 (n=85)
FRONTAL CORDILLERA tributary
RBLA01 (n=107)
A)
PRINCIPAL CORDILLERA Argentina tributary
RMDZ03 (n=109)
PRINCIPAL CORDILLERA Chile rivers
RCONCH01 & RCHOCH(n=210)
Pepper et al., 2016
Number of Grains
Age (Ma)
Andean Arc
23-0 Ma
Argentina Ng
201-23 Ma
Chile Jr-Pg
Cordillera
280-225 Ma
PTr Choiyoi
350-280 Ma
Carb Arc
Early Paleozoic Arcs
510-380 Ma
W Sierras Pampeanas
725-510 Ma
E Sierras Pampeanas
Proterozoic Basement
1450-925 Ma
Sunsas + Laurentian

Figure 2.7: Comparative plot of detrital zircon U-Pb age distributions for modern river sands, depicted as age histograms and relative probability density curves, with emphasis on key age populations (color shading). Pie diagrams represent percent abundance of key age populations in each sample. Samples from Capaldi et al., 2017, unless otherwise specified. (A) Principal Cordillera rivers. (B) Frontal Cordillera rivers. (C) Precordillera rivers. (D) Sierras Pampeanas rivers.

Modern river characterization of sediment sources

Integrating modern river sand DZ age distributions with observed variation in bedrock sources and geomorphology across the retroarc region establishes predictable sediment provenance trends to compare to the Cenozoic sedimentary record. Detrital zircon U-Pb age distributions for modern river sands in the south Central Andes demonstrate distinctive age signatures from several competing sediment sources: (1) Andean Arc, (2) Principal Cordillera and Frontal Cordillera, (3) Precordillera and recycled Cenozoic basin strata, and (4) Sierras Pampeanas basement block uplifts (Fig. 7). This well characterized modern baseline provides a unique opportunity to apply DZ provenance to predict tectonic unroofing patters, track erosion, and reconstruct the sediment routing system during Neogene flat-slab subduction.

Principal Cordillera Rivers: The Principal Cordillera along the Chile-Argentina border consists of Mesozoic magmatic arc rocks, deformed Mesozoic foreland and rift-related strata, and Cenozoic arc related sedimentary and volcanic rocks. Modern river sand DZ exhibit a dominant age peak of 180-150 Ma, consistent with Jurassic arc related volcanic and igneous units. Additional sources represented in the river sand U-Pb age spectra include <50 Ma Eocene-Miocene arc derived zircons, a broad population of 150-50 Ma ages from the Cretaceous-Paleocene arc, and a minor 350-280 Ma Carboniferous arc peak (Fig. 7A). The Principal Cordillera is dominated by 180-50 Ma zircons, which are diagnostic of Jurassic to Paleocene arc sources now found in Chile and the High Andes of Argentina.

Frontal Cordillera Rivers: The hinterland is predominately composed of Frontal Cordillera thick-skinned blocks that exhume ~3 km thick Late Paleozoic–Triassic sequences of granodiorite intrusions and associated andesitic and rhyolitic lavas, ignimbrites, and pyroclastic rocks of the Choiyoi Group, and covered by Neogene Andean volcanic sequences of basaltic through rhyolitic compositions. The modern river drainage networks that drain Frontal Cordillera sources have unimodal to bimodal U-Pb age spectra that are dominated by a Permian-Triassic (280-225 Ma) population with subordinate (<23 Ma) Neogene arc contributions, and 350-280 Ma Carboniferous arc peaks (Fig. 7B). Predicted sedimentary unroofing sequence in the Frontal Cordillera involves initial erosion into Neogene volcanic cover (RBLA01) with subsequent increase erosion into Triassic-Carboniferous crystalline basement (RMDZ01) (Fig. 7B).

Precordillera Rivers: The fold-thrust belt province is composed of Paleozoic marine siliciclastic and carbonate platform sequences that were originally derived from source areas found in the eastern craton (Pampean, Famatinian, Sunsas igneous-metamorphic belts). Modern river DZ U-Pb results from the Precordillera main trunk river (RSJ01) show cosmopolitan age distributions with strong <50 Ma Eocene-Miocene arc, 280-225 Ma Permian-Triassic, and 350-280 Ma Carboniferous arc peaks, which indicating recycling from exhumed Neogene sedimentary rocks between thrust sheets (Capaldi et al., 2017). Additionally, sands from small axial tributary networks along the thrust sheet display significantly more older ages including 510-380 Ma Western Sierras Pampeanas, 725-510 Ma Eastern Sierras Pampeanas, 925-1450 Sunsas belt grains that represent sediment recycled from Paleozoic metasedimentary sequences of the thrust sheets (Fig.

7C). Predicted sedimentary unroofing sequence involves initial erosion of Neogene basin strata (RSJ01) then into underlying Paleozoic metasedimentary sequence (RZH01) (Fig. 7C).

Sierras Pampeanas Rivers: Distal modern river networks within the partitioned foreland drain large catchments that span axial river networks within the Sierras Pampeanas ranges. The flanking river network flows south along the Sierras Pampeanas western ranges, sourcing broadly folded Triassic-Jurassic fluvial red beds and overlying exhumed Precambrian-lower Paleozoic basement along Sierra Valle Fertile, and Sierra Pie de Palo uplifts (Fig. 2). Modern river sands show dominant 510-380 Ma western Sierras Pampeanas, 725-510 Ma Eastern Sierras Pampeanas, and 925-1200 Sunsas belt age components contributions from the basement cored uplifts, with minor Cordillera and Andean arc age distributions (< 350 Ma) from recycled overlying strata (Capaldi et al., 2017; Fig. 7D). Predicted sedimentary unroofing sequence involves initial erosion of Neogene basin strata and Mesozoic rift basins (RBMJ01) followed by erosion of underlying Paleozoic-Precambrian igneous-metamorphic basement rocks (RPDP01) (Fig. 7D).

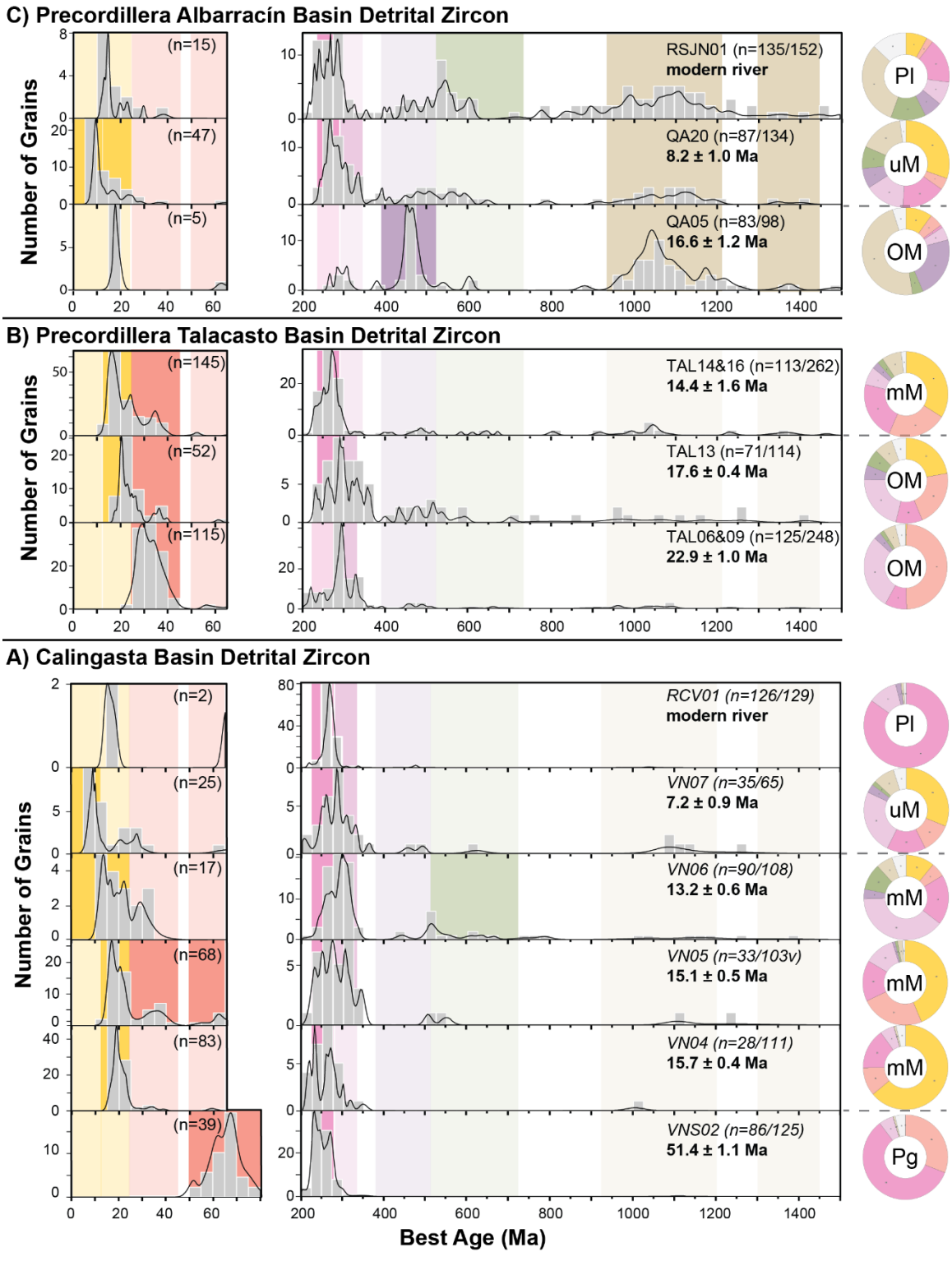
C) Precordillera Albarracín Basin Detrital Zircon
Number of Grains
(n=15)
(n=47)
(n=5)
RSJN01 (n=135/152)
modern river
QA20 (n=87/134)
8.2 ± 1.0 Ma
QA05 (n=83/98)
16.6 ± 1.2 Ma
Pl
uM
OM
B) Precordillera Talacasto Basin Detrital Zircon
Number of Grains
(n=145)
(n=52)
(n=115)
TAL14&16 (n=113/262)
14.4 ± 1.6 Ma
TAL13 (n=71/114)
17.6 ± 0.4 Ma
TAL06&09 (n=125/248)
22.9 ± 1.0 Ma
mM
OM
OM
A) Calingasta Basin Detrital Zircon
Number of Grains
(n=2)
(n=25)
(n=17)
(n=68)
(n=83)
(n=39)
RCV01 (n=126/129)
modern river
VN07 (n=35/65)
7.2 ± 0.9 Ma
VN06 (n=90/108)
13.2 ± 0.6 Ma
VN05 (n=33/103v)
15.1 ± 0.5 Ma
VN04 (n=28/111)
15.7 ± 0.4 Ma
VNS02 (n=86/125)
51.4 ± 1.1 Ma
Pl
uM
mM
mM
mM
Pg
Best Age (Ma)

Figure 2.8: Comparative plot of U-Pb age distributions for sandstone depicted as age histograms and relative probability density curves, with emphasis on diagnostic age populations (color shading). Pie diagrams represent percent abundance of key age populations in each sample. (A) Calingasta hinterland basin. (B) Precordillera Talacasto section (Levina et al., 2014). (C) Precordillera Albarracín section (Levina et al., 2014).

Cenozoic Sediment Provenance Trends

Integrating detrital zircon U-Pb maximum depositional age estimates, sandstone age distributions, and conglomerate clast count provide new constraints on Andean unroofing patterns and sediment routing evolution for the Cenozoic retroarc basin systems. We interpret five distinctive sediment provenance trends that include: (1) Localized Paleogene (**Pg**) sequence of deposits that record erosion in the Principal Cordillera. (2) Oligocene to lower Miocene (**OM**) strata derived from Principal and Frontal Cordillera sediment source regions, while Bermejo Basin and Precordillra basal deposits receive sediment from the eastern cratonic region. (3) Middle Miocene (**mM**) sediments record a second unroofing sequence from the Frontal Cordillera. (4) Upper Miocene (**uM**) strata predominately in the Bermejo foreland display numerous unroofing sequences from the Precordillera fold-thrust belt. (5) Pliocene to modern (**Pl**) sediment provenace indicate basins receive sediment from proximal erosional catchments as Sierras Pampeanas erode during uplifted across the Bermejo broken foreland.

***Paleogene* (>34 Ma):** Basal Calingasta unit C1 (VNS02; Fig. 9) detrital zircon U-Pb ages display Cretaceous to Paleocene population with a prominent peak at ~67 Ma, and a dominant 280-225 Ma Permian-Triassic age mode involving the Choiyoi igneous province, with peaks at 230 Ma and 270 Ma. The age signatures are indicative of sediment sources in the Principal Cordillera (Figs. 8A).

Oligocene-Lower Miocene (24-17 Ma): During the Oligocene to lower Miocene (**OM**) two distinct sediment sources are apparent from the provenance results. Western Andean sources from the Principal and Frontal Cordillera provide sediment into the orogen

parallel fluvial-eolian deposits from 23 to 17 Ma (Fig 8B. TAL06&09, TAL13). The basal eolian deposits within the Precordillera Talacasto section are dominated by Eocene-Oligocene and Carboniferous to Triassic zircon age populations, indicative of Principal Cordilleran rocks outcropping on the western Chilean side of the present-day Andean drainage divide (Fig. 2A). The fluvial sequence overlying the basal eolian sequence (Unit T2) displays a similar age distribution, but with an increase in Miocene Andean arc ages (TAL13). The second sediment source from the eastern cratonic region are recorded by basal deposits in Precordilleran (Albaracin), Beremjo foreland, and broken foreland depocenters (Figs. 8C, 9A, and 9B; QA05, MGN08, and AMP01). The Lower Miocene strata are dominated by older age distributions (>400 Ma) and sedimentary to metasedimentary conglomerate clast, and eastern paleoflows indicative of eastern cratonic sediment sources. Contrasting hinterland and cratonic sediment sources is common in incipient foreland deposits and indicative of growing topography in the hinterland that induces a flexural response and drives sediment accommodation across the retroarc foreland (Horton and DeCelles, 2001; Horton et al., 2018). Regional isostatic response to hinterland structural shortening can generate a flexural wave that can drive localized uplift (a forebulge) in the distal foreland region, which may explain the synchronous eastern derived cratonic sources and corresponding paleocurrent indicators that broadly show sources toward the northwest.

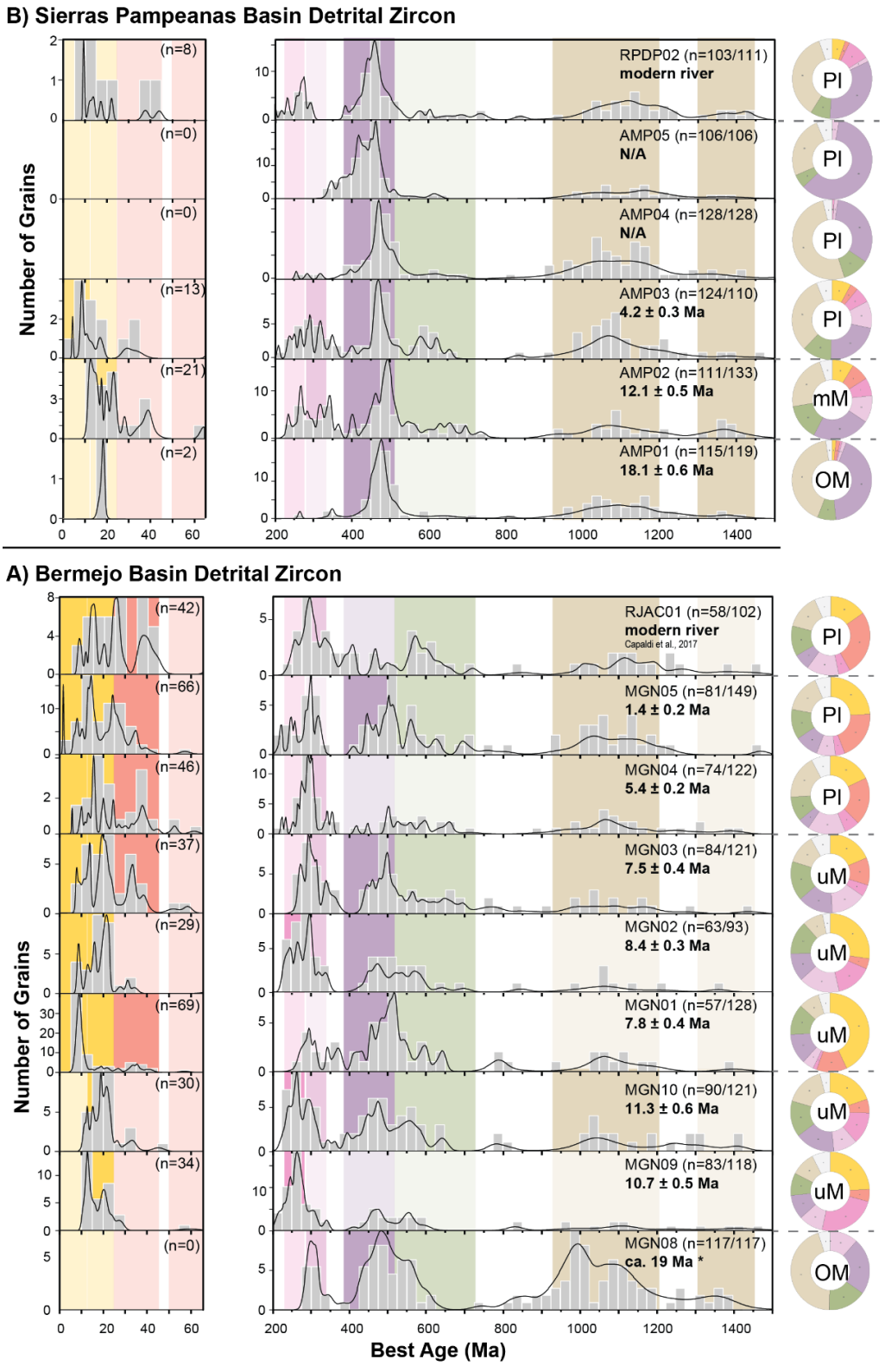
B) Sierras Pampeanas Basin Detrital Zircon
A) Bermejo Basin Detrital Zircon
Number of Grains
Best Age (Ma)
RPDP02 (n=103/111)
modern river
AMP05 (n=106/106)
N/A
AMP04 (n=128/128)
N/A
AMP03 (n=124/110)
4.2 ± 0.3 Ma
AMP02 (n=111/133)
12.1 ± 0.5 Ma
AMP01 (n=115/119)
18.1 ± 0.6 Ma
RJAC01 (n=58/102)
modern river
Capaldi et al., 2017
MGN05 (n=81/149)
1.4 ± 0.2 Ma
MGN04 (n=74/122)
5.4 ± 0.2 Ma
MGN03 (n=84/121)
7.5 ± 0.4 Ma
MGN02 (n=63/93)
8.4 ± 0.3 Ma
MGN01 (n=57/128)
7.8 ± 0.4 Ma
MGN10 (n=90/121)
11.3 ± 0.6 Ma
MGN09 (n=83/118)
10.7 ± 0.5 Ma
MGN08 (n=117/117)
ca. 19 Ma *
PI
mM
OM
uM

Figure 2.9. Comparative plot of U-Pb age distributions for sandstone depicted as age histograms and relative probability density curves, with emphasis on diagnostic age populations (color shading) emblematic of particular units. Pie diagrams represent percent abundance of key age populations in each sample. (A) Bermejo foreland samples. (B) Sierras Pampeanas broken foreland samples.

Middle Miocene (17-11 Ma): The regional Middle Miocene fluvial sequence records Frontal Cordillera unroofing in the Calingasta basin and subsequent progradation of the Cordilleran signal into the distal foreland region in the Bermejo basin. Frontal Cordilleran unroofing can be inferred by the DZ signature trends within Calingasta basin Unit C3 (Fig. 10: VN04, VN05, VN06) showing increased Carboniferous (350-280 Ma) component relative to the Permian-Triassic (280-225 Ma) age component. The up-section decrease in Argentina Neogene (<23 Ma) Andean age zircon is synchronous with an increase in Carboniferous to Triassic zircons, suggesting uplift driven denudation of Andean volcanic arc and volcaniclastic cover and erosion into underlying igneous basement of the Carboniferous arc and Permian-Triassic Choiyoi igneous units in the Frontal Cordillera. During 13 to 11 Ma the Andean Cordilleran age signature (0-350 Ma) is propagated from the Calingasta and Precordilleran (Talacasto) sections (VN06 and TAL14&16) and appears downstream within the Bermejo foreland (Mogna and Pie de Palo North) sections (MGN09 and AMP02) (Figs. 8 and 9).

Upper-Miocene (11-5 Ma): Upper-Miocene deposits in Calingasta basin continue to incorporate Cenozoic age zircons from proximal Andean volcanics and underlying Carboniferous to Triassic arc rocks of the Frontal Cordillera (Fig. 8A: VN07). Downstream provenance trends towards the foreland exhibit a decrease in the Andean zircon age populations (from > 50% to 25%) and an increase in older (>460 Ma) zircon age population (from 10% to >40%) (Figs. 10 and 11: QA20, MGN10, MGN01, MGN02, and MGN03). Fluvial mega-fan sequence in the Bermejo basin records mixed sediment provenance signatures as Precordillera shortening and erosion contribute 380-510 Ma, 510-725 Ma,

and 925-1450 Ma age components that are greater than the 0-23 Ma and 225-350 Ma age distributions derived from the Frontal Cordillera and Andean arc hinterland. The Upper-Miocene deposits in the Bermejo foreland basin display 2 up-section changes in zircon age distributions between 11-8 Ma (MGN09 and MGN10) and 8-5 Ma (MGN01, MGN02, and MGN03), which are characterized by increased older (> 460 Ma) zircon ages, decreased in carboniferous to Triassic (350-225 Ma) age components, and broadening of Cenozoic age distributions to older population than the maximum depositional age popultions. The up-section provenance changes are inferred to represent sedimentary unroofing and recycling of Cenozoic basin deposits that cover the Paleozoic metasedimentary sequence, as the Precordillera fold-thrust belt sequentially advances eastward.

Pliocene to Present (5-0 Ma) Pliocene deposits found in the Bermejo basin show characteristic unroofing of initial Cenozoic basin deposits in the Precordillera followed by an increase in sediment input from Paleozoic metasedimentary sources within the Precordillera (Fig. 9A; MGN04 and MGN05). A Similar unroofing pattern is recorded in Pliocene-Pleistocene deposits in the broken foreland depocenter (Pie de Palo North), where recycled Andean (<66 Ma) and Cordilleran (225-350 Ma) zircon ages (AMP03) are absent up-section as sediments are predominately sourced from proximal igneous and metamorphic basement rocks represented by dominant Western Sierras Pampeanas (510-380 Ma) zircon age components (AMP04 and AMP05). The up-section increase in older ages suggest initial uplift and erosion of Cenozoic basin deposits followed by exhumation of igneous and metamorphic basement sources uplifted along foreland basement involved Sierra de Pie de Palo within the western Sierras Pampeanas uplifts (Fig. 2). Modern rivers

in the Bermejo (RJAC01) and broken foreland (RPDP02) show the reappearance of Cordilleran (0-350 Ma) age zircons reflecting recent uplift and recycling of proximal Cenozoic foreland deposits (Fig. 9). The modern rivers eroding the Frontal Cordillera display an increase in Permian-Triassic (200-275 Ma) zircon grains, indicating recent exhumation in Frontal Cordillera province (Fig. 8A; RCV01).

DISCUSSION

Retroarc Basin Subsidence

The refined chronostratigraphic framework across the Calingasta, Precordillera, and Bermejo basins from new and published maximum depositional ages, dated volcanic deposits, and magnetic polarity stratigraphy (Milana et al., 2003) constrain the timing, location, and relative rates of sediment deposition (Fig. 10). The retroarc sediment accumulation record is categorized into four distinct phases: Oligocene-early Miocene proximal basins accumulation, middle Miocene regional accumulation, late Miocene basin reorganization, and Pliocene to present foreland accumulation, with the average accumulation rates are not corrected for compaction.

Calingasta and Precordillera deposition initiated by ~24 Ma and recorded low accumulation rates (29 to 86 m/Myr), yielding stratigraphic thicknesses of <500 m by 17 Ma (Fig. 6: Calingasta and Talacasto). By ~17 Ma the depocenter broadened eastward from the arc proximal Calingasta basin to the distal Bermejo foreland within the Sierras Pampeanas region that initially accommodated < 500 m in the first 6 Myr of foreland deposition. The basin architecture inferred from higher accumulation rates (83 to 100

m/Myr) at 18 to 11 Ma suggest a foredeep depocenter located in the western sections (Calingasta, Talacasto). In contrast, eastern sections of Bermejo basin fill (Albarracín, Bermejo and Sierras Pampeanas sections) display low accumulation rates (18 to 43 m/Myr) indicative of a distal foredeep or potential forebulge to backbulge depocenters. Basin-wide accommodation of lower Miocene deposits across Calingasta, Precordillera, and into the distal Bermejo depocenter demonstrates a single continuous flexural foreland basin system. The Calingasta and Precordillera sections higher sediment accumulation reflect foredeep depocenters, whereas the Bermejo section reflects a distal foredeep that onlaps eastern cratonic regions with the Sierras Pampeanas stratigraphic section depositing in a low accommodation setting potentially within a forebuldge depocenter.

By the early late Miocene (11 to 8 Ma), Calingasta and Precordillera depocenters display similar mean accumulation rates (97 to 171 m/Myr), and the Bermejo foreland becomes the locus of deposition, with high sediment accumulation rates (383 m/Myr) (Fig. 6). Uncharacteristically, deposition did not migrate progressively eastward to the distal Bermejo basin within the Sierras Pampeanas broken foreland, which underwent severely reduced sedimentation rate (7 m/Myr) during 12 to 4 Ma. The spatial variability of accumulation rates that span orders of magnitudes, indicates structural partitioning of the basins by the Precordillera fold-thrust belt. This suggests both Calingasta and Precordillera sections transitioned to wedge-top depozones, and the Bermejo basin rapidly accumulated sediment in a foredeep setting (Jordan et al., 1993). The lack of late Miocene accommodation within the Sierras Pampeanas broken foreland suggest a fixed forebulge or structural high that inhibits accommodation in the distal foreland.

Pliocene deposits in the distal foreland Sierras Pampeanas section record significantly increased sediment accumulation rates from 7 m/Myr to 143 m/Myr (Fig. 10: Sierras Pampeanas). Sediment accommodation along the proximal Sierra Pie de Palo basement uplift is indicative of a broken foreland basin setting (Jordan, 1995). Uppermost Miocene to Pleistocene stratigraphy from the Bermejo foreland continues to record high sediment accumulation rates (250 m/Myr). Isolated basin accumulation within the foreland and lack of deposition within the hinterland and wedge-top basins indicate a completely structurally partitioned basin system by the Pliocene.

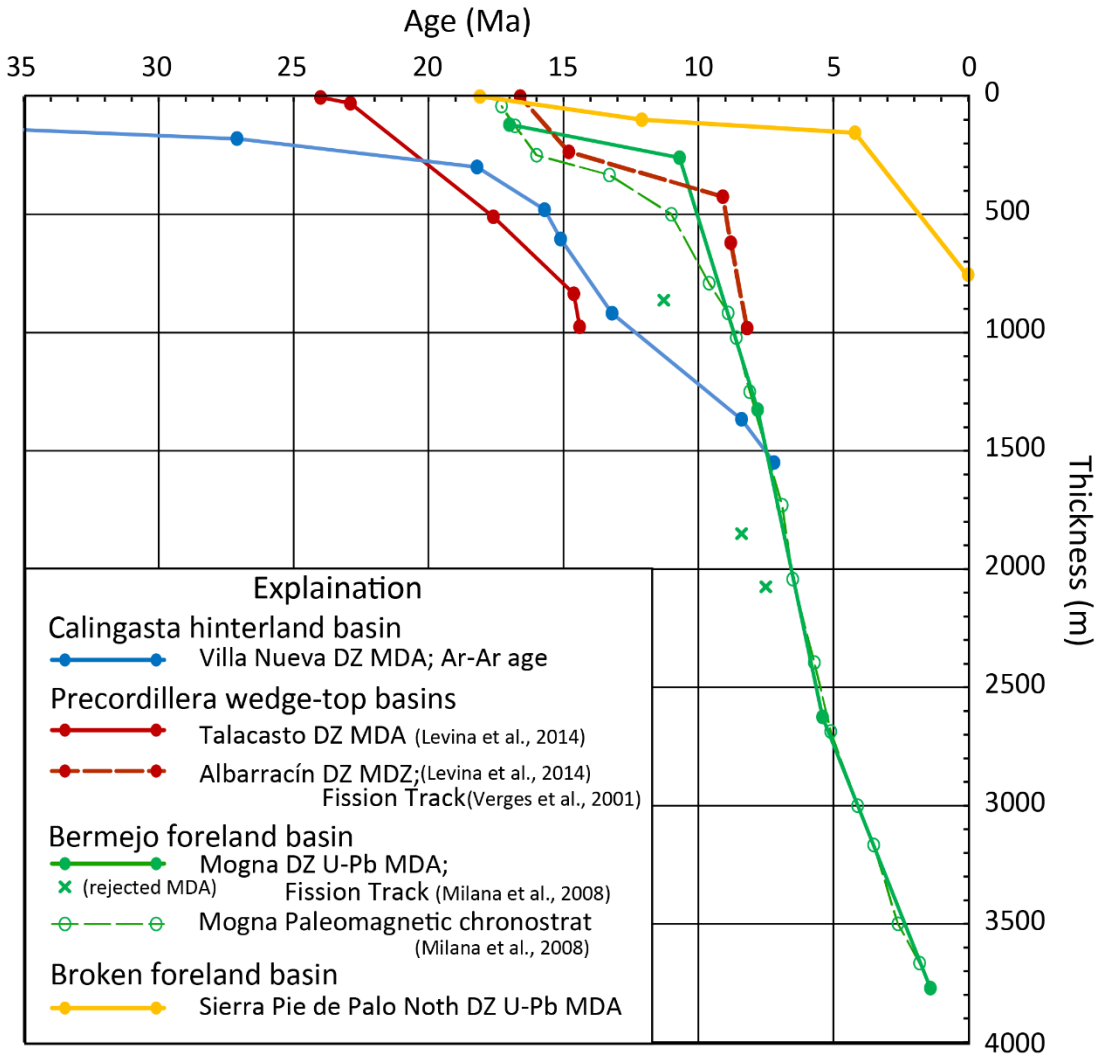

Figure 2.10: Cenozoic sediment accumulation history for Calingasta hinterland (blue), Precordillera wedge-top (red), Bermejo foreland (green), and broken foreland (yellow) sections.

Foreland Clastic Wedges

New Neogene lithostratigraphic and chronostratigraphic correlations across the retroarc of Argentina exhibit upward coarsening stratigraphic phases across five distinct stratigraphic periods: (1) Oligocene to lower Miocene (24-17 Ma) mixed fluvial-eolian system, (2) Middle Miocene (17-11 Ma) regional fluvial sequence, (3) Upper-Miocene (11-5 Ma) fluvial mega-fan distributive system, and (4) Pliocene to Present (5-0 Ma) broken foreland basin. The shift from low to high energy deposition (fine to coarse grained facies) reoccurs within stratigraphic intervals that span 3-7 Myr, and is superimposed upon a prolonged Oligocene to present eastward progradation of alluvial facies. Investigating the relationships among stratigraphic trends (Figs. 3, and 4), lithofacies (Fig. 5), and sediment provenance (Figs. 7, 8 and 9), and accumulation histories (Fig. 10) across the retroarc region of Argentina, establishes a stratigraphic framework to understand the feedbacks and relationships among subduction, magmatism, Cenozoic orogenesis, and sediment transport (Fig. 11).

The Paleogene sequence in the Calingasta basin does not exhibit upward coarsening stratigraphic signatures like those in the younger Oligocene to Miocene units (Fig. 7). The volcaniclastic deposits of the Calingasta basin contain Paleogene arc and Carboniferous arc zircon age signatures indicative of Principal Cordilleran sediment sources found in present Chile. These deposits can be potentially correlated to Paleogene deposits found in the northern Bermejo basin that exhibit low-energy lacustrine and fluvial depositional environments (Puesto de Flecha Formation) and are interpreted to be deposited in an incipient distal foreland basin setting (Reat and Fosdick, 2018). The overlying middle

Oligocene fine-grained overbank paleosols and floodplain deposits and interbedded andesitic-basalt volcanics can be interpreted as a stratigraphic expression of hinterland extension (Fig. 12; Mackaman-Lofland et al., 2019).

Oligocene-lower Miocene (24 - 17 Ma) fluvial-eolian system

The first upward coarsening phase is recorded in Oligocene-Miocene basal eolian deposition in the Precordillera Talacasto section that is capped by a regionally extensive lower-Miocene fluvial deposits (Fig. 11A). The basal eolian unit T2 spans 24-18 Ma and can be correlated regionally with Vallacito Formation eolian stratigraphy that spans the north Bermejo foreland (Jordan et al., 1993; 1996; Limarino et al., 2000; Ciccioli et al., 2014; Levina et al., 2014; Fosdick et al., 2017). Calingasta Oligocene-lower Miocene fluvial stratigraphy (Unit C2) has east paleocurrents and Andean sediment provenance, whereas distal Bermejo foreland deposits are coarse grained fluvial sequences from eastern cratonic sources (Figs. 7, 8, 9). Calingasta and Bermejo basins flank the eolian deposits (Unit T2) that exhibit N-NW Paleocurrents, which suggest the eolian system developed orogen-parallel and axially transported sediment derived from both the Andes and craton as the incipient foreland basin developed (Figs. 12). The lateral facies change from a proximal east flowing braided fluvial system (Unit C2) to distal eolian deposits reworking fluvial deposits along with a predominate south to north wind direction (Unit T2) is analogous to the Holocene Bermejo foreland sediment routing system (Hirtz et al., 2019). Regionally extensive fluvial deposits (~17 Ma) overly both Precordilleran eolian and Bermejo basin conglomeratic facies, with diagnostic Andean (Principal and Frontal

Cordillera) sediment sources. This capping fluvial sequence records the terminal phase of the Oligocene-Lower Miocene clastic wedge as increased shortening within the Cordilleran hinterland inducing potentially high sediment flux far into the foreland basin (Fig. 12). The upward coarsening sequence observed in the Oligocene-lower Miocene deposits indicate a migrating flexural basin system from proximal foreland fluvial system in Calingasta, distal eolian foreland deposits in Precordillera, and thin basal alluvial deposits indicative of a potential forebulge migration eastward (Fig. 7). The distal conglomerate facies of the lower Rio Salado Formation suggest exposed sediment sources in the distal foreland, at the time of initiation of Bermejo deposition, suggesting erosion from an eastern migrating forebulge between Bermejo and the Sierras Pampeanas (Fig. 7).

Middle Miocene (17 - 11 Ma) regional fluvial sequence

By the middle-Miocene (~17 Ma) a regionally continuous foreland basin and associated fluvial systems comprising of braided river deposits extended >300 km across the Calingasta basin propagating into the Precordillera sections by 15 Ma and into the distal foreland around 11 Ma (Fig. 12A). Basal Bermejo basin stratigraphy consisted of fine-grained silts and sands with interbedded pedogenic horizons suggest floodplain and intermittent playa lake depositional system indicative of a distal foredeep depocenter or a forebulge. From 17-11 Ma the retroarc foreland basin of Argentina records a prograding fluvial facies assemblage by 11 Ma there is the appearance of conglomerates in the Calingasta basin, sand to pebble conglomerate in the Precordillera, and sand in the Bermejo foreland sections (Fig. 12). The propagation of the Middle Miocene clastic wedge and

Frontal Cordillera unroofing trends recorded by DZ provenance suggest deformation advanced toward the foreland as subduction angle begins to flatten. The upsection transition from sandy channels into well-rounded cobble to granule conglomerate beds with trough and planar-cross beds is the culmination of the Middle Miocene upward coarsening cycle. Additionally, the initial appearance of channels suggests a high energy and ephemeral braided fluvial system propagating into the Bermejo basin. These coarsening up-section trend is observed in each stratigraphic section during this time phase, indicative of a prograding braided river-dominated, clastic wedge from the hinterland extending > 300 km toward the foreland (Fig. 7).

Upper-Miocene (11-5 Ma) foreland fluvial-mega fan and internally drained hinterland

Upper Miocene stratigraphy records two upward coarsening sequences spanning the (11-8 Ma) and (8-5 Ma) during punctuated shortening within the Precordillera and Frontal Cordillera (Fig. 12; Jordan et al., 1993; Cristallini and Ramos, 2001; Allmendinger and Judge, 2014). Sediment accumulation migrates to the foredeep as fluvial-mega fan systems initiated in the Bermejo foreland. Deposition is focused in a foredeep proximal to the deforming Precordillera fold-thrust belt, accumulating 2000 m thick deposits that thin rapidly eastward toward the Sierras Pampeanas. In the Pie de Palo section only 10's of meters are deposited during 11-5 Ma, which reflects a either the lack of strata during this period or a highly condensed stratagraphic section within upper Unit SP1 (Figs. 4B and 10). Lack of sediment accommodation within the distal foreland potentially suggest a

change in the sediment routing system where a distal axial system migrates closer to the orogenic front.

Precordillera uplift structurally partitions the Calingasta and Precordillera sections into wedge-top depocenters with low accommodation basins dominated by cobble to gravel braided fluvial and alluvial fan systems that are sourced by proximal high relief drainage catchments, and lower accommodation rates. (Fig. 12). By 8 Ma abrupt facies change to fine-grained silts and marls in the Calingasta basin suggests a dramatic change in the sediment routing system that alternates between an internally drained system and sediment bypass to the fluvial mega-fan system of Bermejo Basin (Val et al., 2016). Intermittent basin isolation and volcaniclastic facies indicate that Calingasta depocenter transitioned into an isolated hinterland basin by 8 Ma. The appearance of hinterland lacustrine carbonates and lack of deposition within the Sierras Pampeanas and Precordillera, suggest extensive structural partitioning of the basin system into isolated depo-centers and a spatially narrow region of foreland deposition within the Bermejo foreland.

Pliocene to Present (5-0 Ma) isolated basin systems

Broken foreland conditions are established during Pliocene to present (5-0 Ma), as the once continuous basin system is structurally partitioned into the Precordillera fold-thrust belt and Sierras Pampeanas basement involved uplifts. Continued foreland deformation cannibalizes Neogene foreland deposits as the proximal Bermejo Foreland shift towards a wedge-top basin setting, and the distal Sierras Pampeanas records proximal

alluvial fan deposition as Sierra Pie de Palo accommodates far field strain in the Pliocene to present (Fig. 12).

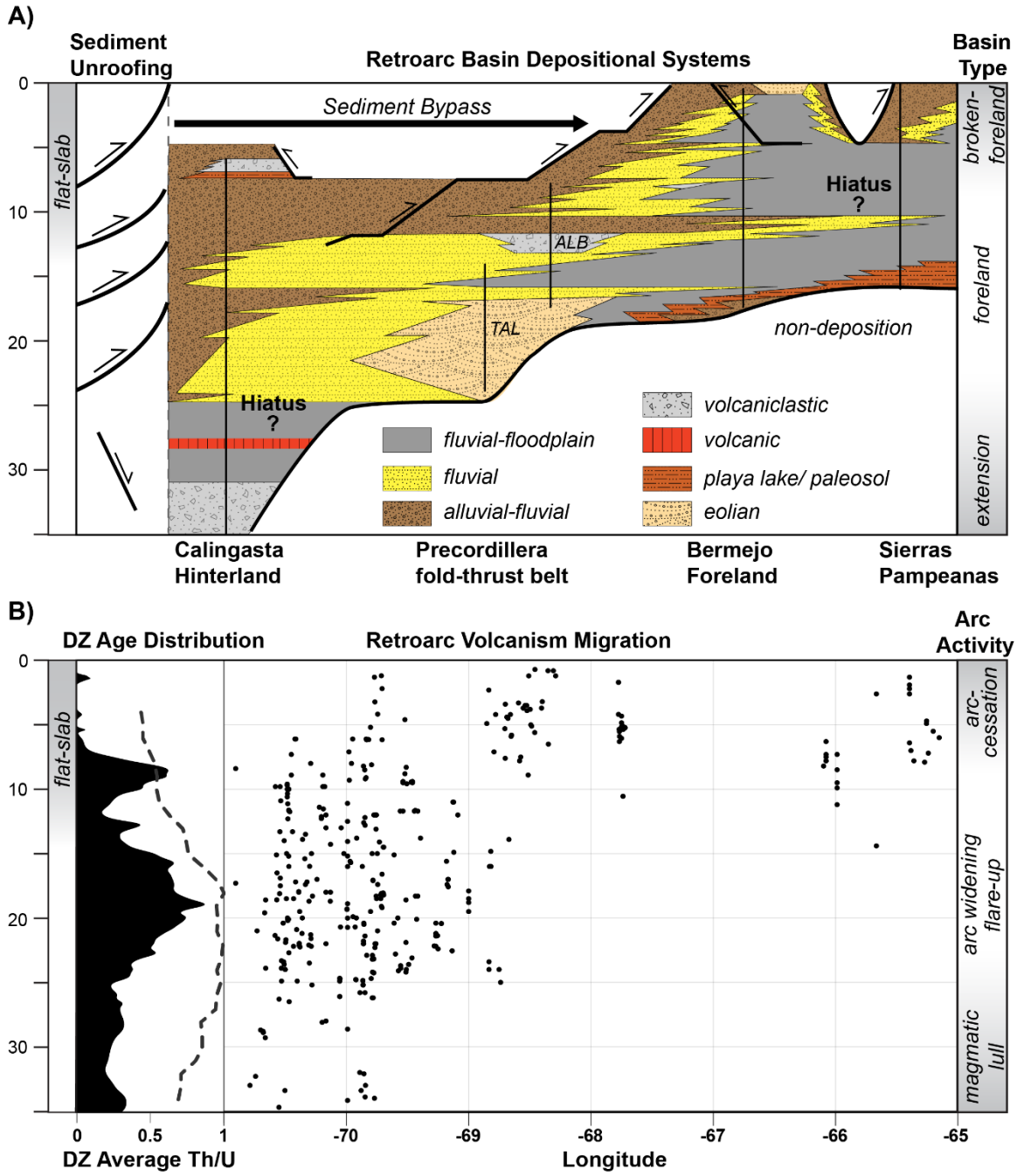

Figure 2.11: (A) Spatial and temporal facies and sediment unroofing correlation plot across the Argentina retroarc basin system. Vertical black lines represent measured section location. Precordillera fold-thrust belt progression interpretations from (Allmendinger and Judge, 2014). (B) Cenozoic magmatic history recorded by detrital zircon (DZ) isotopic systems (U-Th-Pb-Lu-Hf). Arc tempo records pulses and lulls in DZ U-Pb geochronology. Magmatism composition derived from evolved sources (< 0.5 Th/U) or juvenile sources (> 0.5 Th/U). Arc migration patterns tracked by bedrock radiometric dates.

Andean arc magmatism

Combined zircon U-Th-Pb and volcanic arc spatial patterns provides a first-order constraint on the geodynamic boundary conditions for the Andean cordilleran system as Neogene Pampean flat-slab subduction initiates. Cenozoic Andean arc tempo can be interpreted from the relative probability of detrital zircon age distribution where magmatic high-flux events (HFEs) and lulls are represented by zircon age peaks and troughs respectively (Fig. 11B). Evaluating the operative spatial and temporal scales of arc magmatism provides a means to test proposals of HFEs and magmatic lulls that may generate cyclical or punctuated recurrence intervals associated with shortening (DeCelles et al., 2009; 2015). Comparing the operative timescales of magmatism activity and changes in crustal composition, with observed cyclical upward-coarsening cycles in the retroarc basin stratigraphy provides new constraints on Cordilleran tectonic feedbacks.

We constrain latest Eocene to present (35-0 Ma) magmatic history to contextualize the Cordilleran system before Andean flat-slab subduction, in terms of Zircon U-Pb age distribution HFEs and U/Th values (Fig. 11B). Late Paleogene (35 to 24 Ma) magmatism is display a lull between 33 to 29 Ma and subtle increased flux 28 to 25 Ma. Magmatism is restricted to a narrower (< 100 km) arc width located in the modern Chilean Principal cordillera. The DZ record a Th/U ratio increase from 0.7 to 1 that suggest extensional upper-plate conditions synchronous with the hinterland depositional hiatus and basaltic magmatism recorded in the basal Calingasta basin deposits in unit C1 (Mackaman-Lofland et al., 2019).

New stratigraphic and magmatic constraints show that Oligocene to Miocene shallowing of subduction angle drives the widening of the magmatic arc (~200 km), which is coeval with upper-plate magmatic HFE, deformation patterns, and basin evolution. Neogene magmatic HFE occur over a 12 Myr long phase during the late-Oligocene to Miocene (24-11 Ma) with a symmetric age-probability shape with subordinate peaks over the sub-3 Myr intervals (Fig. 11B). Notably, this HFE temporally overlap with upward coarsening stratigraphic trends in the retroarc basin of Argentina (Fig. 11A). From 24 to 17 Ma zircon Th/U ratios are relatively stable (0.95 to 1) during the waxing phase of the HFE. By 17 Ma the HFE peaks and begins to wane and is synchronous with DZ Th/U decrease from to 1 to 0.55 by 11 Ma. The decrease in Th/U values indicates greater involvement of crustal components being reworking into the magmatic system throughout the Oligocene to Miocene (24-12 Ma) magmtic phase (Fig. 11 B).

An upper Miocene HFE (11-7 Ma) is the last significant continental arc magmatic activity in the region before arc-cessation (< 5 Ma). The upper-Miocene HFE is synchronous with a significant eastward migration of volcanism (>450 km) into the modern Sierras Pampeanas. The drastic shift in igneous activity reflects the shallowing of the Nazca plate to < 5° by 11 Ma. The upper-Miocene DZ Th/U ratios remain relatively low < 0.55 during this phase of magmatism (Fig. 11B). The decrease in Th/U, and pulsed HFE during the upper-Miocene reflects increased crustal contributions during magmatism as the subduction angle approaches sub-horizontal geometries.

New stratigraphic correlations document propagation of a clastic wedge into the foreland coeval with HFE events and isotopic decrease, suggesting that cyclical tectonic

signatures are also recorded within the retroarc basins of Argentina (Figs. 12 and 13). Variation in zircon isotopes are temporally linked with zircon age peaks throughout the Neogene, displaying frequencies of 3-7 Myr, and may represent cyclical phases of crustal underthrusting into the Miocene magmatic arc (DeCelles et al., 2009; 2015). Here we speculate that a temporal relationship between lower-plate changes, magmatism, and Earth surface response exists. Though speculative, such observed feedbacks and relationships among lower-plate mechanisms and upper-plate responses may have broader significance to refining Cordilleran cyclicity and orogenic wedge models (Anderson et al., 2018).

Cordilleran Evolution during Andean Flat-Slab Subduction

Subduction zones are fundamental components in Earth systems and understanding how deformation is propagated from the down-going oceanic plate into the over-riding plate has far reaching implications for understanding the geodynamics of Cordilleran systems. This study shows that a decrease in subduction angle from 30° to <5° is associated with Miocene arc magmatism, deformation, and deposition that propagates >700 km away from the Chile trench (Fig. 12). Oligocene (32-24 Ma) strata records a magmatic lull and arc proximal basaltic volcanism related to extensional stress-regimes. The Oligocene-Miocene (24-17 Ma) change in subduction angle from 25-10° is reflected in the broadening of arc volcanism and initiation of deposition in the retroarc Calingasta-Bermejo basin network (Fig. 12A). The step-wise jump was subduction angle is synchronous with a rotation of Nazca plate velocity perpendicular to the Andean margin (Yanez, 2001). The rotation of the Nazca Plate additionally changes the trajectory of the predicted Oligocene

Juan Fernandez Ridge hot-spot island chain to an orientation more oblique to the trench, thereby increasing the surface area of the oceanic asperity entering the trench along the South American margin. Oligocene-Lower Miocene deposits were sourced from the Principal Cordillera fold-thrust belt and transported by southern paleo-winds axially through a regional-scale eolian field (Tripaldi and Limarino, 2005). By 17 Ma crustal thickening and lithospheric loading produced flexural accommodation that advances into the foreland (Fig. 12B). The continuity of lithofacies and sediment provenance suggest a spatially continuous foreland basin system. During 17-11 Ma, a transverse fluvial system draining the Principal Cordillera and Frontal Cordillera displayed a spatial trend of sediment finning towards the foreland and changes from a W-E traversing braided river network to a distal N-S axially flowing meander belt and floodplain environment. The foreland basin system connectivity was abruptly perturbed as volcanism broadens and deformation advances into the foreland. The width of the 11-2 Ma volcanic arc records subduction angle decrease to ~5° and is synchronous with significant changes within upper-plate deformation and basin configuration. A coarse-grained clastic wedge propagated throughout the foreland as shortening within the Precordillera exhumed and cannibalized the Oligocene-Lower Miocene foreland basin sediments (Fig. 12 C). Both Calingasta and Precordilleran stratigraphic records changes to an alluvial depositional environment, a decrease in sediment accumulation, and are fed by proximal sediment sources, suggesting a transition into wedge-top depo-centers between 11 to 8 Ma (Beer et al., 1999; Verges et al., 2001; Levina et al., 2014). Shallowing of the subduction angle to 5° produces a flat-slab geodynamic setting as the Juan Fernandez ridge enters the trench

E-NE spatially stabilizing the buoyant asperity below these latitudes. Upper-plate response to prolonged Upper-Miocene to present flat-slab subduction is manifested by distal basement involved deformation that structurally partitioned the regional flexural foreland into isolated, uplift-proximal basins. The retroarc region of Argentina at this time transitioned into a broken foreland setting where the basin systems were discontinuous and distal sediment routing systems are controlled by structural location and proximal sediment sources (Fig. 12D). By the Quaternary broken foreland deposition was dominated by fluvial-mega fans exiting the Precordillera fold-thrust belt and transitioning into broad eolian systems in the east.

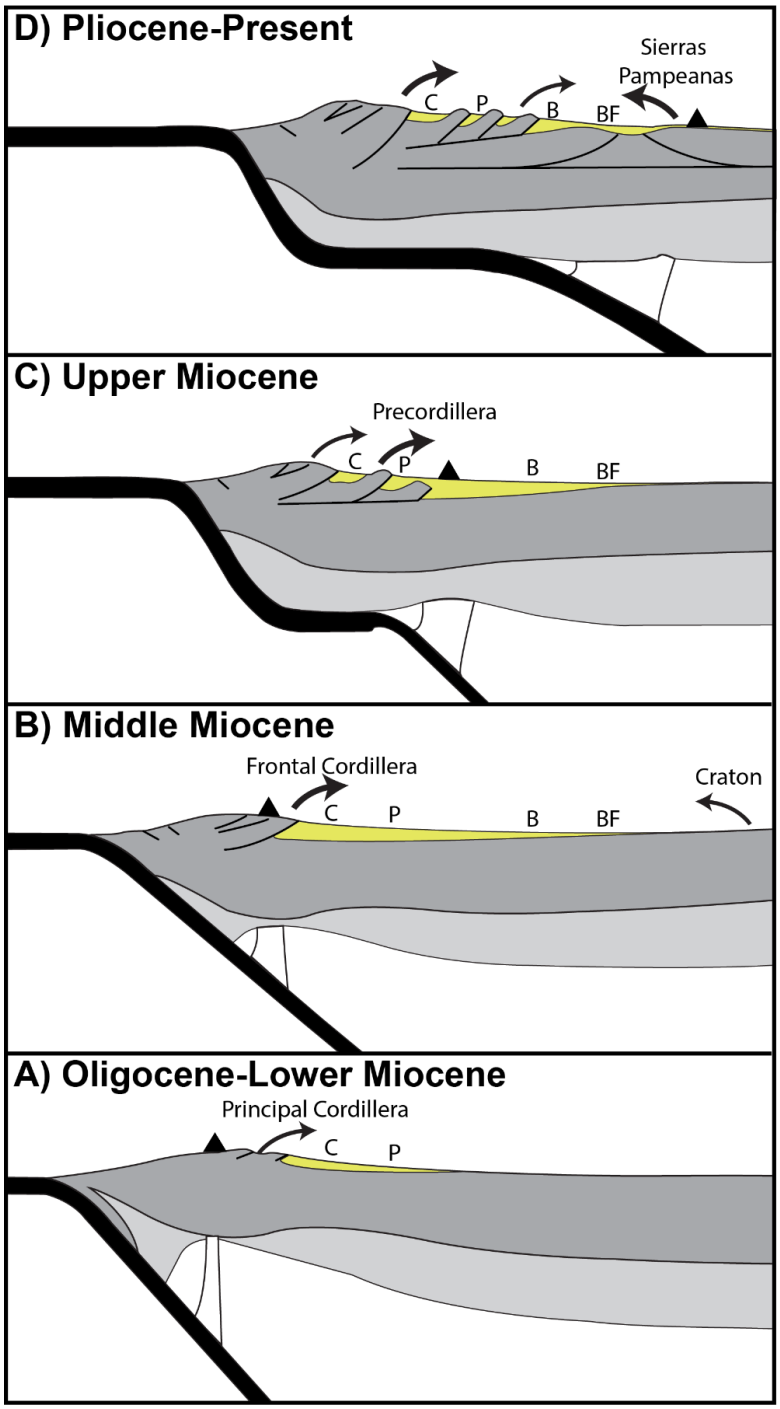

Figure 2.12: Cenozoic tectonic model for Argentina retroarc basin evolution. Black arrow indicate sediment provenance sources. Yellow polygon reflects basin deposition. Black triangle is location of arc magmatism front.

CONCLUSIONS

(1) New measured stratigraphic sections in the Calingasta hinterland basin and Sierras Pampeanas broken foreland are integrated with published stratigraphy to establish new lithofacies and chronostratigraphic correlation across the Andes of Argentina at 32.5°S. The retroarc basin system records numerous clastic wedges that propagate toward the foreland that include: Oligocene to lower Miocene (24-17 Ma) mixed fluvial-eolian system; Middle Miocene (17-11 Ma) regional fluvial sequence; Upper Miocene (11-5 Ma) fluvial mega-fan distributive system and internally drained hinterland basin, and (6) Pliocene to Present (5-0 Ma) broken foreland basin system.

(2) New detrital zircon analyses from a suite of Cenozoic sandstones when compared with published modern river sands constrain the erosional unroofing history of the Coastal Cordillera and Principal Cordillera of Chile and Frontal Cordillera, Precordillera, and Sierras Pampeanas of Argentina (32.5°S). Provenance trends record Oligocene to lower Miocene erosion from Principal Cordillera, followed by dominant sediment input from the Frontal Cordillera by the Middle Miocene. Middle to Upper Miocene foreland deposits record mixed provenance signatures from both the Frontal Cordillera and Precordillera fold-thrust belt as flat-slab subduction became fixed below the South American plate at 32.5°S. Provenance signatures reflect proximal basement involved uplifts as the retroarc transitions into a broken foreland setting in the Pliocene.

(3) Miocene magmatism displays high flux events that occur over 3-7 Myr long phases coeval with upward coarsening stratigraphic signatures and detrital zircon provenance trends. Radiometric isotope systems from detrital zircon indicates greater

involvement of crustal components being reworking into the magmatic system as subduction angle decreases.

(4) Patterns of Andean erosion and sedimentation recorded the initiation of shallow to flat-slab subduction and increased plate coupling, as expressed in the intensification and eastward advance of magmatism, shortening, and foreland basin subsidence.

CHAPTER 3: SEDIMENT PROVENANCE IN CONTRACTIONAL OROGENS: THE DETRITAL ZIRCON RECORD FROM MODERN RIVERS IN THE ANDEAN FOLD-THRUST BELT AND FORELAND BASIN SYSTEM OF WESTERN ARGENTINA[1]

ABSTRACT

This study analyzes detrital zircon U-Pb age populations from Andean rivers to assess whether active synorogenic sedimentation accurately records proportional contributions from varied bedrock source units across different drainage areas. Samples of modern river sand were collected from west-central Argentina (28-33°S), where the Andes are characterized by active uplift and deposition in diverse contractional provinces, including (1) hinterland, (2) wedge-top, (3) proximal foreland, and (4) distal broken foreland basin settings. Potential controls on sediment provenance are evaluated by comparing river U-Pb age distributions with predicted age spectra generated by a sediment mixing model weighted by relative catchment exposure (outcrop) areas for different source units. Several statistical measures (similarity, likeness, and cross-correlation) are employed to compare how well the area-weighted model predicts modern river age populations. (1) Hinterland basin provenance is influenced by local relief generated along thrust-bounded ranges and high zircon fertility of exposed crystalline basement. (2) Wedge-top (piggyback) basin provenance is controlled by variable lithologic durability among thrust-belt bedrock sources and recycled basin sediments. (3) Proximal foreland (foredeep) basin provenance

[1] Capaldi, T.N., Horton, B.K., McKenzie, N.R., Stockli, D.F., Odlum, M.L., 2017, Sediment provenance in contractional orogens: The detrital zircon record from modern rivers in the Andean fold-thrust belt and foreland basin of western Argentina: Earth and Planetary Sciences Letters, v. 479, p. 83-97, doi: 10.1016/j.epsl.2017.09.001. I completed field work, sample preparation, geochron analysis, statistical modeling, project idea, and writing.

of rivers and fluvial megafans accurately reflect regional bedrock distributions, with limited effects of zircon fertility and lithologic durability in large (>20,000 km^2) second-order drainage systems. (4) In distal broken segments of the foreland basin, regional provenance signatures from thrust-belt and hinterland areas are diluted by local contributions from foreland basement-cored uplifts.

INTRODUCTION

Provenance studies incorporating the composition and geochronology of clastic sediments are fundamental to reconstructions of tectonic, paleogeographic, and paleodrainage histories. In modern depositional systems, petrographic analyses were critical in first identifying important controls on sediment composition, including source-rock distribution, drainage organization, climate, structural geometry, and basin configuration (Dickinson and Suczek, 1979; DeCelles and Hertel, 1989; Ingersoll, 1990; Johnsson et al., 1993; Garzanti et al., 2007). More recently, detrital zircon (DZ) U-Pb geochronology has become increasingly utilized as a proxy for contributions from zircon-bearing sources in continental crustal rocks, with U-Pb age distributions providing constraints on provenance and depositional age (e.g., Dickinson and Gehrels, 2008; Gehrels 2014; McKenzie et al., 2013, 2016; Horton et al., 2015a). Nevertheless, interpretations of DZ provenance for ancient systems are far from routine, as they involve numerous unknowns and assumptions regarding source-to-sink processes, which commonly relate to issues of source characterization, structural context, drainage network

morphology, zircon fertility, lithologic durability, erosional variability, the effects of proximal-distal mixing and downstream dilution, and the configuration of subsiding basins.

Because the distribution of sediment sources and drainage networks are explicitly known in active orogenic systems, studies of modern rivers provide unparalleled opportunities to identify source signals and isolate DZ provenance responses to several variables. Key issues include the impact of heterogeneous input (as controlled by variable erosion patterns and zircon fertility distributions) and downstream fluvial mixing patterns (as governed by drainage organization and basin configuration). Detrital mineral ages from modern rivers have allowed researchers to gauge contributions from particular segments of mountainous drainage catchments in contractional orogens (e.g., Amidon et al., 2005a, 2005b; Cina et al., 2009; Zhang et al., 2012, 2016; Saylor et al., 2013; Horton et al., 2015b; Pepper et al., 2016). In addition to exposure (outcrop) area, zircon age distributions are influenced by: (1) variations in *zircon fertility*, defined as zircon mineral fraction weight % or whole-rock Zr concentrations for a given source area (Moecher and Samson, 2006; Dickinson, 2008; Malusà et al., 2016); (2) differences in lithologic *erodibility* (or durability) (Amidon et al., 2005a; Garzanti et al., 2007); and (3) locally focused erosion and climatic effects (Zhang et al., 2012; 2016; Romans et al., 2016). These factors have the potential to generate disproportionate sediment and zircon yields relative to exposure area, and may alter zircon age signals and downstream trends. Further, given the limited preservation potential of erosional drainages, understanding of the role of basin structural configuration on modern provenance requires evaluation of actively subsiding (net accumulation) systems.

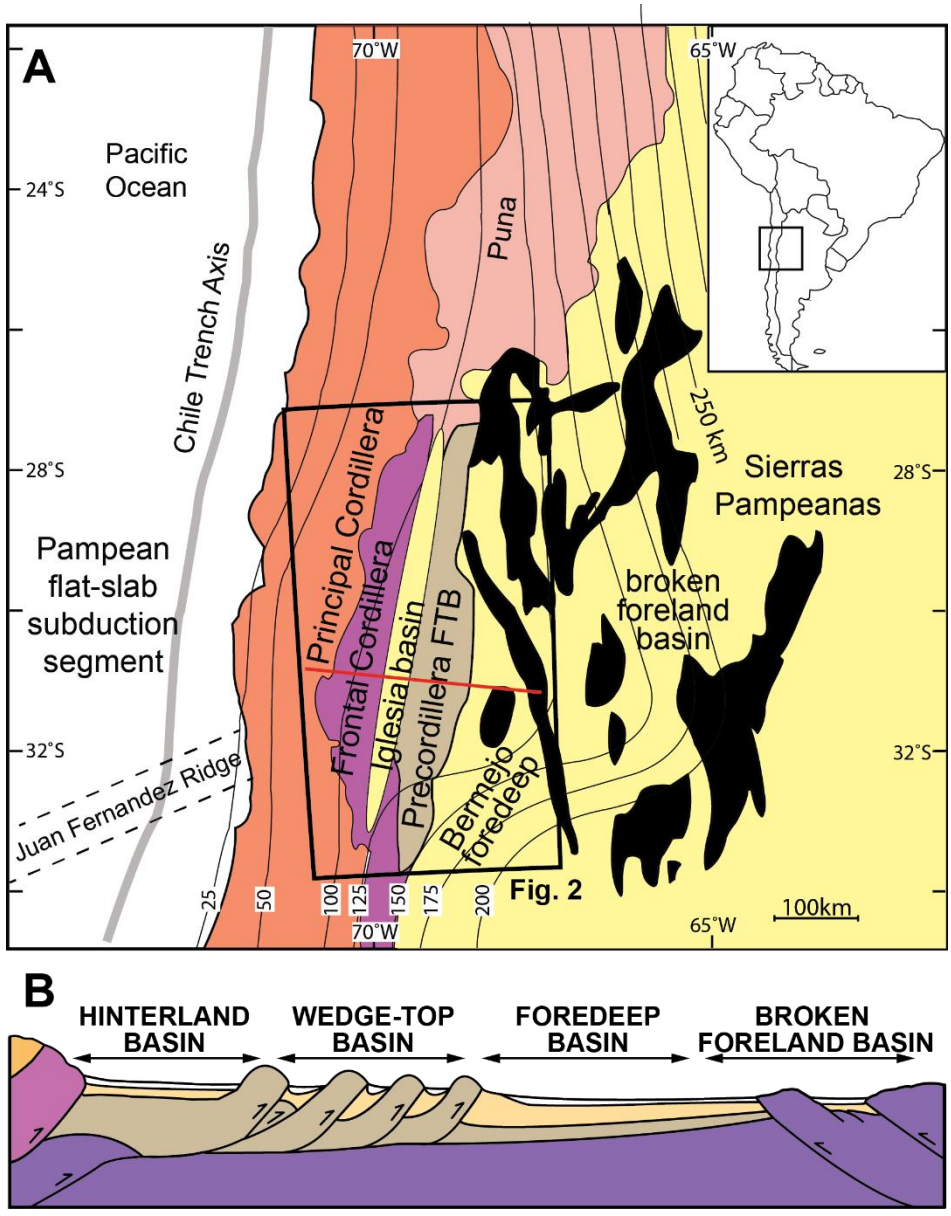

Figure 3. 1: (A) Tectonic map of the southern Central Andes displaying major geologic provinces in the Pampean flat-slab segment of western Argentina, with depth contours (in kilometers) to the subducted Nazca plate (after Ramos et al., 2002). (B) Simplified east-west cross section showing various tectonic settings for contractional basin systems in a retroarc foreland setting.

This study applies DZ U-Pb geochronology to river sediments in several contractional basins and their respective drainage networks and fluvial systems. Retroarc hinterland and foreland basin systems are defined by distinct structural styles and associated sediment routing systems (Dickinson et al., 1988; Jordan, 1995; Horton and DeCelles, 2001; Horton, 2012). These basins are the product of flexural subsidence driven by shortening and crustal thickening, in which fold-thrust structures control relief generation and associated erosion, drainage network evolution, and the distribution of fluvial megafans. This study assesses the fidelity of DZ age signatures in an active source-to-sink system with variable fertility, erodibility, and sediment recycling patterns over a range of spatial scales across different basin tectonic settings (Fig. 1). The impact of basin configuration on DZ provenance is assessed by generating forward models (Saylor et al., 2013; Saylor and Sundell, 2016) that predict age distributions with contributions proportional to exposed bedrock area in respective catchments, which are then compared to river DZ age distributions.

The Andes exemplify retroarc fold-thrust belt and foreland basin processes, with active uplift and deposition in diverse contractional provinces, including hinterland, wedge-top, foreland, and broken foreland basin settings. The study region in west-central Argentina (Fig. 2) exposes bedrock sources with variable lithologies and zircon age spectra that can be readily distinguished (Fig. 3). River sand samples from various provenance groups—including smaller (first-order) tributary rivers draining individual to locally mixed rock types, and larger (second-order) main stem rivers draining mountain ranges (e.g., Ingersoll, 1990)—provide insights into scaling factors that influence DZ provenance. Due

to the uniform semi-arid environment, significant effects from climatic variability are unlikely. Hence, this segment of the Andes and its adjacent foreland provide an important opportunity to assess the influence of contractional basin configuration on sediment provenance.

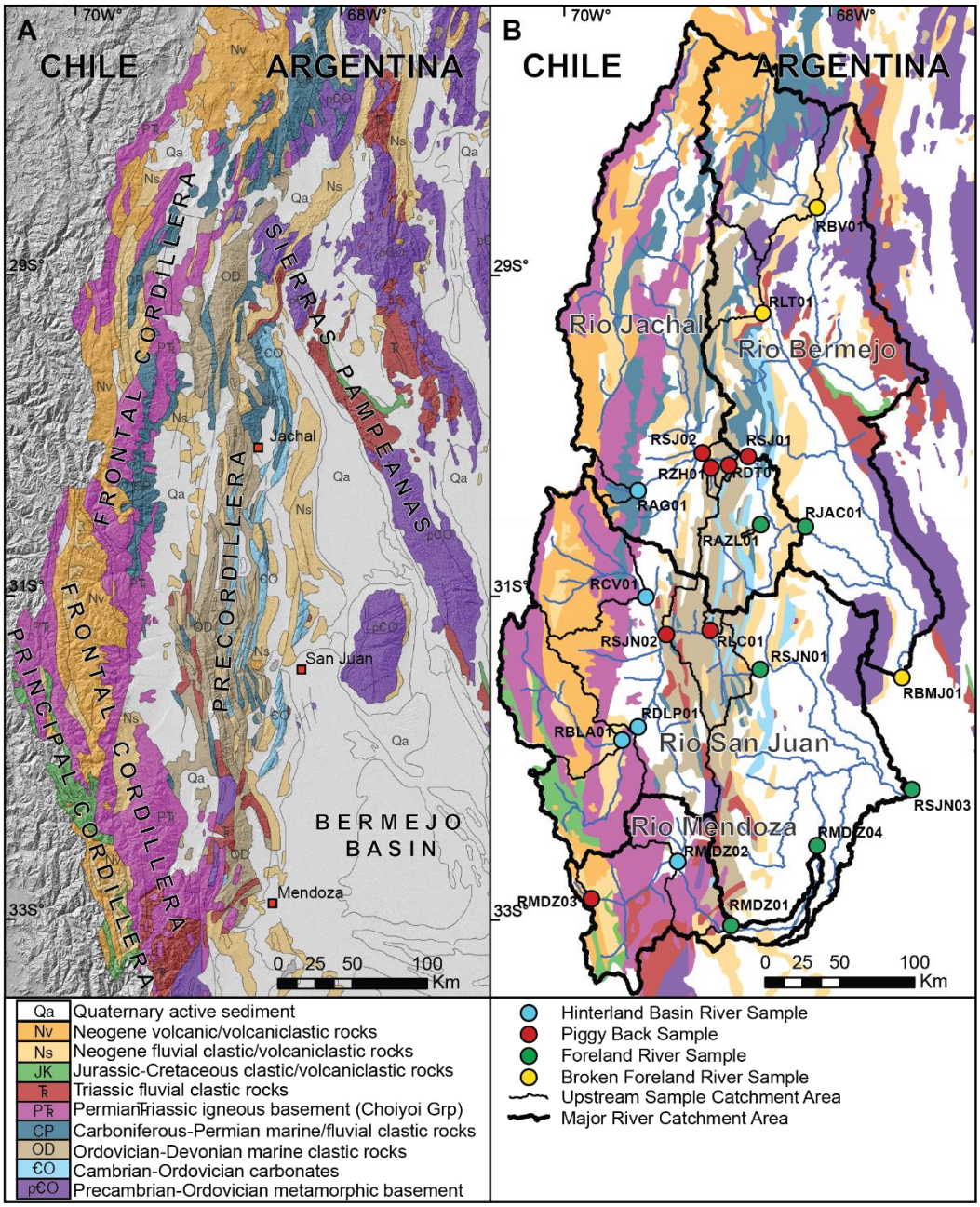

Figure 3.2: Regional maps of west-central Argentina. (A) tectonic provinces and geologic units of the Andean retroarc thrust belt (Principal Cordillera, Frontal Cordillera, and Precordillera), foreland basement uplifts (Sierras Pampeanas), and foreland basin deposits (unit Ns). (B) Drainage catchments for major rivers (Rio Bermejo, Rio Jachal, Rio San Juan, and Rio Mendoza thick black outlines), subordinate drainage networks (thin black outlines), and modern river samples (circles) color coded by tectonic setting: hinterland basins (blue); wedge-top basins (red); foreland basins (green); and broken foreland basins (yellow).

RETROARC CONTRACTIONAL BASIN SYSTEMS

The Andes of west-central Argentina (28-33°S) (Figs. 1A and 2A) are divided into distinct provinces. These include, from west to east: (1) a magmatic arc (Principal Cordillera), thick-skinned block uplift (Frontal Cordillera), and adjacent hinterland basin (Iglesia-Calingasta basin); (2) a ramp-flat fold-thrust belt (Precordillera) with isolated wedge-top (piggyback) basins; (3) a proximal foreland basin (Bermejo basin) with large fluvial and alluvial-fan systems and thick foredeep depocenters; and (4) a distal foreland partitioned by basement-cored block uplifts (Sierras Pampeanas).

In the west, the Principal Cordillera along the Chile-Argentina border consists of magmatic arc rocks (unit Nv) and deformed Mesozoic rift-related strata (unit JK) (Fig. 2A; Cristallini and Ramos, 2000). The retroarc hinterland includes the Frontal Cordillera block, composed of a >3 km thick assemblage of late Paleozoic-Triassic granodiorite, andesitic/rhyolitic lavas, and pyroclastic rocks of the Choiyoi Group (unit P^; Heredia et al., 2002), which is capped by Neogene volcanic and volcaniclastic materials derived from the Andean arc (unit Nv). Deeper structural levels in the northern Frontal Cordillera include Carboniferous-Permian marine strata and associated intrusions (unit CP; Fig. 2A) (Heredia et al., 2002). High-relief drainage networks of the Principal and Frontal Cordilleras deliver sediments to the high elevation (~2000m) Iglesia-Calingasta-Uspallata hinterland basin system. This <3.5 km intermontane depocenter is composed of Neogene alluvial-fan, fluvial, and lacustrine facies (Beer et al., 1990; Fig. 2B).

The Precordillera is an east-directed fold-thrust belt involving a Paleozoic marine clastic and carbonate succession (units CP, OP, _O) (von Gosen, 1992; Ramos, 1999). The

Cambrian-Ordovician carbonate platform succession (unit _O) is overlain by Upper Ordovician-Devonian clastic facies in eastern and central thrust sheets, with slope to deep-marine facies in western thrust sheets (unit OD). Over 100 km of E-W shortening was accommodated by imbricate thrust sheets above a ~12 km deep decollement (von Gosen, 1992; Cristallini and Ramos, 2000; Allmendinger and Judge, 2014; Fosdick et al., 2015). Neogene foreland basin deposits (unit Ns) are preserved in the footwalls of major thrust faults, with preferential erosion forming intermontane valleys between thrust-generated ranges (Jordan et al., 2001; Levina et al., 2014). Modern wedge-top basins are filled by coalescing alluvial fans along narrow intermontane valleys in which axial N-trending tributaries transport sediment downslope to E-flowing transverse rivers (Fig. 2B).

Along the eastern flank of the Precordillera, the Bermejo foreland basin accumulated up to 7 km of Neogene synorogenic fluvial and alluvial-fan sediments (unit Ns; Jordan et al., 2001). Active sedimentation is dominated by fluvial megafans fed by large catchment areas (>10,000 km^2) with focused entry points into the proximal foreland basin. Distal eastern parts of the basin are structurally partitioned by roughly NNW-trending basement-cored arches (Sierras Pampeanas) and intervening subsiding zones within a broken foreland basin province (Fig. 1). This zone is composed of metamorphic and igneous rocks (unit =O) of late Proterozoic-early Paleozoic terranes (Ramos, 1999, 2009; Ramos et al., 2002; Mulcahy et al., 2014), local Mesozoic nonmarine strata (units ^ and JK) (Ortiz et al., 2015; Fig. 2), and Neogene basin fill (unit Ns) capped by coalescing alluvial fans along basin-bounding structures (Diamante, 1993).

U-Pb GEOCHRONOLOGY

Methods

We collected and analyzed 23 sedimentary, igneous, and metamorphic samples for bedrock source characterization and 21 unconsolidated sands from major rivers and tributaries within the La Rioja, San Juan, and Mendoza provinces (Fig. 2B). Standard mineral separation techniques included crushing and grinding for consolidated bedrock samples, and water table, heavy-liquid density, and magnetic susceptibility separations for all samples. Nonmagnetic heavy mineral separates were poured onto double sided tape (~2.54 cm) on epoxy resin mounts, then zircon grains were chosen randomly for analysis by laser ablation–inductively coupled plasma–mass spectrometry (LA-ICP-MS) to obtain U-Pb ages. At least 120 zircon grains were analyzed per sample to resolve significant age components. Sample mounts were loaded into a large-volume Helex sample cell and analyzed with a magnetic sector, single collector Element2 ICP-MS with a PhotonMachine Analyte G.2 excimer laser, as outlined by Horton et al. (2016).

U-Pb age distributions (Table S1; see Supplementary Material) are described in terms of specific age components or modes for samples or stratigraphic intervals that reflect a particular provenance signal. Diagnostic age components include, from oldest to youngest (Fig. 3): (1) 1450-1350 Ma Laurentian-derived ages from the Cuyania terrane (Ramos, 2009); (2) 1200-1000 Ma Cuyania basement and Sunsás magmatic rocks (Bahlburg et al., 2009); (3) 725-550 Ma Neoproterozoic rocks of eastern Sierras Pampeanas uplifts; (4) 550-450 Ma Famatinian and Pampean arc rocks of the western Sierras Pampeanas (unit pCE); (5) 340-280 Ma Carboniferous arc rocks of the Principal

Cordillera (Fig. 1A; Mpodozis and Kay, 1992); (6) 280-240 Ma Permian-Triassic arc rocks of the Choiyoi Igneous Complex, exposed in the Frontal Cordillera (unit P^); and (7) 50-0 Ma Andean magmatic arc rocks and 175-145 Ma Jurassic intrusions in the Principal Cordillera, Frontal Cordillera, and Chilean coastal ranges (Mpodozis and Kay, 1992; Ramos, 1999, 2009; Bahlburg et al., 2009; Mulcahy et al., 2014).

Results

Sediment source regions

Exposed bedrock source rocks are grouped according to their stratigraphic and lithologic context (SEGEMAR, 1999; Fig. 2). Described here are U-Pb age spectra for 9 distinguishable units that reflect a history of Paleozoic terrane accretion and Permian to Neogene subduction (Fig. 3; Table S1).

Primary sources include age components derived from: (1) unit =O foreland basement arches, with strong Famatinian-Pampean arc (550-450 Ma) and Proterozoic Sunsás (1200-1000 Ma) basement signatures (zircon age data from Casquet et al., 2001; Vujovich et al., 2004; Mulcahy et al., 2014); (2) unit P^ Permian-Triassic hinterland basement of the Choiyoi igneous complex with prominent age signatures at 280-240 Ma; and (3) unit Nv Andean magmatic arc, as represented by Neogene populations from hinterland clastic/volcaniclastic rocks in unit Ns.

Sources of recycled zircons include Paleozoic strata in the hinterland and fold-thrust belt (Fig. 2): (4) unit _O Cambrian-Ordovician strata of the eastern thrust belt with early Mesoproterozoic (1450-1350 Ma) ages and minor late Mesoproterozoic Sunsás

basement (1200-1000 Ma) signatures; (5) unit OD Ordovician-Devonian strata of the central Precordillera thrust- belt dominated by Sunsás basement (1200-1000 Ma) with minor early Mesoproterozoic (1450-1350 Ma) signatures (ages from McKenzie et al., 2016); and (6) unit CP Carboniferous-Permian strata of the western thrust belt containing Carboniferous arc (340-280 Ma), Ordovician Famatinian-Pampean arc (550-450 Ma), and Eastern Sierras Pampeanas (725-550 Ma) signatures (ages from McKenzie et al., 2016).

Mesozoic-Cenozoic zircons are sourced from hinterland, fold-thrust belt, and foreland sedimentary packages (Fig. 2): (7) unit ^ Triassic rift strata with pronounced Carboniferous arc (340-280 Ma) and late Mesoproterozoic Sunsás basement (1200-1000 Ma) signatures; (8) unit JK Jurassic-Cretaceous hinterland strata (ages from Mackaman-Lofland et al., 2015) with a broad range of Jurassic through Carboniferous ages and a major Permian-Triassic volcanic (280-240 Ma) peak; and (9) unit Ns Neogene basin fill dominated by Andean arc (50-0 Ma) ages with minor Permian-Triassic volcanic (280-240 Ma), late Mesoproterozoic basement (1200-1000 Ma), and Carboniferous arc (340-280 Ma) signatures.

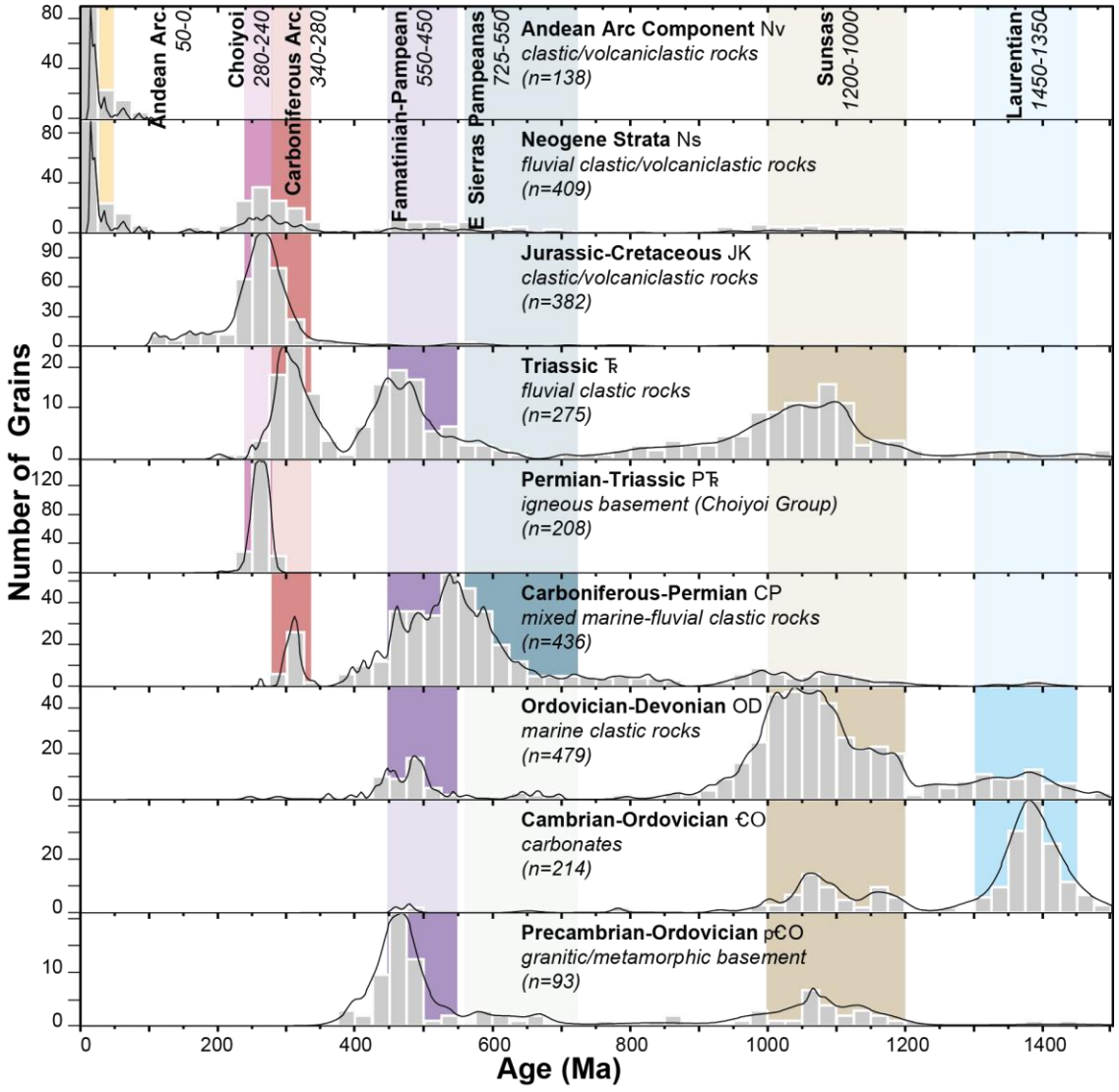
Andean Arc. 50-0
Choiyoi 280-240
Carboniferous Arc. 340-280
Famatinian-Pampean 550-450
Sierras Pampeanas 725-550
Sunsas 1200-1000
Laurentian 1450-1350
Andean Arc Component Nv
clastic/volcaniclastic rocks
(n=138)
Neogene Strata Ns
fluvial clastic/volcaniclastic rocks
(n=409)
Jurassic-Cretaceous JK
clastic/volcaniclastic rocks
(n=382)
Triassic Ŧr
fluvial clastic rocks
(n=275)
Permian-Triassic PŦr
igneous basement (Choiyoi Group)
(n=208)
Carboniferous-Permian CP
mixed marine-fluvial clastic rocks
(n=436)
Ordovician-Devonian OD
marine clastic rocks
(n=479)
Cambrian-Ordovician €O
carbonates
(n=214)
Precambrian-Ordovician p€O
granitic/metamorphic basement
(n=93)
Number of Grains
Age (Ma)

Figure 3.3: Comparative plot of U-Pb age distributions for bedrock source units, depicted as age histograms and relative probability density curves, with emphasis on diagnostic age populations (color shading) emblematic of particular units. (1) Unit =O, Precambrian and Ordovician basement (from Casquet et al., 2001; Vujovich et al., 2004; Mulcahy et al., 2014); (2) Unit _O, Cambrian and Ordovician carbonates; (3) Unit OD, Ordovician-Devonian marine clastic and metasedimentary rocks (from McKenzie et al., 2016); (4) Unit CP, Carboniferous-early Permian continental sandstones (from McKenzie et al., 2016); (5) Unit P^, Permian-Triassic felsic volcanic rocks; (6) Unit ^, Triassic continental sandstones; (7) Unit JK, Jurassic-Cretaceous marine siliciclastics (from Mackaman-Lofland et al., 2015); (8) Unit Ns, Neogene fluvial sandstones; (9) Unit Nv, represented by Neogene populations from hinterland clastic/volcaniclastic rocks from unit Ns.

Modern river sands

Main stem and tributary river sands for the (1) Bermejo, (2) Jachal, (3) San Juan, and (4) Mendoza river systems display distinct U-Pb age patterns from erosional source regions to sedimentary basin sinks (Figs. 4 and 5).

Rio Bermejo DZ U-Pb age distributions (3 samples; Fig. 4) for headwater samples RLT01 and RBV01 and distal sample RBMJ01 are dominated by Paleozoic grains with significant 550-450, 725-550, and 1200-1000 Ma populations (Fig. 4). Other components include Carboniferous arc (340-280 Ma) materials, with Permian-Triassic (280-240 Ma) basement signals absent in samples RBV01 and RBMJ01 but present in sample RLT01.

Transverse river samples for the Rio Jachal (7 samples; Fig. 4) display a downstream eastward increase in Andean arc (50-0 Ma) and associated decrease in 550-450, 725-550, and 1200-1000 Ma ages (RSJ02, RSJ01, RJAC01). Rio Jachal samples show consistent Permian-Triassic (280-240 Ma) basement ages. Wedge-top tributary samples (RDT01, RZH01) display complex distributions that include all age populations except for the Carboniferous arc (340-280 Ma). A hinterland tributary river (RAG01) has pronounced 280-240, 550-450, 725-550, and 1200-1000 Ma ages. A foreland tributary sample (RAZL01) displays complex distributions that include all signatures except the 1450-1350 Ma Laurentian basement signal.

The Rio San Juan (7 samples; Fig. 5) is a dominantly transverse river network displaying a downstream eastward increase in the number of age components, from bimodal 280-240 and 340-280 Ma signatures (RSJN02) to composite distributions (RSJN01, RSJN03) that include all populations except the 1450-1350 Ma signal. First-

order tributary river samples (RBLA01, RLC01, RCV01) show pronounced 280-240 Ma with minor 50-0 and 340-280 Ma populations. Hinterland tributary (RDLP01) displays complex distributions that includes all age signatures.

Within the Rio Mendoza (4 samples; Fig. 5), hinterland tributaries (RMDZ03) show a distinctive Jurassic (175-145 Ma) signature with minor 340-280 and 50-0 Ma components. Downstream, hinterland main stem river samples (RMDZ02, RMDZ01) have a pronounced 280-240 Ma population and a foreland river sample (RMDZ04) displays increased complexity with 50-0, 550-450, 725-550, and 1200-1000 Ma age populations.

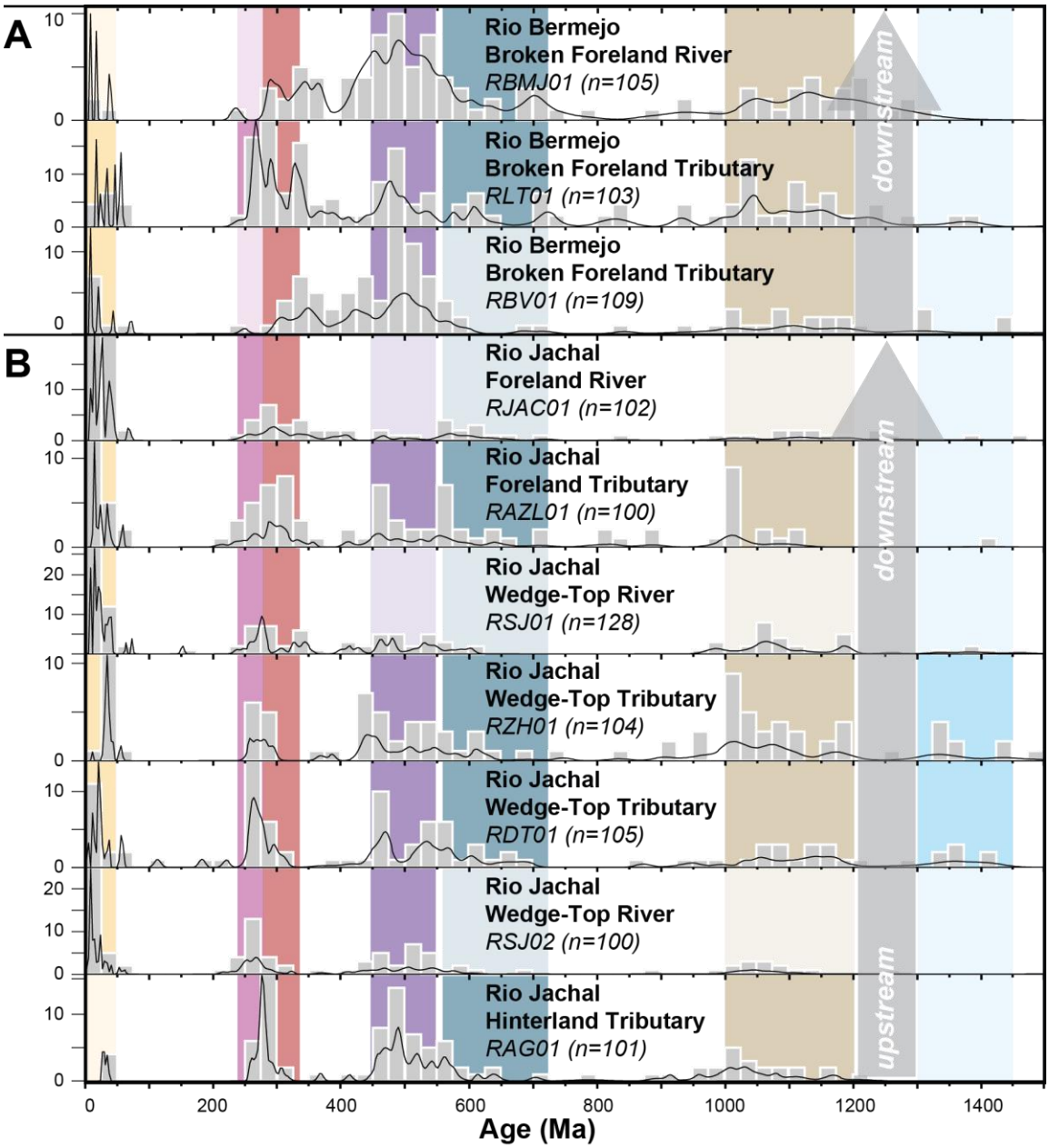
A
B
Rio Bermejo
Broken Foreland River
RBMJ01 (n=105)
Rio Bermejo
Broken Foreland Tributary
RLT01 (n=103)
Rio Bermejo
Broken Foreland Tributary
RBV01 (n=109)
Rio Jachal
Foreland River
RJAC01 (n=102)
Rio Jachal
Foreland Tributary
RAZL01 (n=100)
Rio Jachal
Wedge-Top River
RSJ01 (n=128)
Rio Jachal
Wedge-Top Tributary
RZH01 (n=104)
Rio Jachal
Wedge-Top Tributary
RDT01 (n=105)
Rio Jachal
Wedge-Top River
RSJ02 (n=100)
Rio Jachal
Hinterland Tributary
RAG01 (n=101)
downstream
upstream
0
200
400
600
800
1000
1200
1400
Age (Ma)

Figure 3.4: Comparative plot of detrital zircon U-Pb age distributions for modern river sands, depicted as age histograms and relative probability density curves, with emphasis on key populations (color shading). Sample locations shown in Fig. 2B. (A) Rio Bermejo axial river headwaters Rio Bermejo RBV01 and Rio La Troya RLT01 and distal broken foreland Rio Bermejo RBMJ01. (B) Rio Jachal transverse drainage network; hinterland tributary Rio Agua Negra RAG01; wedge-top transverse river Rio Jachal west RSJ02 and east RSJ01; wedge-top axial tributaries Rio De Tranca RDT01 and Rio Zonda Honda RZH01; foreland transverse river Rio Jachal RJAC01; and foreland alluvial fan tributary Rio Azul RAZL01.

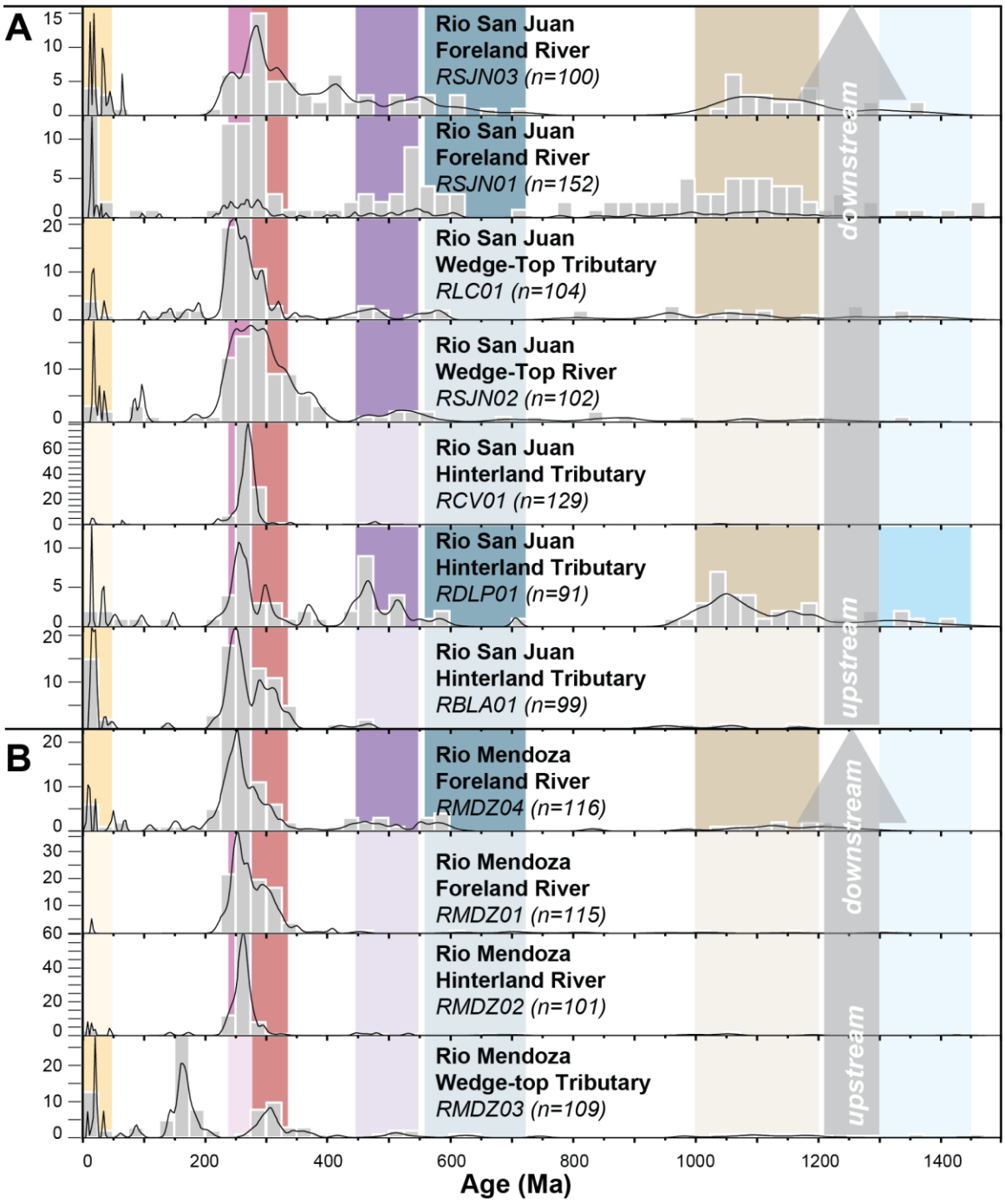
A
Rio San Juan
Foreland River
RSJN03 (n=100)
Rio San Juan
Foreland River
RSJN01 (n=152)
Rio San Juan
Wedge-Top Tributary
RLC01 (n=104)
Rio San Juan
Wedge-Top River
RSJN02 (n=102)
Rio San Juan
Hinterland Tributary
RCV01 (n=129)
Rio San Juan
Hinterland Tributary
RDLP01 (n=91)
Rio San Juan
Hinterland Tributary
RBLA01 (n=99)
B
Rio Mendoza
Foreland River
RMDZ04 (n=116)
Rio Mendoza
Foreland River
RMDZ01 (n=115)
Rio Mendoza
Hinterland River
RMDZ02 (n=101)
Rio Mendoza
Wedge-top Tributary
RMDZ03 (n=109)
downstream
upstream
0
200
400
600
800
1000
1200
1400
Age (Ma)

Figure 3.5: Comparative plot of detrital zircon U-Pb age distributions for modern river sands, depicted as age histograms and relative probability density curves, with emphasis on key populations (color shading). Sample locations shown in Fig. 2B. (A) Rio San Juan transverse drainage network; hinterland rivers Rio Blanco RBLA01, Rio de los Patos RDLP01, Rio Castaño Viejo RCV01; wedge-top transverse river Rio San Juan RSJN02; wedge-top axial river Rio La Cieneaga RLC01; foreland Rio San Juan west RSJN01 and east RSJN03. (B) Rio Mendoza transverse drainage network; wedge-top tributary Rio de las Cuevas RMDZ03; hinterland basin river Rio Mendoza RMDZ02; foreland basin river Rio Mendoza west RMDZ01 and east RMDZ04.

FORWARD MODELS BASED ON CATCHMENT AREA

Model construction

Forward models were constructed to test whether river DZ U-Pb age distributions accurately reflect the relative proportions of geologic units exposed in their respective catchment areas (Figs. 2B and 6). Following previously defined methods (Saylor et al., 2013 and references therein), individual catchments were designated using ArcGIS (ArcHydro tool extension) and 30 m resolution ASTER II digital elevation data (courtesy of METI and NASA). Geologic units were compiled from a 1:3,000,000 regional map (SEGEMAR, 1999; Fig. 2), allowing for delineation of contributing surface areas for all units within each catchment (Fig. 6A). Local water bodies and Quaternary alluvium were considered negligible sources and excluded from bedrock area calculations.

Each forward model scales the source bedrock probability density function (PDF) (Fig. 3) by the relative exposure (outcrop) area within the contributing catchment upstream of each river sample location. For each sample, relative exposure area values (0-100 %) are compiled in a 1×9 vector with each column representing exposure area of bedrock sources. Thus, the U-Pb age distributions for the 9 bedrock sources are represented by a 9×1500 matrix (with 1 Myr column intervals representing the relative probability over a 0-1500 Myr age range and rows representing each bedrock source in the catchment). Each model sums the 9 source distributions, as scaled by exposure area, to yield an area-weighted forward model PDF for each catchment (Fig. 6B).

Comparative statistical methods

Commonly applied statistical tests for DZ U-Pb datasets involve direct comparisons of PDF values across multiple samples and their relative age spectra (Saylor and Sundell, 2016). Three statistical measures of similarity are employed in order to compare predicted PDFs with actual river DZ data: cross-plot R^2 (CP-R^2), likeness, and similarity (Fig. 6C; Table S2).

Similarity (S) measures whether a modeled age distribution and actual dataset have comparable modal sub-intervals and proportions of components in each mode (Gehrels, 2000). The similarity Equation (1) is defined as

$$(1) \qquad S = \sum_{i=1}^{n} \sqrt{f(i)g(i)}$$

where f(i) and g(i) are PDFs over the age interval (n) of interest. Endmember values represent either a perfect match in mode and magnitude (S = 1) or two age distributions sharing no modes (S = 0).

Likeness (L) considers the area mismatch (M) between the model and actual PDFs f(i) and g(i) (Amidon et al., 2005a; 2005b; Satkoski et al., 2013), such that the area mismatch (M) is calculated as Equation (2)

$$(2) \quad M = [\sum_{i=1}^{n} |f(i) - g(i)|]/2$$

With likeness (L) defined as Equation (3)

$$(3) \quad L = 1\text{-}M$$

Cases with no area mismatch show considerable likeness (L = 1), whereas cases with complete area mismatch yield negligible likeness (L = 0).

Relative probability cross-plots measure distribution similarity, where a modeled PDF is plotted against the actual PDF (Saylor et al., 2013). The PDF cross-plot coefficient R^2 value (CP-R^2) represents a line fitted among the probability distributions, providing a quantitative assessment of the degree of similarity. The cross-plot coefficient is sensitive to the presence and absence of age components, as well as variations in relative magnitude or shape in the density peak. Modeled and actual PDFs with identical age components and probability density magnitudes result in high coefficients (CP-R^2 = 1), in contrast to PDFs that share no age components (CP-R^2 = 0).

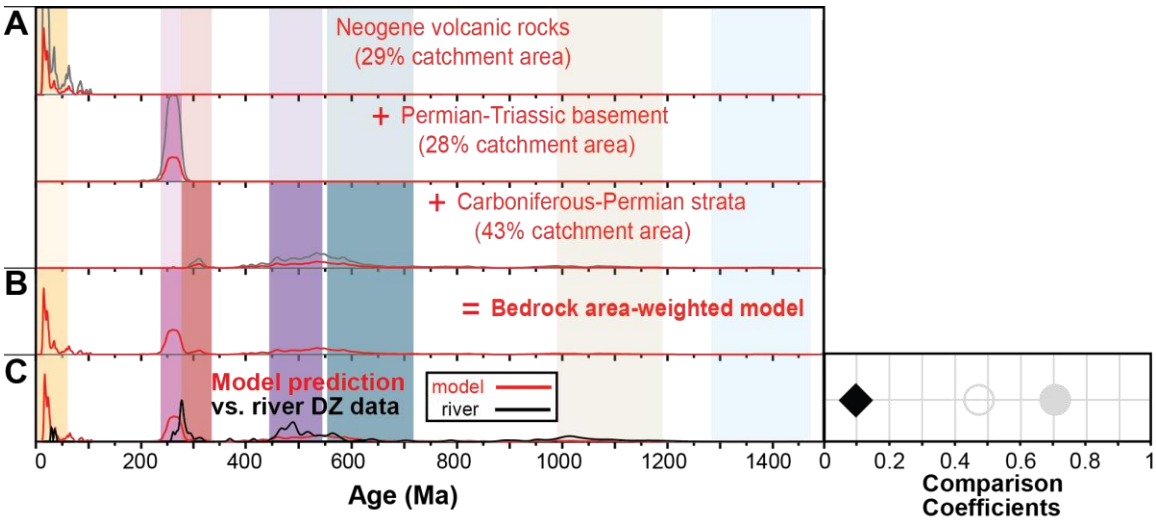

Figure 3.6: Schematic plot of detrital zircon U-Pb age distributions showing the construction of an area-weighted model and comparison of model predictions with results for a river sand sample. (A) PDF (probability density function) plots for the three exposed geologic units (black curves) scaled proportionally to the relative exposure areas in the drainage catchment (red curves). (B) Composite PDF plot (the sum of the three curves in A) showing the model prediction of an area-weighted age distribution. (C) Comparative PDF plot showing the model predictions (red curve) and actual age distribution (black curve) for a modern river sand sample (RAG01), along with a plot of calculated statistical coefficients using cross-plot R^2 (CP-R^2; black diamond), likeness (open grey circle), and similarity (closed grey circle).

Results

River DZ U-Pb results (Figs. 7 and 8) are organized according to basin configuration (hinterland, wedge-top, foreland, and distal broken foreland) to elucidate any trends in the statistical comparison of model predictions and river sand age distributions. The full array of comparison coefficients are considered in order to distinguish a relatively good fit from a poor fit. Results show average (and minimum-maximum) comparison coefficient values as follows: CP-R^2 = 0.32 (0.02-0.92); L= 0.54 (0.27-0.77); S=0.79 (0.53-0.91) (Table S2). The observed range of CP-R^2 values suggest that these statistical measures are most sensitive to mismatches between modeled and observed age distributions. For this study, we consider CP-R^2 values < 0.25 to be poor fits, values between >0.25 and <0.50 to be moderate fits, and values >0.50 to be good fits.

Hinterland basins

Drainage areas for hinterland transverse river samples (RMDZ02, RBLA01, RDLP01, and RCV01) range from 4440-8374 km^2 with a single smaller (RAG01) 423 km^2 catchment. Hinterland catchments are dominated by Neogene volcanics (unit Nv) and Permian-Triassic Choiyoi igneous basement (unit P^), with RAG01 and RMDZ02 also tapping Carboniferous-Permian (unit CP) and Jurassic-Cretaceous (unit JK) strata, respectively (Table S2). Predicted age distributions reflect the exposed source units and display strong Andean arc (50-0 Ma) and Choiyoi (280-240 Ma) age components (Fig. 7B). However, observed DZ ages for samples RAG01, RCV01, and RDLP01 differ from model predictions, with a distinct lack of Andean arc ages (50-0 Ma) and appearance of Famatinian-Pampean arc (450-550 Ma) and late Mesoproterozoic Sunsás basement (1200-

1000 Ma) ages. The modeled age distributions predict a persistent Permian-Triassic age component and northward increase in Neogene ages. Complementing this trend is a northward decrease in correlation between modeled and observed age distributions. Southern hinterland samples RMDZ02 and RBLA01 display the best fits, with CP-R^2 coefficients of 0.92 and 0.63. The northernmost samples (RAG01 and RCV01) display a northward decrease to CP-R^2 values of 0.10 and 0.27.

Wedge-top basins

Wedge-top basin samples (Fig. 7A) represent sharply contrasting catchment areas, including smaller, first-order axial tributaries (RLC01, RMDZ03, RDT01, and RZH01) averaging 130 km^2 and larger, second-order transverse main stem river catchments (RSJ01, RSJ02, and RSJN02) averaging 24,200 km^2 (Table S2). These contrasting drainage areas display a distinctly bimodal distribution of CP-R^2 values in which first-order axial tributaries show poor fits (average CP-R^2 = 0.09) and second-order transverse rivers exhibit relatively better fits (average CP-R^2 = 0.32) (Fig. 9). Tributary river exposure areas are typically dominated by Paleozoic bedrock (units OD and _O), with the exception of RMDZ03 with significant exposures of Mesozoic strata (unit JK) (Fig. 1; Table S2). Resulting modeled ages for tributary samples (RLC01, RMDZ03, RDT01, RZH01) predict enhanced Paleozoic and Precambrian age signatures, with 340-280, 550-450, 725-550, and 1200-1000 Ma age components and little to no Cenozoic ages.

Observed ages are remarkably younger, with significant Andean arc (50-0 Ma), anomalous Jurassic ages (175-145 Ma), and Choiyoi igneous ages (280-240 Ma). The

larger transverse rivers consist of drainage areas that expose units Nv and P^ (20-40% each), with minor exposure areas of units Ns, CP, and OD (<20% each). Modeled age distributions for transverse river samples (RSJ01, RSJ02, and RSJN02) predict significant Andean arc and Permian-Triassic age components with a low proportion of Paleozoic age components. Observed ages for wedge-top main stem and transverse rivers (RSJ01, RSJ02, and RSJN02) display variations among Andean arc and Choiyoi igneous age components with minor Paleozoic components. Sample RSJN02, from western Rio San Juan, displays a moderate match between modeled and observed Andean arc age components, a common trend for Rio San Juan samples (Fig. 7).

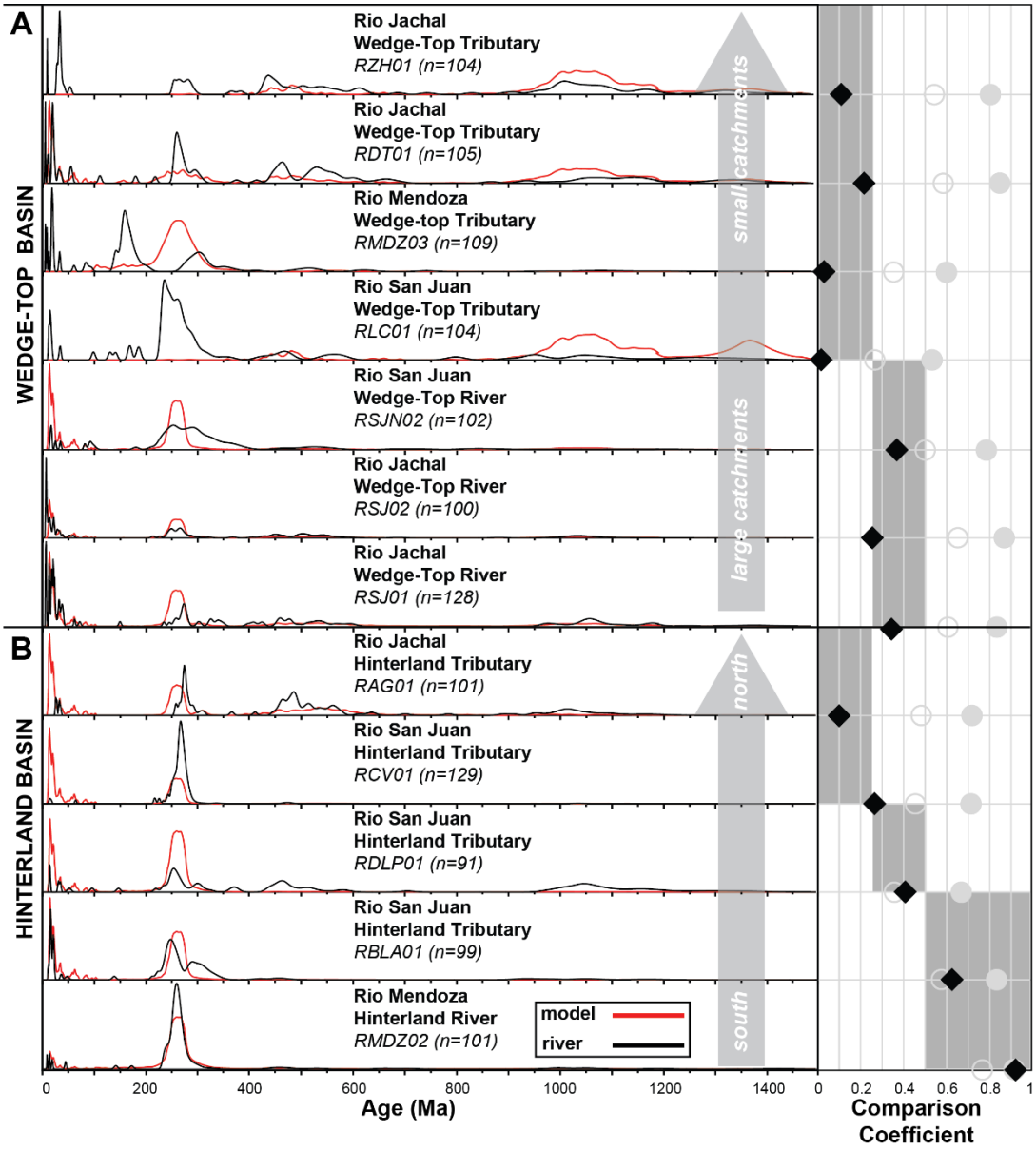

Figure 3.7: Comparative plots of detrital zircon U-Pb age distributions showing area-weighted model predictions (red curves) and modern river age distributions (black curves) for (A) wedge-top basin and (B) hinterland basin samples (Figs. 4 and 5; sample locations Fig. 2B), along with a plot of calculated statistical coefficients: CP-R^2 (black diamond), likeness (open grey circle), and similarity (closed grey circle). Grey rectangles delineate a samples range of coefficient values: < 0.25 (poor fits), >0.25 and <0.50 (moderate fits), and >0.50 (good fits). (A) Wedge-top results are plotted bottom to top

from largest to smallest catchment size (km^2). (B) Hinterland basin results are plotted based on latitude from south to north.

Foreland basins

Foreland basin samples from the Rio Mendoza (RMDZ01, RMDZ04), Rio San Juan (RSJN01, RSJN03), and Rio Jachal (RAZL01, RJAC01) drainage networks produce the most robust model fits, with an average CP-R^2 coefficient value of 0.49 (Fig. 8B). In these foreland (foredeep) settings, transverse river systems with large catchments areas (Rio Mendoza: 8,858 km^2; Rio San Juan: 55,329 km^2; and Rio Jachal: 29,944 km^2) feed fluvial megafan fluvial systems. An exception is an alluvial fan (RAZL01) draining a small 20 km^2 area (Table S2). Exposure areas are dominated by Permian-Triassic igneous basement (unit P^） in the hinterland (27-54%). Whereas Rio Mendoza samples (RMDZ04 and RMDZ01) tap outcrops of unit JK (20%) and unit ^ (12%), Rio San Juan (RSJN01 and RSJN03) and Rio Jachal (RJAC01 and RAZL01) samples have more Cenozoic and Paleozoic exposure areas of units Nv and Ns (32-80%) and unit OD (20%) (Table S2). Predicted age distributions are dominated by Andean arc (50-0 Ma) and Permian-Triassic (280-240 Ma) ages with minor Famatinian-Pampean arc (550-450 Ma) and Sunsás basement (1200-1000 Ma) components (Fig. 8B). For Rio Mendoza (RMDZ01 and RMDZ04), predicted age distributions have strong Choiyoi (280-240 Ma) and minor Andean arc (50-0 Ma) signatures, both of which are observed in river sand ages. For Rio San Juan (RSJN01 and RSJN03) and Rio Jachal (RAZL01 and RJAC01), the model predictions overestimate the Choiyoi age (280-240 Ma) component, with minor variation

in Andean arc ages (50-0 Ma). The modeled ages tend to correctly predict older Paleozoic and Precambrian age components 550-450, 725-550, and 1200-1000 Ma.

Distal broken foreland

Rio Bermejo samples represent a broken foreland basin and have poor average fits (CP-R^2 = 0.07) (Fig. 8A). Transverse rivers from broken foreland headwaters (RLT01 and RBV01), with drainage areas of 2000-7000 km^2, feed the large Rio Bermejo axial system (RBMJ01) encompassing an extensive drainage area (66,558 km^2). The RLT01 drainage area contains mostly Paleozoic strata, unit OD (50%), with subordinate units Ns, CP, and =O (~15% each). The RBV01 catchment is dominated by Neogene volcanic rocks and Paleozoic strata (~30% each), with minor Ns and =O (11% and 19% respectfully). Modeled distributions for RBV01 predict a major Andean arc (50-0 Ma) age component, due to significant Nv and Ns catchment exposures. Modeled distributions for RLT01 predict significant Famatinian-Pampean (550-450 Ma) and late Mesoproterozoic Sunsás basement (1200-1000 Ma) populations. Modeled ages for RBMJ01 predict significant Andean arc (50-0 Ma) and Permian-Triassic (280-240 Ma) age components, with minor Famatinian-Pampean (550-450 Ma) and Sunsás (1200-1000 Ma) age peaks.

Observed ages of broken foreland river sands are dominated by Famatinian-Pampean (550-450 Ma) and Neoproterozoic rocks of eastern Sierras Pampeanas (725-550 Ma), significant Sunsás basement (1200-1000 Ma) and Carboniferous arc (340-280), and minor Andean arc (50-0 Ma) ages. Broken foreland samples show a trend between CP-R^2 value and drainage area, where larger catchments display poorer model fits. For example,

sample RBMJ01 represents the largest catchment but displays the poorest fit (CP-R^2 = 0.02) in the study. This case reflects an interesting situation where the area model predicts a significant Permian-Triassic age signature from hinterland sources, but that signal is entirely missing.

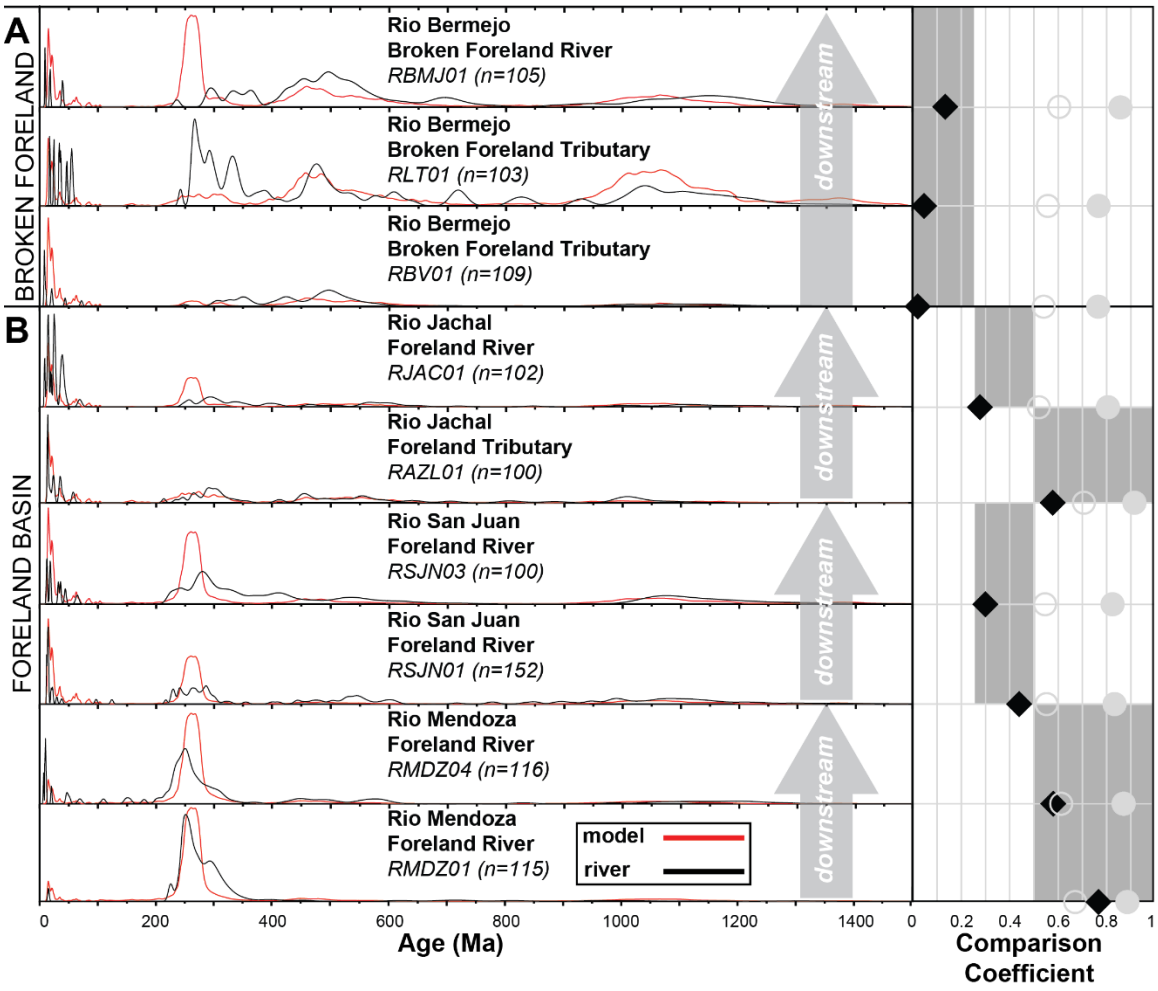

Figure 3.8: Comparative plots of detrital zircon U-Pb age distributions showing area-weighted model predictions (red curves) and modern river age distributions (black curves) for (A) broken foreland and (B) foreland basin (Figs. 4 and 5; sample location Fig. 2B), along with a plot of calculated statistical coefficients: CP-R^2 (black diamond), likeness (open grey circle), and similarity (closed grey circle). Grey rectangles delineate a range of coefficient values: < 0.25 (poor fits), >0.25 and <0.50 (moderate fits), and >0.50 (good fits). (A) Broken foreland results are plotted from bottom to top, from north to south (proximal to distal), for the Rio Bermejo axial river. (B) Foreland results are plotted by transverse river network, from bottom to top, for the Rio Mendoza, Rio San Juan, and Rio Jachal, with pairings from west to east (proximal to distal).

DISSCUSSION

Several factors may explain mismatches in observed versus predicted DZ U-Pb age distributions for modern river sands of the Andean orogen and associated sedimentary basins. The forward models generated in this study represent uniform contributions, normalized by exposure area, from across each erosional drainage network. Departures of actual DZ data from predicted distributions reveal cases where specific bedrock sources disproportionately contribute sediment to their respective catchments, highlighting the impact of variable erosion patterns, zircon fertility, lithologic durability, and/or downstream mixing and dilution on resulting provenance signatures. An important next step is to begin to evaluate the relative influence of these factors across a complete contractional orogen, through an array of different retroarc basin configurations and their affiliated depositional systems.

Local variations in hinterland basins

Hinterland river DZ age distributions in the study region depart from the predictions of the area weighted model, potentially because exposed igneous sediment sources display along-strike variations in catchment erosion and/or zircon fertility. These variations reflect contrasting river morphologies and stream erosion patterns across the diverse topography of the Frontal Cordillera (Fig. 2), which consists of: (1) an elevated, low-relief hinterland region capped by Neogene deposits (units Nv and Ns); (2) a high-relief (>1000 m) fault-bounded block with deeply incised Permian-Triassic basement rocks (notably unit P^); and (3) a low-relief hinterland basin with alluvial-fan deposition.

The contrast in relief potentially leads to disproportionate catchment erosion and sediment flux from different hinterland source units. Specifically, higher channel gradients and focused basement erosion across the Frontal Cordillera range front (e.g., Hoke et al., 2015) likely induce greater contributions from Carboniferous–Triassic units (units CP, P^) and recycled Cenozoic basin fill (units Ns). When combined with diminished input from the lower relief, less erosive landscapes upstream (units Nv and JK), this trend may explain the distinct lack of Andean age components (samples RAG01, RCV01, RDLP01).

Alternatively, hinterland results may be the product of high zircon fertility (i.e., high Zr ppm or zircon weight %), where bedrock source areas exceed the contributions predicted by the equal-area contribution model (see Malusá et al., 2016). Zircon fertility estimates using Zr ppm agree well with source rock zircon modal abundances, since no other mineral phases incorporate Zr in significant amounts (Dickinson, 2008). In this study, higher zircon fertility for the extensive Permian-Triassic plutonic/volcanic crystalline basement unit may contribute a disproportionate and greater volume of zircon grains than Neogene volcanic sources. This interpretation is compatible with observed Zr concentrations, with average Zr concentration of 272 ppm versus 178 ppm for the Choiyoi Group (unit P^) relative to Miocene igneous rocks (unit Nv) (Stazzere et al., 2006; Kleiman and Japas, 2009; Maydagán et al., 2011). The issue of zircon fertility may be particularly acute for hinterland basins, where sedimentary sinks are in close proximity to magmatic arc and crystalline basement sources.

Another potential factor involves variable erodibility, in which Neogene volcanic rocks may be more easily eroded than Permian-Triassic basement sources. This prediction,

however, is at odds with the observed trend, suggesting that focused erosion or enhanced basement fertility outpaces the erodibility effect. An along-strike (northward) increase in Neogene volcanic rocks relative to Permian-Triassic sources correlates with a decrease in the CP-R^2 coefficient, suggesting that high basement zircon fertility disproportionally affects hinterland settings (Fig. 9A). Although not unexpected, this relationship underscores the potential for considerable provenance variations in the more-proximal hinterland segments of contractional orogens with greater proportions of zircon-rich crystalline rocks and shorter transport distances.

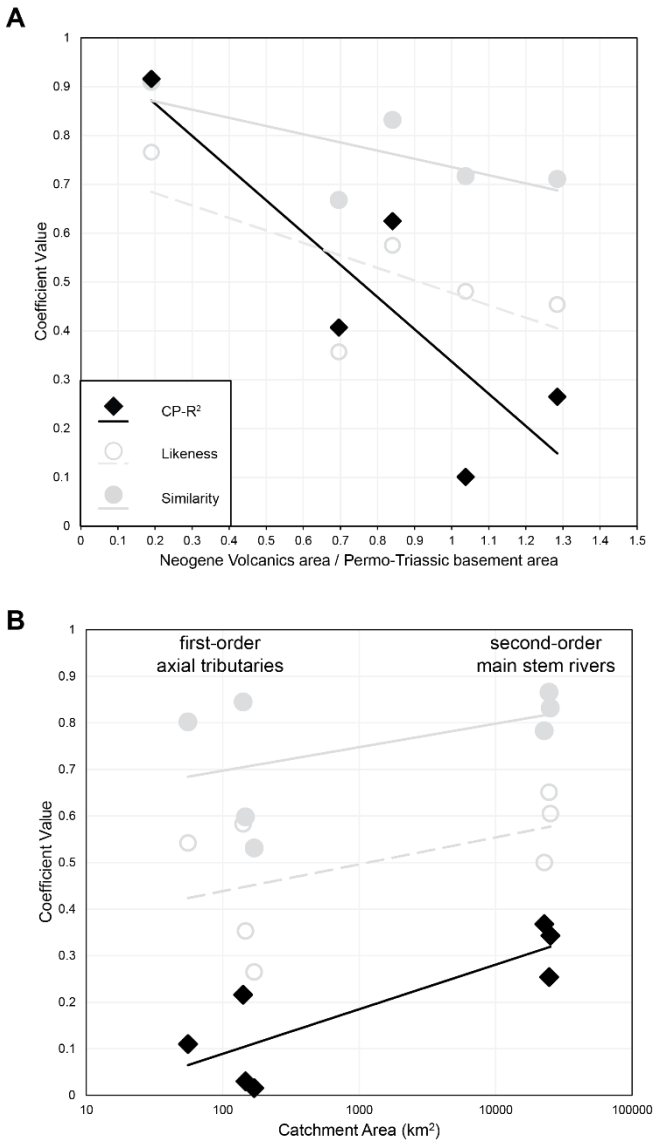

Figure 3.9: Diagrams showing statistical results comparing (A) ratio between Neogene volcanic rocks (unit Nv) and Permian-Triassic igneous basement (unit P^) exposure areas among hinterland basin river catchments, relative to calculated statistical coefficients: CP-R^2 (black diamond), likeness (open grey circle), and similarity (closed grey circle). (B) Positive correlation among wedge-top basin main stem and tributary river sample catchment area size, relative to sample calculated comparison coefficients.

Variable erodibility within wedge-top basins

The structural configuration of retroarc fold-thrust belts represents a dominant control on bedrock exposure patterns, drainage organization, and sediment accumulation in narrow wedge-top basins. In these basin settings, sand provenance can be divided into (1) first-order samples from axial tributaries that flow along strike, and (2) second-order samples from transverse rivers that cut across orogenic strike (Fig. 9B). These two contrasting drainage systems exhibit a bimodal distribution of comparison coefficients. For first-order axial tributaries with smaller catchment areas (samples RLC01, RMDZ03, RDT01, RZH01; Fig. 9B), low CP-R^2 coefficients are the result of higher concentrations of Mesozoic and Neogene zircons compared to area-weighted model predictions (Fig. 7A). A relatively poor goodness of fit between the area-weighted model and observed river sediment age distributions is largely due to preferential recycling of erodible sedimentary units within axial tributary networks. Erodible Neogene sandstones (unit Ns) are preserved locally in the footwalls of Precordillera thrust faults that exhume durable Paleozoic strata (units _O, OD, CP). Despite the limited exposure area of Neogene basin fill, disproportionate contributions of Neogene zircons reflect the high erodibility of young basin fill, which is readily eroded and mobilized by axial tributaries within the Precordillera (Fig. 2).

Preferential erosion of Neogene basin fill is less significant for second-order samples of transverse rivers (e.g., Rio San Juan and Rio Jachal), for which area-weighted models provide a better match to observed age distributions (RSJ01, RSJ02, RSJN02; Fig. 7A). However, statistical coefficients are potentially influenced by along-strike variations

in zircon fertility for hinterland igneous units (Nv and P^). Notably, Rio San Juan samples that tap the southern Frontal Cordillera (Fig.2B) are enriched in Permian-Triassic Choiyoi ages relative to model predictions (RSJN02 (Fig. 7A) and RBLA01, RDLP01, and RCV01 (Fig. 7B)). This trend also correlates with a contrast in average Zr concentration of 251 versus 103 ppm for upper Choiyoi and lower Choiyoi rocks (Kleiman and Japas, 2009), which dominate the Rio San Juan and Rio Jachal catchments, respectively. The inherited zircon fertility variations in thrust-belt rivers result in an abundance of Permian-Triassic age zircons in the Rio San Juan drainage network (RSJN02, RLC01; Figs. 5A and 7B), and Andean age zircons in the Rio Jachal network (RSJ01, RSJ02, RDT01, RZH01; Figs. 4B and 7B). In summary, river sand DZ provenance in wedge-top basin systems is affected by drainage order and respective sampling scale (Ingersoll, 1993; Horton and DeCelles, 2001). Whereas preferential recycling of erodible sedimentary units governs first-order tributary river age distributions, variations among zircon fertility and lithologic durability have a minor influence on second-order, main stem river age distributions.

Provenance signal in foreland basins

Foreland basin (foredeep) depositional patterns are dominated by large (second-order) point-source fluvial megafans and interfan (first-order) alluvial fans (Damanti, 1993; Horton and DeCelles, 2001). Proximal foreland samples (Fig. 2) characterize megafans of the Rio Jachal (RJAC01), Rio San Juan (RSJN01, RSJN03), Rio Mendoza (RMDZ01, RMDZ04), and associated interfan areas (RAZL01). Provenance patterns for these systems are accurately predicted by area-weighted models (average CP-R^2 = 0.49),

suggesting that foredeep deposits robustly record DZ provenance characteristics of their respective drainage catchments (Fig. 8). The foredeep provenance signal more accurately reflects source unit distributions than localized wedge-top basins and may reflect a better regional integration of erosion patterns across the fold-thrust belt. In contrast, more-proximal wedge-top and hinterland basin settings with shorter transport distances (i.e., smaller order streams) are more susceptible to local variations, an important issue previously recognized in other sediment provenance studies (Ingersoll, 1990; Ingersoll et al., 1993).

An important caveat here is that more complex age distributions (i.e., multiple age components) can prove challenging for the forward models (Fig. 8). Whereas relatively simple catchments draining igneous sources are well predicted by an area weighted model (e.g. RMDZ01, RMDZ04; Fig. 7B), large drainage networks (>20,000 km^2) sourcing a suite of recycled sedimentary units (e.g. RSJN01, RSJN03; Fig. 8B) produce highly variable age distributions that are difficult to accurately predict given the limited sampling resolution and quality of catchment metrics (Table S2).

Signal dilution by foreland basement uplifts

Broken foreland basins commonly include axial rivers that originate in the fold-thrust belt and flow parallel to basement arches in the distal foreland (Jordan, 1995). Broken foreland samples (RBMJ01, RBV01, RLT01) from axial fluvial systems influenced by Precambrian basement arches display relatively poor model comparisons (average of 0.07 CP-R^2 value) with disproportionate contributions from basement arches (unit =O) and

overlying Mesozoic strata (units JK and ^). This trend is attributed to signal dilution due to increased sediment input from basement arches of the distal foreland, thus overwhelming the signal of thrust-belt-derived fluvial megafans in the west. Whereas fluvial megafan transport distances are on the order of 100 km, fringing alluvial fans transport sediment on the order of 10 km away from basement arches. Nevertheless, efficient sediment transport across these short, high-relief alluvial fans appears to provide considerable amounts of homogenous DZ ages from basement arches and overlying Mesozoic strata units =O and ^. This drainage configuration and the progressive introduction of new sources areas downstream leads to a decrease in DZ populations from thrust-belt and hinterland sources. In some extreme cases, this dilution effect results in complete aliasing of such DZ signals, as observed for the Rio Bermejo (RBMJ01) with the loss of hinterland Permian-Triassic igneous signatures. Broken foreland river sands in this study illustrate the disproportionate effect of local bedrock sources and diminished sensitivity to sediment input from the fold-thrust belt and hinterland.

Predicting disproportionate detrital zircon contributions in ancient systems

U-Pb ages from modern river sediments in diverse drainage systems help elucidate provenance trends in ancient sedimentary records (Fig. 10). As shown here, DZ results can display either provenance signal stability (area-proportional) or strong variability (area-disproportional) as a function of contrasting basin configurations in an Andean-type retroarc contractional system, providing insights into bedrock contributions across variable

structural, sedimentary, and geomorphic conditions. Here we consider potential factors that produce disproportionate DZ contributions for each contractional basin system.

(1) Basement-involved structures generate drainage networks that deliver sediment to hinterland basins within an orogen. Area-weighted models consistently overestimate sediment contributions from volcanic cover relative to crystalline basement. Observed provenance results are disproportionately influenced by local fault-generated relief and variable zircon fertility from exposed igneous units (Fig. 10). Hinterland basins adjacent to magmatic arcs record DZ age distributions from syndepositional volcanism (Horton et al., 2015a, 2016) and area-disproportionate DZ contributions associated with exhumation along high-angle, basement involved structures. Even though the DZ signal is disproportionate to exposure area, these basins should faithfully record shortening along hinterland structures. Constraining the area-disproportional mismatch associated with zircon fertility requires measuring the zircon weight % or Zr ppm of potential sediment sources and applying scaling factors to DZ age distributions (Dickinson, 2008; Malusá et al., 2016).

(2) Mismatches between river DZ populations and area-weighted model predictions suggest wedge-top basin provenance is dictated by erodibility contrasts between recycled basin fill and thrust-belt bedrock sources (Fig. 10A and 10B). Modern wedge-top basins within thin-skinned fold-thrust belts consist of orogen-parallel, axial tributaries that show recycled DZ age contributions from erodible footwall basin sources, which are overrepresented with respect to more-durable hanging-wall bedrock sources. Hence, DZ spectra of wedge-top basins are dominated by recycled sediments, even when exposure

area is limited. Thrust-belt provenance in proximal wedge-top settings will be difficult to reconcile due to the significant degree of sediment recycling. Where syntectonic wedge-top basins record continuous recycling of relatively older basin fill, resulting in an invariant DZ provenance trend through time. Requiring additional provenance insights from sandstone or conglomerate clast compositions and thermo/geochronological proxies, to help approximate the degree of sediment recycling.

(3) Unlike their elevated proximal counterparts (wedge-top and hinterland basins), foreland basins accurately reflect hinterland and thrust-belt source regions (Fig. 10). Provenance results from foreland basin (foredeep) river and fluvial megafan systems reveal the limited effects of zircon fertility, lithologic durability, and local erosion fluxes for such large (>20,000 km^2) second-order drainage systems. Modern foredeep and megafan samples are less susceptible to the vagaries observed in proximal settings (e.g., Ingersoll et al., 1993) and are the most consistent and reliable recorders of provenance characteristics in contractional retroarc systems (Horton and DeCelles, 2001).

(4) In broken foreland basins, drainage networks are dominated by axial trunk rivers that mark the intersection of point-source fluvial megafan distributive systems derived from the fold-thrust belt and fringing line-source alluvial fans shed from basement cored arches (Fig. 10). Although area-weighted forward models predict considerable detrital age populations from hinterland and fold-thrust belt sources, they are not well represented in river DZ age spectra. This mismatch between model predictions and observed age spectra suggests that the age signatures from thrust-belt and hinterland river systems are readily diluted by detrital contributions from basement-cored foreland uplifts. More generally, this

trend suggests that broken foreland basin systems (Dickinson et al., 1988) are less sensitive to retroarc hinterland and thrust belt processes and particularly well suited to reflect proximal derivation from basement-involved uplifts in the distal foreland.

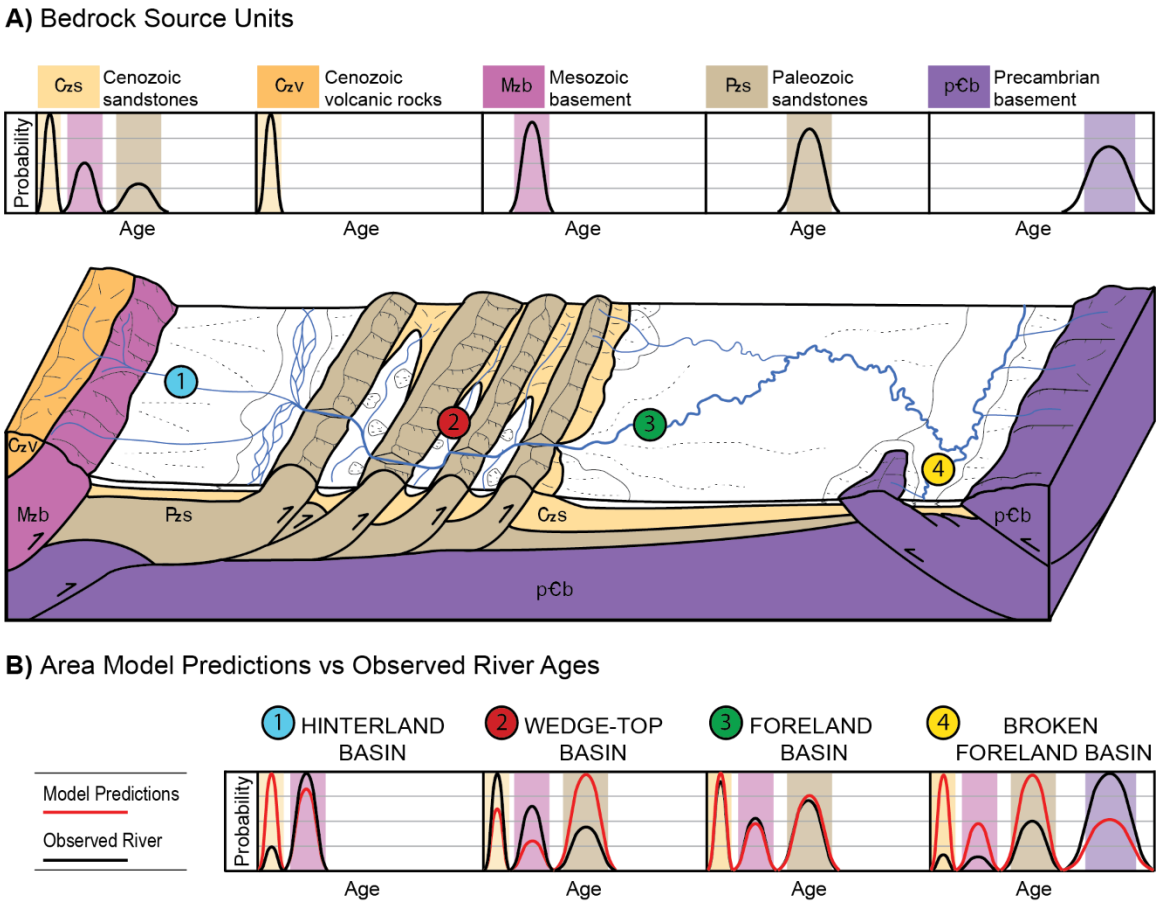

Figure 3.10: Conceptual diagram depicting schematic detrital zircon (DZ) age distributions for different contractional basin systems of an idealized retroarc foreland setting and 3D block diagram showing major source units and drainage configurations. Age probability distributions show: (A) predicted DZ ages from area-weighted models assuming bedrock contributions proportional to exposure areas within catchments; (B) proposed DZ ages for modern rivers in each basin setting, as influenced by zircon fertility, lithologic durability, and signal dilution on river provenance; (C) hypothetical bedrock sources DZ ages in retroarc settings.

CONCLUSIONS

Here we show that differences between river sand provenance and predictions of an area-weighted forward model for a contractional orogen can be linked to contrasts in the structural configuration of the sediment sink—namely variations among hinterland, wedge-top (piggyback), foreland (foredeep), and broken foreland basin settings. Forward modeling of detrital zircon (DZ) U-Pb age distributions weighted by source bedrock exposure area predicts an expected river DZ signature. By quantifying goodness of fit between model predictions and observed DZ spectra, we assess the influence of lithologic erodibility, zircon fertility, and signal dilution by locally focused erosion. In the Andean study region, hinterland basin provenance is disproportionately affected by local thrust-generated relief and the variable zircon fertility of exposed igneous sources. Differences among wedge-top (piggyback) basin provenance is potentially controlled by the greater erodibility of recycled basin sediments relative to thrust-belt bedrock sources. Unlike the more-proximal hinterland and wedge-top zones, foreland basins accurately reflect the distribution of source units within retroarc hinterland and thrust belt catchment areas. However, in broken foreland basins, drainage networks are dominated by axial trunk rivers, where thrust-belt and hinterland age signatures are readily diluted by local contributions from foreland basement-cored uplifts. Factors influencing modern DZ provenance such as proximal to distal mixing effects, variable erosion patterns, and zircon source fertility potentially can be applied to ancient basins to yield more robust investigation of potential sources, structural setting, and drainage network. Further work in quantifying the lithologic

erodibility, durability, zircon fertility, and sediment supply across a range of study regions will help improve predictive models of DZ provenance.

ACKNOWLEDGMENTS

This research was funded by the Geological Society of America, American Association of Petroleum Geologists, and Jackson School of Geosciences at the University of Texas at Austin (grants awarded to T.N. Capaldi) and support from the U.S. National Science Foundation (grant EAR 1348031 awarded to B.K. Horton and N.R. McKenzie). We thank Patricia Alvarado, Gustavo Ortiz, Chelsea Mackaman-Lofland, Sebastian Ramirez, and Facundo Fuentes for discussions and logistical assistance in Argentina. This manuscript benefited from discussions with Greg Hoke, Joel Saylor, Kurt Sundell, Kelly Thomson, Lily Jackson, Sarah George, and Lisa Stockli. The constructive comments of reviewers Alan Chapman and Andres Folguera were helpful in improving the original manuscript.

Appendices

APPENDIX 1.1: DETRITAL ZIRCON LU-HF RESULTS

Spot	$^{176}Yb/^{177}Hf$	±(1σ)	$^{176}Lu/^{177}Hf$	±(1σ)	$^{176}Hf/^{177}Hf$	±(1σ)	t* (Ma)	$(^{176}Hf/^{177}Hf)_i$	ε_{Hf} (t)	±(1σ)	t_{DM} (Ga)	±(1σ)	t_{DM2} (Ga)	±(1σ)
VILE104	0.043039	0.001472	0.001880	0.000055	0.282508	0.000023	274.8	0.282499	-3.6	0.82	1.08	0.03	1.31	0.04
VILE103	0.019191	0.000948	0.000870	0.000040	0.282804	0.000022	15.6	0.282804	1.5	0.78	0.63	0.03	0.83	0.04
VILE1012	0.026603	0.001028	0.001300	0.000049	0.282855	0.000018	9.5	0.282855	3.1	0.62	0.57	0.03	0.74	0.03
VILE1022	0.024476	0.002380	0.001138	0.000106	0.282789	0.000024	163.8	0.282785	4.1	0.83	0.66	0.03	0.82	0.04
VILE1023	0.008596	0.000498	0.000389	0.000020	0.282824	0.000017	10.1	0.282824	2.0	0.60	0.60	0.02	0.80	0.03
VILE1031	0.066714	0.001788	0.002539	0.000058	0.282516	0.000030	273.4	0.282503	-3.5	1.06	1.09	0.04	1.31	0.06
VILE1053	0.031420	0.000944	0.001379	0.000040	0.282551	0.000030	275.8	0.282544	-2.0	1.04	1.00	0.04	1.23	0.06
VILE1059	0.026770	0.001146	0.001105	0.000047	0.282606	0.000024	249.8	0.282601	-0.6	0.84	0.92	0.03	1.13	0.04
VILE1071	0.014835	0.000250	0.000721	0.000012	0.282835	0.000023	11.3	0.282834	2.5	0.81	0.59	0.03	0.78	0.04
VILE1072	0.030846	0.000920	0.001400	0.000039	0.282502	0.000019	261.6	0.282495	-4.1	0.65	1.07	0.03	1.32	0.03
VILE1078	0.076871	0.001844	0.002932	0.000066	0.282378	0.000019	271.2	0.282363	-8.5	0.68	1.30	0.03	1.56	0.04
VILE1079	0.035296	0.001450	0.001432	0.000054	0.282650	0.000021	242.1	0.282644	0.8	0.74	0.86	0.03	1.05	0.04
VILE1082	0.020942	0.000862	0.000881	0.000030	0.282449	0.000023	311.5	0.282443	-4.8	0.81	1.13	0.03	1.40	0.04
VILE1088	0.011024	0.000187	0.000579	0.000007	0.282773	0.000018	6.4	0.282773	0.2	0.62	0.67	0.02	0.89	0.03
VILE1091	0.028833	0.000366	0.001340	0.000022	0.282892	0.000020	68.5	0.282890	5.7	0.69	0.52	0.03	0.65	0.04
VILE1094	0.057544	0.001324	0.002354	0.000049	0.282501	0.000015	227.1	0.282491	-4.9	0.52	1.10	0.02	1.34	0.03
VILE1096	0.028090	0.000838	0.001238	0.000036	0.282621	0.000026	232.7	0.282615	-0.4	0.90	0.90	0.04	1.11	0.05
VILE10109	0.023789	0.000922	0.001079	0.000044	0.282753	0.000021	149.3	0.282750	2.5	0.74	0.71	0.03	0.89	0.04
VILE10111	0.020754	0.000540	0.000878	0.000028	0.282365	0.000025	330.8	0.282360	-7.3	0.88	1.25	0.04	1.55	0.05
VILE10113	0.013312	0.000690	0.000596	0.000044	0.282738	0.000030	11.5	0.282738	-1.0	1.04	0.72	0.04	0.96	0.06
VILE10123	0.023247	0.000840	0.001110	0.000035	0.282439	0.000027	268.4	0.282433	-6.1	0.94	1.15	0.04	1.44	0.05
VILE10132	0.029549	0.000956	0.001184	0.000036	0.282322	0.000015	345.1	0.282314	-8.6	0.52	1.32	0.02	1.63	0.03
VILE10135	0.016720	0.000356	0.000760	0.000015	0.282633	0.000028	8.5	0.282633	-4.7	0.99	0.87	0.04	1.15	0.05
VILE10137	0.033118	0.001422	0.001408	0.000055	0.282321	0.000022	325.9	0.282313	-9.1	0.76	1.33	0.03	1.64	0.04
VILE10140	0.012447	0.000052	0.000517	0.000005	0.282598	0.000027	269.0	0.282595	-0.4	0.94	0.92	0.04	1.14	0.05
VILE105	0.018106	0.000416	0.000778	0.000015	0.282427	0.000024	291.0	0.282422	-6.0	0.85	1.16	0.03	1.45	0.05
VILE1017	0.038164	0.001976	0.001529	0.000079	0.282312	0.000022	339.9	0.282303	-9.1	0.76	1.35	0.03	1.65	0.04
VILE1150	0.001472	0.000065	0.036838	0.001594	0.282537	0.000025	241.9	0.282371	-8.9	0.86	20.16	0.58	1.56	0.05
VILE1160	0.000488	0.000050	0.010657	0.000176	0.282526	0.000029	265.7	0.282473	-4.8	1.00	1.38	0.05	1.36	0.05
VILE1169	0.001042	0.000005	0.020396	0.000113	0.282995	0.000035	44.5	0.282978	8.3	1.23	0.75	0.10	0.50	0.07
VILE1170	0.001097	0.000010	0.024561	0.000173	0.282406	0.000015	306.9	0.282265	-11.2	0.53	3.17	0.06	1.73	0.03
VILE1152	0.000531	0.000023	0.010942	0.000476	0.282801	0.000034	28.9	0.282796	1.5	1.18	0.87	0.06	0.84	0.06
VILE1183	0.000994	0.000015	0.023756	0.000322	0.282592	0.000019	293.2	0.282461	-4.5	0.65	2.36	0.06	1.38	0.03

VILE11		0.000		0.001		0.000								
107	0.001102	053	0.023052	230	0.282742	038	7.6	0.282739	-1.0	1.34	1.74	0.13	0.96	0.07
VILE11		0.000		0.000		0.000								
108	0.000610	030	0.013342	754	0.282837	031	8.0	0.282835	2.4	1.09	0.88	0.07	0.78	0.06
VILE11		0.000		0.000		0.000								
123	0.001007	022	0.023911	552	0.282606	033	262.4	0.282489	-4.3	1.15	2.33	0.12	1.33	0.06
VILE11		0.000		0.003		0.000			-					
124	0.000456	115	0.010853	040	0.282066	076	10.5	0.282064	24.8	2.65	2.26	0.14	2.19	0.14
VILE11		0.000		0.001		0.000								
130	0.000944	046	0.019698	094	0.282794	054	15.9	0.282788	0.9	1.89	1.29	0.15	0.86	0.10
VILE11		0.000		0.000		0.000			-					
132	0.001517	030	0.037378	770	0.282440	028	346.0	0.282198	12.7	0.98	31.29	0.81	1.84	0.05
VILE11		0.000		0.001		0.000						(0.2		
134	0.001951	055	0.044197	356	0.282802	029	19.9	0.282786	0.9	1.02	(4.31)	9)	0.87	0.05
VILE11		0.000		0.001		0.000								
117	0.001584	059	0.035332	440	0.282842	023	21.7	0.282828	2.5	0.81	6.69	0.35	0.79	0.04
VILE11		0.000		0.002		0.000								
105	0.001199	124	0.024210	020	0.282777	045	13.7	0.282771	0.3	1.58	1.76	0.16	0.89	0.08
VILE11		0.000		0.000		0.000								
80	0.000610	016	0.012337	336	0.282818	030	32.6	0.282810	2.1	1.06	0.88	0.06	0.81	0.06
VILE11		0.000		0.000		0.000								
41	0.000574	033	0.011497	620	0.282739	028	37.6	0.282730	-0.6	0.99	1.01	0.06	0.96	0.05
VILE11		0.000		0.000		0.000								
39	0.000835	006	0.019591	132	0.282479	031	309.3	0.282366	-7.6	1.07	2.15	0.08	1.55	0.06
VILE11		0.000		0.002		0.000								
31	0.000893	102	0.018900	140	0.282764	032	20.2	0.282757	-0.1	1.11	1.32	0.08	0.92	0.06
VILE11		0.000		0.000		0.000								
28	0.001099	009	0.021269	252	0.282807	030	15.5	0.282801	1.4	1.05	1.37	0.09	0.84	0.06
VN05		0.000		0.001		0.000								
21	0.001099	055	0.024624	286	0.282948	033	54.6	0.282923	6.5	1.14	1.16	0.12	0.60	0.06
VN05		0.000		0.000		0.000								
27	0.000910	031	0.020507	732	0.282859	023	62.5	0.282835	3.6	0.80	1.16	0.07	0.76	0.04
VN05		0.000		0.001		0.000						(0.1		
34	0.002200	033	0.053458	086	0.282605	026	226.6	0.282378	-9.0	0.91	(2.35)	0)	1.55	0.05
VN05		0.000		0.001		0.000								
41	0.001113	046	0.027092	288	0.282723	022	232.0	0.282606	-0.8	0.76	2.44	0.10	1.13	0.04
VN05		0.000		0.000		0.000								
45	0.000622	010	0.014054	338	0.282565	032	267.0	0.282495	-3.9	1.11	1.49	0.07	1.32	0.06
VN05		0.000		0.003		0.000			-			(0.0		
47	0.003122	111	0.083277	180	0.282557	043	232.7	0.282195	15.3	1.50	(0.83)	5)	1.89	0.08
VN05		0.000		0.003		0.000								
48	0.001621	116	0.038184	000	0.282722	092	220.0	0.282565	-2.5	3.22	66.21	6.25	1.21	0.17
VN05		0.000		0.000		0.000								
56	0.001232	024	0.028478	726	0.282646	106	341.5	0.282464	-3.4	3.71	3.17	0.54	1.35	0.20
VN05		0.000		0.000		0.000								
57	0.000879	038	0.019254	846	0.282954	028	157.9	0.282897	7.9	0.99	0.82	0.08	0.61	0.05
VN05		0.000		0.001		0.000								
58	0.000834	049	0.017506	122	0.282892	029	63.3	0.282871	4.9	1.00	0.91	0.07	0.69	0.05
VN05		0.000		0.001		0.000								
59	0.000980	056	0.021510	416	0.282569	030	257.9	0.282465	-5.2	1.06	2.12	0.09	1.38	0.06
VN05		0.000		0.000		0.000								
60	0.000615	018	0.015656	504	0.282432	023	303.9	0.282343	-8.5	0.81	1.90	0.05	1.59	0.04
VN05		0.000		0.000		0.000								
63	0.000714	038	0.015470	838	0.282520	020	249.6	0.282448	-6.0	0.71	1.68	0.05	1.42	0.04
VN05		0.000		0.003		0.000						(0.6		
65	0.001620	147	0.040919	740	0.282825	024	62.8	0.282777	1.6	0.84	(9.90)	2)	0.87	0.04
VN05		0.000		0.001		0.000						(0.8		
71	0.001671	044	0.040895	346	0.282551	030	347.9	0.282285	-9.6	1.04	(17.63)	9)	1.68	0.05
VN05		0.000		0.001		0.000								
79	0.000715	052	0.015372	092	0.282834	043	58.9	0.282818	2.9	1.50	0.96	0.10	0.79	0.08
VN05		0.000		0.001		0.000								
77	0.000455	047	0.009881	180	0.282599	031	251.4	0.282552	-2.3	1.10	1.21	0.06	1.22	0.06
VN05		0.000		0.000		0.000						(0.2		
80	0.001790	005	0.044019	165	0.282577	026	317.0	0.282316	-9.2	0.92	(6.84)	9)	1.64	0.05
VN05		0.000		0.000		0.000								
84	0.000544	007	0.011296	156	0.282806	032	65.3	0.282793	2.2	1.13	0.87	0.06	0.84	0.06
VN05		0.000		0.000		0.000						(0.1		
85	0.002170	027	0.054925	660	0.282795	044	254.0	0.282534	-2.8	1.54	(1.50)	5)	1.25	0.08
VN05		0.000		0.000		0.000								
86	0.000499	007	0.011657	153	0.282523	024	300.0	0.282458	-4.5	0.85	1.44	0.05	1.38	0.04
VN05		0.000		0.000		0.000								
90	0.000838	022	0.018460	542	0.282804	043	63.9	0.282782	1.8	1.50	1.19	0.11	0.86	0.08
VN05		0.000		0.000		0.000								
128	0.000436	016	0.008595	338	0.282884	031	35.5	0.282879	4.6	1.08	0.65	0.05	0.69	0.06
VN05		0.000		0.000		0.000								
130	0.000626	011	0.014252	184	0.282683	082	233.9	0.282621	-0.2	2.88	1.24	0.18	1.10	0.15
VN05		0.000		0.000		0.000								
20	0.000485	001	0.011145	015	0.282821	025	15.0	0.282818	2.0	0.88	0.84	0.05	0.81	0.05
VN05		0.000		0.000		0.000								
35	0.000379	016	0.008178	348	0.282727	030	15.5	0.282725	-1.3	1.04	0.92	0.05	0.98	0.05

VN05		0.000		0.000		0.000								
19	0.000658	011	0.013483	238	0.282815	023	23.1	0.282809	1.8	0.81	0.93	0.05	0.82	0.04
VN05		0.000		0.000		0.000								
44	0.000464	002	0.010817	048	0.282790	016	16.3	0.282787	0.9	0.57	0.89	0.03	0.86	0.03
VN05		0.000		0.000		0.000								
110	0.000812	010	0.018199	228	0.282837	022	16.7	0.282831	2.5	0.78	1.08	0.06	0.78	0.04
		0.000		0.007		0.000								
TAL06 6	0.001152	368	0.023112	380	0.282947	041	55.6	0.282923	6.6	1.43	1.05	0.14	0.60	0.08
TAL06		0.000		0.000		0.000								
60	0.001095	041	0.025164	570	0.282516	018	40.0	0.282497	-8.8	0.62	2.89	0.07	1.39	0.03
TAL06m		0.000		0.002		0.000								
2 14	0.001312	119	0.028904	720	0.282773	037	208.3	0.282661	0.6	1.28	2.63	0.20	1.03	0.07
TAL06m		0.000		0.001		0.000								
2 29	0.001336	080	0.028499	810	0.282913	027	153.2	0.282832	5.5	0.93	1.79	0.14	0.73	0.05
TAL06m		0.000		0.000		0.000								
2 32	0.001764	010	0.041137	834	0.282659	026	221.0	0.282489	-5.2	0.91	(13.04)	(0.65)	1.35	0.05
TAL06m		0.000		0.000		0.000								
2 35	0.000964	020	0.019798	376	0.282916	024	42.9	0.282900	5.5	0.85	0.95	0.07	0.64	0.05
TAL06m		0.000		0.001		0.000								
2 41	0.001920	061	0.038840	392	0.282918	024	66.6	0.282869	4.9	0.85	(75.56)	(13.81)	0.69	0.05
TAL06m		0.000		0.001		0.000								
2 56	0.001241	045	0.025991	028	0.282899	025	140.5	0.282831	5.2	0.88	1.49	0.11	0.74	0.05
TAL06m		0.000		0.000		0.000								
2 65	0.001043	026	0.021869	538	0.282972	031	42.2	0.282955	7.4	1.10	0.89	0.10	0.54	0.06
TAL16		0.000		0.000		0.000								
31	0.000709	022	0.015034	448	0.282808	032	66.5	0.282789	2.1	1.13	1.01	0.07	0.84	0.06
TAL16		0.000		0.000		0.000								
104	0.000546	034	0.011368	714	0.282806	026	185.1	0.282767	3.9	0.90	0.87	0.05	0.85	0.05
TAL14		0.000		0.000		0.000								
32	0.000842	030	0.016049	608	0.282788	032	27.2	0.282779	0.9	1.13	1.10	0.08	0.87	0.06
TAL14		0.000		0.000		0.000			-0.4					
42	0.000382	005	0.007352	212	0.281651	028	182.6	0.281626	36.6	0.98	2.69	0.05	2.93	0.05
TAL14		0.000		0.000		0.000								
48	0.001308	034	0.027204	742	0.282756	040	75.9	0.282717	-0.3	1.39	2.32	0.18	0.97	0.07
TAL14		0.000		0.001		0.000								
50	0.001405	047	0.032321	188	0.282745	025	52.4	0.282713	-0.9	0.87	4.28	0.20	0.99	0.05
TAL14		0.000		0.000		0.000			-0.4					
72	0.000523	017	0.012321	396	0.282021	019	51.5	0.282009	25.8	0.67	2.47	0.04	2.28	0.03
TAL09		0.000		0.001		0.000								
23	0.000726	047	0.015956	242	0.282768	027	42.3	0.282756	0.4	0.93	1.14	0.06	0.91	0.05
TAL09		0.000		0.000		0.000						(0.10)		
40	0.002454	019	0.058810	542	0.282742	036	82.0	0.282652	-2.5	1.27	(1.35)		1.09	0.07
TAL09		0.000		0.000		0.000								
90	0.000534	009	0.012187	176	0.282846	033	217.7	0.282797	5.6	1.14	0.82	0.07	0.78	0.06
AMP03		0.000		0.000		0.000								
119	0.000997	016	0.019407	480	0.282787	022	4.2	0.282786	0.6	0.78	1.29	0.06	0.87	0.04
AMP03		0.000		0.000		0.000								
62	0.000656	023	0.013931	468	0.282816	017	8.6	0.282814	1.7	0.58	0.94	0.04	0.82	0.03
AMP03		0.000		0.003		0.000								
114	0.000976	177	0.018754	000	0.282776	023	10.5	0.282772	0.2	0.81	1.28	0.06	0.89	0.04
TAL09		0.000		0.001		0.000								
107	0.000919	055	0.021274	342	0.282531	022	85.1	0.282497	-7.9	0.77	2.21	0.07	1.38	0.04
MGN04		0.000		0.000		0.000								
1	0.000520	020	0.011230	360	0.282694	021	14.9	0.282691	-2.5	0.75	1.09	0.04	1.04	0.04
MGN04		0.000		0.000		0.000								
7	0.000677	018	0.014740	476	0.282641	026	20.4	0.282635	-4.4	0.92	1.36	0.06	1.14	0.05
MGN04		0.000		0.000		0.000								
19	0.000758	006	0.017406	173	0.282678	023	13.8	0.282673	-3.2	0.81	1.44	0.06	1.08	0.04
MGN04		0.000		0.000		0.000								
36	0.000576	008	0.013135	170	0.282681	036	15.6	0.282677	-3.0	1.27	1.19	0.08	1.07	0.07
MGN04		0.000		0.002		0.000								
37	0.001314	105	0.029924	580	0.282829	031	21.7	0.282817	2.1	1.07	2.60	0.18	0.81	0.06
MGN04		0.000		0.001		0.000								
38	0.000596	044	0.013479	032	0.282670	021	15.7	0.282666	-3.4	0.74	1.23	0.04	1.09	0.04
MGN04		0.000		0.001		0.000						(0.24)		
40	0.001908	059	0.043258	288	0.282830	020	24.5	0.282810	1.9	0.69	(4.85)		0.82	0.04
MGN04		0.000		0.000		0.000								
44	0.001129	029	0.024200	624	0.282850	023	39.9	0.282832	3.0	0.82	1.49	0.09	0.77	0.04
MGN04		0.002		0.000		0.000								
51	0.033913	646	0.001437	104	0.282757	049	15.9	0.282756	-0.2	1.72	0.71	0.07	0.92	0.09
MGN04		0.000		0.000		0.000								
58	0.000751	030	0.016143	698	0.282668	016	9.6	0.282665	-3.6	0.56	1.38	0.04	1.09	0.03
MGN04		0.000		0.000		0.000								
62	0.000703	014	0.015858	400	0.282725	038	12.8	0.282721	-1.5	1.33	1.23	0.09	0.99	0.07
MGN04		0.000		0.000		0.000								
63	0.001027	021	0.020473	464	0.282769	028	5.4	0.282767	-0.1	0.99	1.42	0.08	0.91	0.05
MGN04		0.000		0.000		0.000								
72	0.000838	016	0.016623	336	0.282813	029	38.7	0.282801	1.9	1.02	1.06	0.07	0.83	0.05
MGN04		0.000		0.000		0.000								
73	0.001005	032	0.022546	776	0.282643	026	9.9	0.282638	-4.5	0.90	2.02	0.08	1.14	0.05

MGN04		0.000		0.002		0.000								
80	0.001207	087	0.029135	200	0.282824	018	86.1	0.282777	2.1	0.64	2.41	0.10	0.86	0.03
MGN04		0.000		0.000		0.000								
91	0.000697	036	0.013826	740	0.282824	022	37.9	0.282814	2.3	0.76	0.92	0.05	0.81	0.04
MGN04		0.000		0.000		0.000								
96	0.001412	038	0.030967	836	0.282849	021	24.3	0.282835	2.8	0.75	2.81	0.15	0.77	0.04
MGN04		0.000		0.004		0.000						(0.2		
97	0.001734	123	0.044742	280	0.282645	023	24.7	0.282625	-4.7	0.81	(5.37)	2)	1.16	0.04
MGN04		0.000		0.000		0.000								
108	0.000674	007	0.013640	170	0.282764	020	30.4	0.282756	0.1	0.71	1.04	0.04	0.92	0.04
MGN04		0.000		0.001		0.000								
109	0.001023	064	0.020834	318	0.282861	030	28.7	0.282850	3.4	1.04	1.18	0.09	0.74	0.06
MGN04		0.000		0.000		0.000								
113	0.000645	008	0.012145	169	0.282866	027	36.2	0.282858	3.8	0.93	0.78	0.05	0.72	0.05
MGN04		0.000		0.000		0.000								
121	0.001029	006	0.021089	224	0.282837	022	41.3	0.282821	2.6	0.76	1.26	0.07	0.79	0.04
MGN04		0.000		0.000		0.000								
125	0.000359	005	0.006851	061	0.282824	020	37.4	0.282819	2.5	0.70	0.72	0.03	0.80	0.04
RAG01_		0.000		0.000		0.000			-					
1	0.282152	012	0.000554	016	0.011350	096	503.5	0.282147	11.0	0.42	1.53	0.02	1.89	0.02
RAG01_		0.000		0.000		0.000								
10	0.282360	010	0.000626	005	0.014072	111	498	0.282354	-3.8	0.34	1.25	0.01	1.51	0.02
RAG01_		0.000		0.000		0.000								
2	0.282279	013	0.000629	009	0.014777	167	522.5	0.282273	-6.2	0.46	1.36	0.02	1.65	0.02
RAG01_		0.000		0.000		0.000			-					
21	0.282291	012	0.000886	029	0.022530	709	275.9	0.282286	11.1	0.41	1.35	0.02	1.70	0.02
RAG01_		0.000		0.000		0.000								
23	0.282341	014	0.000738	021	0.017116	529	290.6	0.282337	-9.0	0.49	1.28	0.02	1.61	0.03
RAG01_		0.000		0.000		0.000								
24	0.282528	014	0.001032	028	0.025111	675	488.9	0.282518	1.8	0.48	1.03	0.02	1.20	0.03
RAG01_		0.000		0.000		0.000								
26	0.282514	014	0.001054	008	0.026120	253	510.8	0.282504	1.8	0.50	1.05	0.02	1.22	0.03
RAG01_		0.000		0.000		0.000								
30	0.282323	013	0.001139	022	0.026180	463	477	0.282313	-5.8	0.44	1.32	0.02	1.59	0.02
RAG01_		0.000		0.000		0.000								
31	0.282309	013	0.001250	022	0.029179	596	545.9	0.282297	-4.8	0.45	1.34	0.02	1.60	0.02
RAG01_		0.000		0.000		0.001			-					
33	0.282179	015	0.001134	052	0.029041	510	276.7	0.282173	15.1	0.53	1.52	0.02	1.91	0.03
RAG01_		0.000		0.000		0.000								
35	0.282356	015	0.000135	013	0.003854	333	275.5	0.282355	-8.7	0.51	1.24	0.02	1.58	0.03
RAG01_		0.000		0.000		0.001			-					
41	0.280888	018	0.000869	048	0.021287	280	277.4	0.280884	60.7	0.63	3.27	0.02	4.22	0.03
RAG01_		0.000		0.000		0.000			-					
5	0.282269	007	0.000434	013	0.010210	319	280	0.282266	11.7	0.25	1.37	0.01	1.74	0.01
RAG01_		0.000		0.000		0.000								
53	0.282519	022	0.000222	007	0.005071	166	517	0.282517	2.3	0.76	1.02	0.03	1.20	0.04
RAG01_		0.000		0.000		0.000								
6	0.282561	011	0.000885	011	0.020273	311	467.8	0.282553	2.6	0.37	0.98	0.01	1.15	0.02
RAG01_		0.000		0.000		0.000			-					
8	0.282299	014	0.001532	025	0.038363	668	275.9	0.282291	11.0	0.50	1.37	0.02	1.70	0.03
RAG01_		0.000		0.000		0.000								
9	0.282531	012	0.000736	032	0.017595	847	469.5	0.282525	1.6	0.42	1.01	0.02	1.20	0.02
RSJc01_		0.000		0.000		0.000								
12	0.282513	013	0.000953	015	0.022558	373	346.9	0.282507	-1.8	0.46	1.04	0.02	1.27	0.02
RSJc01_		0.000		0.000		0.000								
15	0.282200	010	0.000036	003	0.000952	070	529.9	0.282200	-8.6	0.34	1.45	0.01	1.78	0.02
RSJc01_		0.000		0.000		0.000								
17	0.282283	013	0.001359	007	0.030895	155	464.8	0.282271	-7.5	0.46	1.38	0.02	1.67	0.02
RSJc01_		0.000		0.000		0.000								
18	0.282377	016	0.001301	017	0.029413	370	479.3	0.282366	-3.8	0.55	1.25	0.02	1.49	0.03
RSJc01_		0.000		0.000		0.000								
3	0.282374	012	0.000915	004	0.019226	057	482.3	0.282365	-3.8	0.41	1.24	0.02	1.49	0.02
RSJc01_		0.000		0.000		0.001								
35	0.282581	012	0.001215	058	0.030392	500	277.8	0.282575	-0.9	0.42	0.96	0.02	1.17	0.02
RSJc01_		0.000		0.000		0.000								
41	0.282525	012	0.001164	033	0.028182	839	341.6	0.282517	-1.5	0.41	1.03	0.02	1.26	0.02
RSJc01_		0.000		0.000		0.000								
43	0.282374	009	0.002762	026	0.069088	442	482.8	0.282349	-4.3	0.33	1.30	0.01	1.52	0.02
RSJc01_		0.000		0.000		0.001								
44	0.282633	012	0.001924	058	0.044614	340	247.8	0.282624	0.2	0.42	0.90	0.02	1.09	0.02
RSJc01_		0.000		0.000		0.000								
49	0.282934	011	0.001304	026	0.031401	629	151.9	0.282931	8.9	0.37	0.45	0.02	0.55	0.02
RSJc01_		0.000		0.000		0.000								
60	0.282585	012	0.000915	020	0.022606	488	303.4	0.282580	-0.1	0.41	0.94	0.02	1.15	0.02
RSJc01_		0.000		0.000		0.001								
65	0.282276	017	0.001292	070	0.030977	580	541.8	0.282263	-6.1	0.59	1.39	0.02	1.66	0.03
RSJc01_		0.000		0.000		0.000			-					
7	0.282107	016	0.000499	004	0.012122	133	529.7	0.282102	12.1	0.55	1.59	0.02	1.96	0.03
RSJc01_		0.000		0.000		0.000			-					
9	0.282304	012	0.001066	051	0.025901	996	283.8	0.282299	10.5	0.42	1.34	0.02	1.68	0.02

		0.000		0.000		0.000			-					
ST02-12	0.282073	013	0.001031	015	0.021718	339	483.7	0.282064	14.4	0.47	1.66	0.02	2.04	0.02
		0.000		0.000		0.000			-					
ST02-13	0.282067	013	0.000976	026	0.019949	523	487.2	0.282058	14.5	0.44	1.67	0.02	2.05	0.02
		0.000		0.000		0.000								
ST02-14	0.282322	013	0.000897	028	0.019218	667	488.6	0.282314	-5.5	0.47	1.31	0.02	1.58	0.02
		0.000		0.000		0.000								
ST02-20	0.282294	019	0.001288	031	0.028192	694	497.9	0.282282	-6.4	0.65	1.36	0.03	1.64	0.03
		0.000		0.000		0.000								
ST02-21	0.282418	015	0.001040	008	0.021443	306	473.4	0.282409	-2.4	0.52	1.18	0.02	1.41	0.03
		0.000		0.000		0.001								
ST02-22	0.282294	015	0.001229	077	0.024679	430	482.9	0.282282	-6.7	0.53	1.36	0.02	1.64	0.03
		0.000		0.000		0.000			-					
ST02-28	0.282105	020	0.000683	005	0.014764	075	497.1	0.282099	12.9	0.69	1.60	0.03	1.98	0.04
		0.000		0.000		0.000			-					
ST02-29	0.282114	016	0.000852	011	0.017588	214	479.6	0.282106	13.0	0.56	1.60	0.02	1.97	0.03
		0.000		0.000		0.000								
ST02-31	0.282279	012	0.001089	016	0.022494	369	516.2	0.282269	-6.4	0.41	1.38	0.02	1.66	0.02
		0.000		0.000		0.000			-					
ST02-39	0.282144	012	0.001206	016	0.025603	410	491.5	0.282133	11.8	0.43	1.57	0.02	1.91	0.02

APPENDIX 1.2: BEDROCK AGE AND LOCATION DATA

See supplementary file

APPENDIX 1.3: DETRITAL ZIRCON U-TH-PB DATA

See supplementary file

APPENDIX 2.1: PALEOCURRENT MEASUREMENTS

Calingasta Hinterland Basin: Villa Nueva section paleoflow measurements

Station	VNPF01	VNPF02	VNPF03	VNPF04	VNPF05	VNPF06	VNPF07
Stratigraphic Height (m)	203.5	214	370	718.5	930	1391	1574
Sedimentary strucutre	imbricated clast	imbricated clast	imbricated clast	imbricated clast	imbricated clast	imbricated clast	imbricated clast
Flow Trend (°) rotated for bedding dip	175	74	161	203	255	232	282
	210	154	159	117	284	144	335
	195	100	155	175	280	146	210
	205	72	173	250	193	129	274
	243	125	174	231	129	111	320
	227	74	166	130	234	167	276
	212	150	172	141	261	203	293
	243	233	145	112	216	160	343
	223	164	183	111	258	168	254
	234	129	147	134	122	163	259
	215	121	150	153	156	128	325
	205	146	168	337	151	140	304
	200	179	155	14	154	109	230
	186	126	169	360	130	96	353
	185	119	196	14	222	164	293
	144	130	179	127	234	187	289
	200	151	162	231	231	161	282
	86	116	195	152	177	269	328
	175	160	263	252	210	283	275
	170	126	159	198	269	223	285
	151	129	149		270	275	323
	143	154	163		265	284	
	176	280	172		254	289	
	201	207	163		292	226	
		88	157		258	264	
					241		

Precordillera Wedgetop Basin: Talacasto section paleoflow measurements

Station	TALPF01	TALPF03	TALPF02
Stratigraphic Height (m)	25	300	510
Sedimentary strucutre	Tablular Cross-strata	Tablular Cross-strata	Trough cross-strata
Flow Trend (°) rotated for bedding dip	62	218	79
	338	36	61
	36	351	39
	13	340	137
	333	97	193
	355	213	161
	325	242	165
	315	267	101
	343	125	103
	352	297	95
	325	358	58
	333	2	248
	297	48	87
	315	54	108
	25	345	98
		351	
		319	
		310	
		337	
		15	

Bermejo Foreland Basin: Mogna section paleoflow measurements

Station	MGNPF01	MGNPF02	MGNPF03	MGNPF07	MGNPF06	MGNPF05	MGNPF04
Stratigraphic Height (m)	10	170	800	1350	2350	3300	3820
Sedimentary strucutre	imbricated clast	Trough cross-strata	Trough cross-strata	Trough cross-strata	Trough cross-strata	imbricated clast	imbricated clast
Flow Trend (°) rotated for bedding dip	317	123	235	50	282	40	58
	323	122	237	347	244	50	54
	332	112	290	213	204	128	212
	349	70	285	329	339	90	154

284	75	347	20	348	80	137
269	189	324	31	338	81	115
327	188	190	311	236	111	166
272	33	174	54	351	118	158
334	329	238	57	224	83	140
314	37	247	185	232	100	140
330	8	222	122	343	68	99
321	123	258	357	229	81	107
143	46	204	359	258	81	149
155		205	69	199	78	139
333		115	191	276	49	45
143						
299						
294						
297						
277						
310						
313						

Broken Foreland Basin: Sierra Pie de Palo North section paleoflow measurements

Station	AMPPF01	AMPPF03	AMPPF02	AMPPF04
Stratigraphic Height (m)	98	158	283	439
Sedimentary strucutre	Tablular Cross-strata	imbricated clast	imbricatedclast	imbricatedclast
Flow Trend (°) rotated for bedding dip	262.9	12.7	25.2	158
	207.6	34.3	118.5	184
	129.6	338	127.1	169
	263.3	336	38	177
	263.3	324.9	102.4	155
	156.1	1.7	41.6	145
	153.1	353.3	55.9	125
	174.4	31.7	77.8	123
	199.2	345.2	76.3	131
	188.3	345.9	77.5	140
	129.7	5	63.9	142
	134.6	350.3	49.3	189
	169.5	30.7	82.3	177
	167.1	349.6	103.3	184
	170.1	35.5	53.1	176
		18.7	145.7	182

30.5	111.2	181
0.2	103.7	143
355.3	66.7	134
224.6	49.1	169
290.1	89.1	115
332.8	72.8	141
326.1	69.1	149
352.9	110	
351.9		
344.4		
15.6		
12.5		
57.7		
321.1		
10		

APPENDIX 2.2: Ar^{40}/Ar^{39} GEOCHRONOLOGY

VN03-031714, Groundmass,

7.19 mg, J=0.0018729±0.02%, IC=0.9905236±0.0007112, NM-288A, Lab#=65422-01, Helix MC

	ID	Power (Watts)	40Ar/39Ar	37Ar/39Ar	36Ar/39Ar (x 10-3)	39ArK (x 10-15 mol)	K/Ca	40Ar* (%)	39Ar (%)	Age (Ma)	±1s (Ma)
X	A	0.5	100.890	2.046	300.922	1.092	0.249	12.017	1.187	41.2	0.9
X	B	0.8	14.748	1.337	21.060	6.800	0.382	58.498	8.579	29.4	0.1
X	C	1.3	9.382	1.063	4.379	14.992	0.480	87.092	24.876	27.8	0.0
X	D	1.6	8.639	1.069	2.097	10.304	0.477	93.797	36.077	27.6	0.0
X	E	1.9	8.400	1.109	1.466	8.607	0.460	95.879	45.433	27.4	0.1
Xi	F	2.2	8.308	1.245	1.265	7.436	0.410	96.678	53.516	27.3	0.1
i	G	3	8.278	3.569	2.044	11.119	0.143	96.086	65.602	27.1	0.0
i	H	5	8.319	8.383	3.726	17.411	0.061	94.665	84.529	26.9	0.0
i	I	6	8.240	6.355	2.751	4.984	0.080	96.183	89.947	27.1	0.1
i	J	7	8.261	6.617	2.668	2.038	0.077	96.739	92.162	27.3	0.2
i	K	8.5	8.360	7.070	2.823	4.292	0.072	96.651	96.828	27.6	0.1
i	L	10	8.445	7.007	2.945	1.401	0.073	96.199	98.351	27.8	0.3
i	M	15	8.229	6.873	2.915	1.517	0.074	96.080	100.000	27.0	0.3
	Integrated age ± 1s			n=13		91.99123	0.14		K2O=2.62 %	27.7	0.0
	Plateau ± 1s	steps G-M		n=7	MSWD=9.32	42.76126			46.48406	27.0	0.1
	Isochron±1s	steps A-E		n=5	MSWD=22.85		40Ar/36Ar =	312.2±0.8		27.5	0.0

Notes:

Isotopic ratios corrected for blank, radioactive decay, and mass discrimination, not corrected for interfering reactions.

Errors quoted for individual analyses include analytical error only, without interfering reaction or J uncertainties.

Integrated age calculated by summing isotopic measurements of all steps.

Integrated age error calculated by quadratically combining errors of isotopic measurements of all steps.

Plateau age is inverse-variance-weighted mean of selected steps.

Plateau age error is inverse-variance-weighted mean error (Taylor, 1982) times root MSWD where MSWD>1.

Plateau error is weighted error of Taylor (1982).
Iisotopic abundances after Steiger and Jäger (1977).
X preceding sample ID denotes analyses excluded from plateau age calculations.
i preceding sample ID denotes analyses excluded from isochron age calculations.

Isochron age and intercept given by York (1969)

Weight percent K_2O calculated from ^{39}Ar signal, sample weight, and instrument sensitivity.

Ages calculated relative to FC-2 Fish Canyon Tuff sanidine standard at 28.201 Ma (Kuiper et al., 2008)
Decay Constant (LambdaK (total)) = 5.463e-10/a (Min et al., 2000)

Correction factors:	NM-289	NM-288
	$(^{39}Ar/^{37}Ar)_{Ca}$ = 0.0006756 ± 0.000001	$(^{39}Ar/^{37}Ar)_{Ca}$ = 0.0006752 ± 0.000002
	$(^{36}Ar/^{37}Ar)_{Ca}$ = 0.000266 ± 0.0000003	$(^{36}Ar/^{37}Ar)_{Ca}$ = 0.0002653 ± 0.0000003
	$(^{40}Ar/^{39}Ar)_{K}$ = 0.00812 ± 0.0001	$(^{40}Ar/^{39}Ar)_{K}$ = 0.00697 ± 0.0004

APPENDIX 2.3: DETRITAL ZIRCON U-PB DATA

See supplementary file

APPENDIX 2.4: DETRITAL ZIRCON MAXIMUM DEPOSITIONAL AGES

	youngest single grain (YSG)			Youngest three zircons (Y3Z)			Youngest grain cluster at 2σ (YGC 2σ)		
sample	age	error	% disc	age	error	% disc	age	error	% disc
VNS02	**50.2**	**1.8**	**6.7**	50.2	1.8	6.7	50.2	1.8	6.7
				52	1.3	5.1	52	1.3	5.1
				57.4	2.7	8.6			
				52.2	**6.7**		**51.4**	**1.1**	
VN02	**17.4**	**1.3**	**21.3**	17.4	1.3	21.3	17.4	1.3	21.3
				18	1.5	5.9	18	1.5	5.9
				18	1	13.5	18	1	13.5
							18.1	1.3	17.7
							18.2	1.1	7.6
							18.2	1.2	20.9
							18.3	1.1	8.5
							18.5	2.1	23.6
							18.62	0.89	24.9
							18.7	1.1	15.8
				17.8	**0.7**		**18.2**	**0.4**	
VN04	**15.3**	**1.2**	**6.7**	15.3	1.2	6.7	15.3	1.2	6.7
				15.49	0.93	4.4	15.49	0.93	4.4
				15.65	0.67	14.0	15.65	0.67	14.0
							16.1	1.1	12.0
							16.4	1.3	22.6
				15.6	**0.5**		**15.7**	**0.4**	
VN05	**14.3**	**1.5**	**23.1**	14.3	1.5	23.1	14.3	1.5	23.1
				14.73	0.9	26.0	14.73	0.9	26.0
				15.1	1	26.0	15.1	1	26.0
							15.2	1.3	10.1
							15.62	0.93	9.2
				14.8	**0.6**		**15.1**	**0.5**	
VN06	**11.8**	**1.6**	**3.3**	11.8	1.6	3.3	11.8	1.6	3.3
				13.0	1.6	42.2	13.0	1.6	42.2
				13.1	1.4	26.8	13.1	1.4	26.8
							13.7	1.0	38.0
							13.9	2.1	23.6
				12.7	**0.9**		**13.2**	**0.6**	
VN01	**7.96**	**0.83**	**20.4**	7.96	0.83	20.4	7.96	0.83	20.4
				8.1	1	45.3	8.1	1	45.3
				8.4	1.5	16.7	8.4	1.5	16.7
							8.5	0.68	22.0

							8.5	2.1	72.3
							8.9	1	66.2
				8.1	**0.6**		**8.4**	**0.4**	
VN07	**6.7**	**1.3**	**40.2**	6.7	1.3	40.2	6.7	1.3	40.2
				7.6	1.2	20.8	7.6	1.2	20.8
				8.1	1.6	19.0			
				7.4	**0.8**		**7.2**	**0.9**	
TAL13	**17.43**	**0.58**	**1.0**	17.4	0.6	1.0	17.4	0.6	1.0
				17.9	0.7	13.4	17.9	0.7	13.4
				19.0	0.4	2.1			
				18.4	**2.1**		**17.6**	**0.4**	
MGN09	**10.45**	**0.7**	**10.7**	10.5	0.7	10.7	10.5	0.7	10.7
				11.0	0.7	28.6	11.0	0.7	28.6
				12.1	0.9	0.2			
				11.0	**1.9**		**10.7**	**0.5**	
MGN10	**11.2**	**1.1**	**44.8**	11.2	1.1	44.8	11.2	1.1	44.8
				11.4	0.6	18.3	11.4	0.6	18.3
				12.6	0.4	22.0			
				12.2	**1.9**		**11.3**	**0.6**	
MGN01	**7.3**	**0.8**	**27.9**	7.3	0.8	27.9	7.3	0.8	27.9
				7.5	1.4	32.4	7.5	1.4	32.4
				7.5	1.3	13.8	7.5	1.3	13.8
							7.7	1.2	31.3
							7.9	1.3	37.3
							8.0	0.9	46.9
							8.1	1.1	20.9
							8.1	1.0	47.4
							8.1	1.1	23.6
				7.4	**0.6**		**7.8**	**0.4**	
MGN02	**8.19**	**0.65**	**36.5**	8.2	0.7	36.5	8.2	0.7	36.5
				8.3	0.5	30.8	8.3	0.5	30.8
				8.7	0.7	37.0	8.7	0.7	37.0
				8.4	**0.3**		**8.4**	**0.3**	
MGN03	**7.5**	**0.4**	**7.7**	7.5	0.4	7.7	7.5	0.4	7.7
				8.3	0.8	33.2			
				9.0	0.9	10.3			
				7.9	**1.7**		**7.5**	**0.4**	
MGN04	**5.41**	**0.21**	**3.4**	5.4	0.2	3.4	5.4	0.2	3.4
				9.2	0.7	7.9			
				9.6	0.7	12.1			
				6.1	**4.6**		**5.4**	**0.2**	
MGN05	**1.23**	**0.19**	**48.1**	1.2	0.2	48.1	1.2	0.2	48.1
				1.4	0.2	38.5	1.4	0.2	38.5
				1.6	0.3	7.1	1.6	0.3	7.1
				1.4	**0.1**		**1.4**	**0.1**	

AMP01	**17.3**	**1.3**	**13.5**	17.3	1.3	13.5	17.3	1.3	13.5
				18.3	0.6	2.3	18.3	0.6	2.3
				170.8	2.2	1.9			
				27.0	**110.0**		**18.1**	**0.6**	
AMP02	**11.7**	**1.1**	**12.7**	11.7	1.1	12.7	11.7	1.1	12.7
				11.9	0.7	5.2	11.9	0.7	5.2
				12.8	1.0	1.6	12.8	1.0	1.6
				12.1	**0.5**		**12.1**	**0.5**	
AMP03	**4.2**	**0.3**	**3.9**	4.2	0.3	3.9	4.2	0.3	3.9
				8.1	0.5	20.2			
				8.4	1.1	28.2			
				5.6	**5.8**		**4.2**	**0.3**	

APPENDIX 3.1: DETRITAL ZIRCON U-PB DATA

See supplementary file

APPENDIX 3.2: RIVER PROVENANCE DATA

See supplementary file

REFERENCES

Alasino, Pablo H., Juan A. Dahlquist, Robert J. Pankhurst, Carmen Galindo, César Casquet, Carlos W. Rapela, M. A. Larrovere, and C. M. Fanning. "Early Carboniferous sub-to mid-alkaline magmatism in the Eastern Sierras Pampeanas, NW Argentina: A record of crustal growth by the incorporation of mantle-derived material in an extensional setting." Gondwana Research 22, no. 3-4 (2012): 992-1008.

Allmendinger, R.W., and Judge, P.A., 2014, the Argentine Precordillera: A foreland thrust belt proximal to the subducted plate: Geosphere, v. 10, p. 1203-1218.

Allmendinger, R.W., Figueroa, D., Snyder, D., Beer, J., Mpodozis, C. and Isacks, B.L., 1990. Foreland shortening and crustal balancing in the Andes at 30 S latitude. Tectonics, 9(4), pp.789-809.

Amidon, W.H., Burbank, D.W., and Gehrels, G.E., 2005a, Construction of detrital mineral populations: insights from mixing of U-Pb zircon ages in Himalayan rivers: Basin Research, v. 17, p. 463-485.

Amidon, W.H., Burbank, D.W., and Gehrels, G.E., 2005b, U-Pb zircon ages as a sediment mixing tracer in the Nepal Himalaya: Earth and Planetary Science Letters, v. 235, p. 244-260.

Anderson, R.B., Long, S.P., Horton, B.K., Thomson, S.N., Calle, A.Z. and Stockli, D.F., 2018. Orogenic wedge evolution of the central Andes, Bolivia (21 S): Implications for Cordilleran cyclicity. Tectonics, 37(10), pp.3577-3609.

Bahlburg, H., Vervoort, J. D., Du Frane, S. A., Bock, B., Augustsson, C., and Reimann, C., 2009, Timing of crust formation and recycling in accretionary orogens: Insights learned from the western margin of South America: Earth-Science Reviews, v. 97(1–4), 215–241. http://doi.org/10.1016/j.earscirev.2009.10.006

Balgord, E.A., 2017, Triassic to Neogene evolution of the south-central Andean arc determined by detrital zircon U-Pb and Hf analysis of Neuquen Basin strata, central Argentina (34 S – 40 S): Lithosphere, v. 9, p. 453-462, doi:10.1130/L546.1.

Beer, J.A., 1990, Steady sedimentation and lithologic completeness, Bermejo Basin, Argentina: Journal of Geology, v.98, p.501-517.

Beer, J.A., Allmendinger, R.W., Figueroa, D.E., and Jordan, T.E., 1990, Seismic stratigraphy of a Neogene piggyback basin, Argentina: American Association of Petroleum Geologists Bulletin, v. 74, p. 1183-1202.

Belousova, E., Griffin, W.L., O'Reilly, S.Y. and Fisher, N.L., 2002. Igneous zircon: trace element composition as an indicator of source rock type. Contributions to mineralogy and petrology, 143(5), pp.602-622.

Belousova, E.A., Kostitsyn, Y.A., Griffin, W.L., Begg, G.C., O'Reilly, S.Y. and Pearson, N.J., 2010. The growth of the continental crust: constraints from zircon Hf-isotope data. Lithos, 119(3-4), pp.457-466.

Cahill, T. and B.L. Isacks (1992), Seismicity and shape of the subducted Nazca Plate, J.Geophys. Res., 97(B12), 17,503-17,529.

Capaldi, T.N., Horton, B.K., McKenzie, N.R., Stockli, D.F., Odlum, M.L., 2017, Sediment provenance in contractional orogens: The detrital zircon record from modern rivers

in the Andean fold-thrust belt and foreland basin of western Argentina: Earth and Planetary Sciences Letters, v. 479, p. 83-97, doi: 10.1016/j.epsl.2017.09.001.

Cardozo, N. and Jordan, T., 2001, Causes of spatially variable tectonic subsidence in the Miocene Bermejo foreland basin, Argentina, Basin Research, v. 13, p.335-357.

Casquet, C., Baldo, E., Pankhurst, R.J., Rapela, C.W., Galindo, C., Fanning, C.M., Saaverdra, J., 2001, Involvement of the Argentine Precordillera terrane in the Famatinian mobile belt: U-Pb SHRIMP and metamorphic evidence from the Sierra de Pie de Palo: Geology, v. 29, p. 703-706.

Casquet, C., Rapela, C.W., Pankhurst, R.J., Baldo, E., Galindo, C., Fanning, C.M. and Dahlquist, J., 2012. Fast sediment underplating and essentially coeval juvenile magmatism in the Ordovician margin of Gondwana, Western Sierras Pampeanas, Argentina. Gondwana Research, 22(2), pp.664-673.

Chapman, A.D., Saleeby, J.B., and Eiler, J., 2013, Slab flattening trigger for isotopic disturbance and magmatic flare-up in the southernmost Sierra Nevada batholith, California. Geology, 41, 1007–1010.

Chapman, J.B., Ducea, M.N., Kapp P., Gehrels, G.E., DeCelles, P.G., 2017, Spatial and temporal radiogenic isotopic trends of magmatism in Cordillera orogens: Gondwana Research, v. 48, p. 189-204, doi: 10.1016/j.gr.2017.04.019.

Charrier, R., Ramos, V.A., Tapia, F. and Sagripanti, L., 2015. Tectono-stratigraphic evolution of the Andean Orogen between 31 and 37 S (Chile and Western Argentina). Geological Society, London, Special Publications, 399(1), pp.13-61.

Chen, Y.W., Wu, J. and Suppe, J., 2019. Southward propagation of Nazca subduction along the Andes. Nature, 565(7740), p.441.

Ciccioli, P.L., Limarino, C.O., Friedman, R. and Marenssi, S.A., 2014. New high precision U-Pb ages for the Vinchina Formation: implications for the stratigraphy of the Bermejo Andean foreland basin (La Rioja province, western Argentina). Journal of South American Earth Sciences, 56, pp.200-213.

Cina, S.E., Yin, A., Grove, M., Dubey, C.S., Shukla, D.P., Lovera, O.M., Kelty, T.K., Gehrels, G.E., and Foster, D.A., 2009, Gangdese arc detritus within the eastern Himalayan Neogene foreland basin: Implications for the Neogene evolution of the Yalu–Brahmaputra River system: Earth and Planetary Science Letters, v. 285, p. 150-162.

Coira, B. L., Davidson, J. D., Mpodozis, C. & Ramos, V. A. 1982. Tectonic and magmatic evolution of the Andes of Northern Argentina and Chile. Earth Science Reviews, 18, 303–332.

Collins, W.J., Belousova, E.A., Kemp A.I.S., Murphy, J.B., 2011, Two contrasting Phanerozoic orogenic systems revealed by hafnium isotopic data: Nature Geosciences, v. 4, p. 333-337.

Coney, P.J. and Reynolds, S.J., 1977. Cordilleran benioff zones. Nature, 270(5636), p.403.

Coney, P.J., Smith, R.B. and Eaton, G.P., 1978. Mesozoic-Cenozoic cordilleran plate tectonics. Cenozoic tectonics and regional geophysics of the western Cordillera: Geological Society of America Memoir, 152, pp.33-50.

Constenius, K.N., 1996. Late Paleogene extensional collapse of the Cordilleran foreland fold and thrust belt. Geological Society of America Bulletin, 108(1), pp.20-39.

Coutts, D.S., Matthews, W.A. and Hubbard, S.M., 2019. Assessment of widely used methods to derive depositional ages from detrital zircon populations. Geoscience Frontiers.

Craig H. Jones, G. Lang Farmer, Brad Sageman, Shijie Zhong; Hydrodynamic mechanism for the Laramide orogeny. Geosphere ; 7 (1): 183–201. doi: https://doi.org/10.1130/GES00575.1

Cristallini, E. O., and Ramos, V. A, 2000, Thick-skinned and thin-skinned thrusting in the La Ramada fold and thrust belt: crustal evolution of the High Andes of San Juan, Argentina (32°SL): Tectonophysics, v. 317(3–4), p. 205–235. http://doi.org/10.1016/S0040-1951 (99)00276-0

Currie, C.A., Beaumont, C. and Huismans, R.S., 2007. The fate of subducted sediments: A case for backarc intrusion and underplating. Geology, 35(12), pp.1111-1114.

Dahlquist J.A., Pankhurst, R.J., Gasching, R.M., Rapela, C.W., Casquet, C., Alasino, P.H., Galindo, C., and Baldo, E.G., 2013, Hf and Nd isotopes in Early Ordovician to Early Carboniferous granites as monitors of crustal growth in the Proto-Andean margin of Gondwana: Gondwana Research, v. 23, p. 1617-1630, doi: 10.1016/j.gr.2012.08.013.

Damanti, J.F., 1993, Geomorphic and structural controls on facies patterns and sediment composition in a modern foreland basin: in Marzo, M., Puigdefabregas, C., eds.,

International Association of Sedimentologists Special Publication, v. 17, p. 221-233.

Dávila, F.M. and Lithgow-Bertelloni, C., 2013. Dynamic topography in South America. Journal of South American Earth Sciences, 43, pp.127-144.Ramos et al., 1986;

Dávila, F.M., Lithgow-Bertelloni, C. and Giménez, M., 2010. Tectonic and dynamic controls on the topography and subsidence of the Argentine Pampas: The role of the flat slab. Earth and Planetary Science Letters, 295(1-2), pp.187-194.

DeCelles, P.G., and Hertel, F., 1989, Petrology of fluvial sands from the Amazonian foreland basin, Peru and Bolivia: Geological Society of America Bulletin, v. 101, p. 1552–1562.

DeCelles, P.G., Gray, M.B., Ridgway, K.D., Cole, R.B., Pivnik, D.A., Pequera, N. and Srivastava, P., 1991. Controls on synorogenic alluvial-fan architecture, Beartooth Conglomerate (Palaeocene), Wyoming and Montana. Sedimentology, 38(4), pp.567-590.

DeCelles, P.G., Zandt, G., Beck, S.L., Currie, C.A., Ducea, M.N., Kapp, P., Gehrels, G.E., Carrapa, B., and Quade, J., 2015, Cyclical orogenic processes in the Cenozoic central Andes. In P.G. DeCelles, M.N. Ducea, B. Carrapa, and P.A. Kapp, Eds., Geodynamics of a Cordilleran Orogenic System: The Central Andes of Argentina and Northern Chile. Geological Society of America Memoir, 212, 459–490. doi: 10 .1130/9780813712123.

Del Rey, A., Deckart, K., Arriagada, C. and Martínez, F., 2016. Resolving the paradigm of the late Paleozoic–Triassic Chilean magmatism: Isotopic approach. Gondwana Research, 37, pp.172-181.

Dickinson, W.R., 2008, Impact of differential zircon fertility of granitoid basement rocks in North America on age populations of detrital zircons and implications for granite petrogenesis: Earth and Planetary Science Letters, v. 275, p. 80-92.

Dickinson, W.R., and Gehrels, G.E., 2008, Sediment delivery to the Cordilleran foreland basin: Insights from U-Pb Ages of detrital zircons in Upper Jurassic and Cretaceous strata of the Colorado Plateau: American Journal of Science, v. 308, p. 1041-1082.

Dickinson, W.R., and Suczek, C.A., 1979, Plate tectonics and sandstone compositions: American Association of Petroleum Geologists Bulletin, v. 63, p. 2164-2182.

Dickinson, W.R., Klute, M.A., Hayes, M.J., Janecke, S.U., Lundin, M.A., and Olivares, M.D., 1988, Paleogeographic and paleotectonic setting of Laramide sedimentary basins in the central Rocky Mountains region: Geological Society of America Bulletin, v. 100, p. 1023-1039.

Dickinson, W.R., Snyder, 1978. Plate tectonics of the Laramide orogeny (Vol. 3, pp. 355-366). Matthews.Ramos et al., 2002

Ducea M.N., Otamendi, J.E., Bergantz, G., Stair, K.M., Valencia, V.A., and Gehrels, G., 2010, Timing constraints on building an intermediate plutonic arc crustal section: U-Pb zircon geochronology of the Sierra Valle Fertil-La Huerta, Famatinian arc, Argentina: Tectonics, v. 29, p. #-#,doi:10.1029/2009TC002615

Ducea, M.N., Otamendi, J.E., Bergantz, G., Stair, K.M., Valencia, V.A. and Gehrels, G.E., 2010. Timing constraints on building an intermediate plutonic arc crustal section: U-Pb zircon geochronology of the Sierra Valle Fértil–La Huerta, Famatinian arc, Argentina. Tectonics, 29(4).Thomas et al., 2015;

Ducea, M.N., Paterson, S.R. and DeCelles, P.G., 2015. High-volume magmatic events in subduction systems. Elements, 11(2), pp.99-104.

Faccenna, C., Oncken, O., Holt, A.F., and Becker, T.W., 2017, Initiation of the Andean orogeny by lower mantle subduction: Earth and Planetary Science Letters, v. 463, 189-201. DOI:10.1016/j.epsl.2017.01.041

Farías, M., Charrier, R., Carretier, S., Martinod, J., Fock, A., Campbell, D., Cáceres, J. and Comte, D., 2008. Late Miocene high and rapid surface uplift and its erosional response in the Andes of central Chile (33–35 S). Tectonics, 27(1).

Fernandez-Seveso, F. and Tankard, A.J., 1995. Tectonics and stratigraphy of the Late Paleozoic Paganzo Basin of Western Argentina and its regional implications.

Flaig, P.P., Fiorillo, A.R. and McCarthy, P.J., 2014. Dinosaur-bearing hyperconcentrated flows of Cretaceous arctic Alaska: recurring catastrophic event beds on a distal paleopolar coastal plain. Palaios, 29(11), pp.594-611.

Folguera, A., and Ramos, V.A., 2011, Repeated eastward shifts of arc magmatism in the Southern Andes: A revision to the long-term pattern of Andean uplift and magmatism: Journal of South American Earth Sciences, v. 32, p. 531–546.

Fosdick, J.C., Carrapa, B., and Ortíz, G., 2015, Faulting and erosion in the Argentine Precordillera during changes in subduction regime: reconciling bedrock cooling

and detrital records. Earth and Planetary Science Letters, v. 431, p. 73–83. http://doi.org/10.1016/j.epsl.2015.09.041

Fosdick, J.C., Reat, E.J., Carrapa, B., Ortiz, G. and Alvarado, P.M., 2017. Retroarc basin reorganization and aridification during Paleogene uplift of the southern central Andes. Tectonics, 36(3), pp.493-514.

Garzanti, E., Doglioni, C., Vezzoli, G., and Ando, S., 2007, Orogenic Belts and Orogenic Sediment Provenance, Journal of Geology, v. 115, p. 315–334.

Gehrels, G. 2000, Introduction to detrital zircon studies of Paleozoic and Triassic strata in western Nevada and northern California: ern Nevada and northern California, in Soreghan, M.J., and Gehrels, G.E., eds., Paleozoic and Triassic Paleogeography and Tectonics of Western Nevada and Northern California: Geological Society of America Special Paper 347, p. 1–17, doi:10.1130/0-8137-2347-7 .1.

Gehrels, G., 2014, Detrital zircon U-Pb geochronology applied to tectonics: Annual Review of Earth and Planetary Sciences, v. 42, p. 127–149.

Gurnis, M., 1992. Rapid continental subsidence following the initiation and evolution of subduction. Science, 255(5051), pp.1556-1558.

Gutscher, M.A., Maury, R., Eissen, J.P. and Bourdon, E., 2000. Can slab melting be caused by flat subduction?. Geology, 28(6), pp.535-538.

Hampton, B.A. and Horton, B.K., 2007. Sheetflow fluvial processes in a rapidly subsiding basin, Altiplano plateau, Bolivia. Sedimentology, 54(5), pp.1121-1148.

Hart, N.R., Stockli, D.F., and Hayman, N.W., 2016, Provenance evolution during progressive rifting and hyperextension using bedrock and detrital zircon U-Pb

geochronology, Mauléon Basin, western Pyrenees: Geosphere, doi:10.1130/GES01273.1.

Haschke, M., Günther, A., Melnick, D., Echtler, H., Reutter, K.J., Scheuber, E., Oncken, O., 2006, Central and southern Andean tectonic evolution inferred from arc magmatism. The Andes. Springer, Berlin Heidelberg, p. 337–353.

Haschke, M., Günther, A., Melnick, D., Echtler, H., Reutter, K.J., Scheuber, E. and Oncken, O., 2006. Central and southern Andean tectonic evolution inferred from arc magmatism. In The Andes (pp. 337-353). Springer, Berlin, Heidelberg.

Haschke, M., Siebel, W., Günther, A., and Scheuber, E., 2002, Repeated crustal thickening and recycling during the Andean orogeny in north Chile (21°–26°S): Journal of Geophysical Research: v. 107, article 2019, doi:10.1029/2001JB000328.

Heller, P.L. and Liu, L., 2016. Dynamic topography and vertical motion of the US Rocky Mountain region prior to and during the Laramide orogeny. GSA Bulletin, 128(5-6), pp.973-988.

Heller, P.L., Angevine, C.L., Winslow, N.S. and Paola, C., 1988. Two-phase stratigraphic model of foreland-basin sequences. Geology, 16(6), pp.501-504.

Heredia, N., Rodriguez-Fernandez, L.R., Gallastegui, G., Busquets, P. and Colombo F. , 2002, Geological setting of the Argentine Frontal Cordillera in the flat-slab segment (30°00'–31°30'S latitude), J. South Am. Earth Sci., v.15, p. 79–99.

Heredia, N., Rodriguez-Fernandez, L.R.,. Gallastegui, G., Busquets, P. and Colombo F. , 2002, Geological setting of the Argentine Frontal Cordillera in the flat-slab segment (30°00'–31°30'S latitude), J. South Am. Earth Sci., v.15, p. 79–99.

Hervé, F, Fanning, C.M., Calderon, M, Mpodozis, C., 2014, Early Permian to Late Triassic batholiths of the Chilean Frontal Cordillera (28-31 S): SHRIMP U-Pb zircon ages and Lu-Hf and O isotope systems: Lithos, v. 187, p. 436-446. doi: 10.1016/j.lithos.2013.10.018.

Hildreth,W., and Moorbath, S., 1988. Crustal contributions to arc magmatism in the Andes of central Chile. Contributions to Mineralogy and Petrology 98, 455–489.

Hilley, G. E., Strecker, M. R. & Ramos, V. A. 2004. Growth and erosion of fold-and-thrust belts with application to the Aconcagua fold-and-thrust belt, Argentina. Journal of Geophysical Research 109, B01410, doi: 10.1029/2002JB002282.

Hilley, G.E., Strecker, M.R. and Ramos, V.A., 2004. Growth and erosion of fold-and-thrust belts with an application to the Aconcagua fold-and-thrust belt, Argentina. Journal of Geophysical Research: Solid Earth, 109(B1).

Hoke, G. D., Graber, N. R., Mescua, J. F., Giambiagi, L.B., Fitzgerald, P.G., and Metcalf, J.R., 2015, Near pure surface uplift of the Argentine Frontal Cordillera: insights from (U–Th)/He thermochronometry and geomorphic analysis: Geological Society, London, Special Publications, v. 399, p.383-399.

Horton, B.K. and DeCelles, P.G., 1997. The modern foreland basin system adjacent to the Central Andes. Geology, 25(10), pp.895-898.

Horton, B.K. and DeCelles, P.G., 2001, Modern and ancient fluvial megafans in the foreland basin system of the central Andes, southern Bolivia: implications for drainage network evolution in fold-thrust belts: Basin Research, v. 13, p. 43–63.

Horton, B.K. and DeCelles, P.G., 2001. Modern and ancient fluvial megafans in the foreland basin system of the central Andes, southern Bolivia: Implications for drainage network evolution in foldthrust belts. Basin research, 13(1), pp.43-63.

Horton, B.K., 2012, Cenozoic evolution of hinterland basins in the Andes and Tibet, in Busby, C., and Azor, A., eds., Tectonics of Sedimentary Basins: Recent Advances: Wiley-Blackwell, Oxford, UK, p. 427–444.

Horton, B.K., 2018a. Tectonic regimes of the central and southern Andes: Responses to variations in plate coupling during subduction: Tectonics, v. 37, p. 402-429. doi: /10.1002/2017TC004624.

Horton, B.K., 2018b, Sedimentary record of Andean mountain building: Earth Science Reviews, v. 178, p. 279-309, doi:10.1016/j.earscirev.2017.11.025.

Horton, B.K., and DeCelles, P.G., 2001, Modern and ancient fluvial megafans in the foreland basin system of the central Andes, southern Bolivia: implications for drainage network evolution in fold-thrust belts, v.13, p.43-63.

Horton, B.K., and Fuentes, F., 2016, Sedimentary record of plate coupling and decoupling during growth of the Andes: Geology, v. 44, p. 647-650, doi:10.1130/G37918.1.

Horton, B.K., Anderson, V.J., Caballero, V., Saylor, J.E., Parra, M., and Mora, A., 2015b, Application of detrital zircon U-Pb geochronology to surface and subsurface correlations of provenance, paleodrainage, and tectonics of the Middle Magdalena Valley Basin of Colombia: Geosphere, v. 11, doi:10.1130/GES01251.1.

Horton, B.K., Fuentes, F., Boll, A., Starck, D., Ramirez, S.G., and Stockli, D.F., 2016, Andean stratigraphic record of the transition from backarc extension to orogenic

shortening: A case study from the northern Neuquén basin, Argentina. Journal of South American Earth Sciences, v. 71, 17-40.

Horton, B.K., Perez, N.D., Fitch, J.D., and Saylor, J.E., 2015a, Punctuated shortening and subsidence in the Altiplano plateau of southern Peru: Implications for early Andean mountain building: Lithosphere, v. 7, p. 117–137, doi:10.1130/L397.1.

Humphreys, E.D., 1995. Post-Laramide removal of the Farallon slab, western United States. Geology, 23(11), pp.987-990.

Ingersoll, R.V., 1990, Actualistic sandstone petrofacies: Discriminating modern and ancient source rocks: Geology, v. 18, p. 733–736.

Ingersoll, R.V., Kretchmer, A.G., and Valles, P.K., 1993, The effect of sampling scale on actualistic sandstone petrofacies: Sedimentology, v. 40, p. 937–953.

Irigoyen, M.V., Buchan, K.L., and Brown, R.L., 2000, Magnetostratigraphy of Neogene Andean foreland-basin strata, lat 33°S , Mendoza Province, Argentina, GSA Bulletin, v.112, p.803-816.

Jara, P., Charrier, R., 2014. Nuevos antecedentes estratigráficos y geocronológicos para el Meso-Cenozoico de la Cordillera Principal de Chile entre 32° y 32°30'S: Implicancias estructurales y paleogeográficas. Andean Geol. 41, 174–209. https://doi.org/10.5027/andgeoV41n1-a07

Johnson, M.N., Jordan, T.E., Johnson, P.A., and Naeser, C.W., 1986, Magnetic polarity stratigraphy, age, and tectonic setting of fluvial sediments in an eastern Andean foreland basin, San Juan Province, Argentina, in Allen, P., and Homewood, P., eds., Foreland Basins: IAS Spec. Pub.v.8, p.63-75.

Johnsson, M.J., 1993, The system controlling the composition of clastic sediments, in Johnsson, M., and A., B., eds., Processes Controlling the Composition of Clastic Sediments: Geological Society of America, v. 284, p. 1-19.

Jones, R.E., Kirstein, L.A., Kasemann, S.A., Dhuime, B., Elliott, T., Litvak, V.D., Alonso, R.N., and Hinton, R., 2015, Geodynamic controls on the contamination of Cenozoic arc magmas in the southern Central Andes: Insights from the O and Hf isotopic composition of zircon: Geochimica et Cosmochimica Acta, v. 164, p. 386-402. http://dx.doi.org/10.1016/j.gca.2015.05.007

Jordan, T.E. and R.W. Allmendinger (1986), The Sierras Pampeanas of Argentina: A modern analogue of Rocky Mountain foreland deformation: American Journal of Science, v. 286, p. 737-764.

Jordan, T.E., 1995, Retroarc foreland and related basins, in Busby, C.J., and Ingersoll, R.V., eds., Tectonics of sedimentary basins: Cambridge, Massachusetts, Blackwell Science, p. 331–362.

Jordan, T.E., Allmendinger, R.W., Damanti, J.F., and Drake, R.E., 1992, Chronology of Motion in a complete thrust belt: The Precordillera 30-31°S, Andes Mountains, Journal of Geology, v. 101, p.135-156.

Jordan, T.E., Rutty, P.M., McRae, L.E., Beer, J.A., Tabbutt, K., and Damanti, J.F., 1990, Magnetic polarity stratigraphy of the Miocene Rio Azul section Precordillera thrust belt, San Juan Province, Argentina, Journal of Geology, v.98, p.519-539.

Jordan, T.E., Schlunegger, F., and Cardozo, N., 2001, Unsteady and spatially variable evolution of the Neogene Andean Bermejo foreland basin, Argentina: Journal of South American Earth Sciences, v. 14, p. 775-798.

Jordan, T.E., Tamm, V., Figueroa, G., Flem-Dog, M, Richards, P.B., Tabbutt, K., Cheatham, T., 1996, Development of the Miocene Manantiales foreland basin, Principal Cordillera, San Juan, Argentina, Revista Geologica de Chile, v. 23, p.43-79.

Karlstrom, L., Lee, C.-T.A., Manga, M., 2014, The role of magmatically driven lithospheric thickening on arc front migration: Geochem. Geophys. Geosyst., v.15, p. 2655-2675. Doi:10.1002/2014GC005355.

Kay, S.M., and Mpodozis, C., 2002, Magmatism as a probe to the Neogene shallowing of the Nazca plate beneath the modern Chilean flat-slab: Journal of South American Earth Sciences, v. 15, p. 39-57.

Kay, S.M., Godoy, E. and Kurtz, A., 2005. Episodic arc migration, crustal thickening, subduction erosion, and magmatism in the south-central Andes. Geological Society of America Bulletin, 117(1-2), pp.67-88.

Kay, S.M., Maksaev, V., Moscoso, R., Mpodozis, C. and Nasi, C., 1987. Probing the evolving Andean Lithosphere: Mid-Late Tertiary magmatism in Chile (29°–30° 30′ S) over the modern zone of subhorizontal subduction. Journal of Geophysical Research: Solid Earth, 92(B7), pp.6173-6189.

Kay, S.M., Mpodozis, C., Ramos, V.A. and Munizaga, F., 1991. Magma source variations for mid-late Tertiary magmatic rocks associated with a shallowing subduction zone

and a thickening crust in the central Andes (28 to 33 S). Geological Society of America Special Paper, 265, pp.113-137.

Kay, S.M., Orrell, S. and Abbruzzi, J.M., 1996. Zircon and whole rock Nd-Pb isotopic evidence for a Grenville age and a Laurentian origin for the basement of the Precordillera in Argentina. The Journal of Geology, 104(6), pp.637-648.

Keppie, D.F., Currie, C.A. and Warren, C., 2009. Subduction erosion modes: comparing finite element numerical models with the geological record. Earth and Planetary Science Letters, 287(1-2), pp.241-254.

Kirkland, C.L., Smithies, R.H., Taylor, R.J.M., Evans, N. and McDonald, B., 2015. Zircon Th/U ratios in magmatic environs. Lithos, 212, pp.397-414.

Kirsch, M., Paterson, S.R., Wobbe, F., Ardila, A.M.M., Clausen, B.L. and Alasino, P.H., 2016. Temporal histories of Cordilleran continental arcs: Testing models for magmatic episodicity. American Mineralogist, 101(10), pp.2133-2154.

Kirsch, M., Paterson, S.R., Wobbe, F., Martinez-Ardila, A.M., Clausen, B.L., and Alasino, P.H., 2016, Temporal histories of Cordillera continental arcs: Testing models for magmatic episodicity. American Mineralogist, v. 101, p. 2133-2154.

Kleiman, L. E., and Japas, M. S., 2009, The Choiyoi volcanic province at 34°S-36°S (San Rafael, Mendoza, Argentina): Implications for the Late Paleozoic evolution of the southwestern margin of Gondwana: Tectonophysics, 473(3–4), 283–299. http://doi.org/10.1016/j.tecto.2009.02.046

Kleiman, L.E., and Japas, M.S., 2009, The Choiyoi volcanic province at 34 S–36 S (San Rafael, Mendoza, Argentina): Implications for the Late Paleozoic evolution of the southwestern margin of Gondwana: Tectonophysics, v. 473, p.283–299.

Levina, M., Horton, B.K., Fuentes, F., and Stockli, D.F., 2014, Cenozoic sedimentation and exhumation of the foreland basin system preserved in the Precordillera thrust belt (31-32°S), southern central Andes, Argentina: Tectonics, v. 33, p. 1659-1680.

Limarino, C., Net, L., Gutiérrez, P., Barreda, V., Caselli, A. and Ballent, S., 2000. Definición litoestratigráfica de la Formación Ciénaga del Río Huaco (Cretácico Superior), Precordillera central, San Juan, Argentina. Revista de la Asociación Geológica Argentina, 55(1), pp.83-99.

Limarino, C.O., Césari, S.N., Net, L.I., Marenssi, S.A., Gutierrez, R.P. and Tripaldi, A., 2002. The Upper Carboniferous postglacial transgression in the Paganzo and Rıo Blanco basins (northwestern Argentina): facies and stratigraphic significance. Journal of South American Earth Sciences, 15(4), pp.445-460.

Litvak, V.D., Poma, S. and Kay, S.M., 2007. Paleogene and Neogene magmatism in the Valle del Cura region: new perspective on the evolution of the Pampean flat slab, San Juan province, Argentina. Journal of South American Earth Sciences, 24(2-4), pp.117-137.

Llambias, E.J. and Sato, A.M., 1990. El Batolito de Colangüil (29-31° S) cordillera frontal de Argentina: estructura y marco tectonico. Andean Geology, 17(1), pp.89-108.

Mackaman-Lofland, C., Horton, B.K., Fuentes, F., Constenius, K.C., McKenzie, N.R., and Alvarado, P.M., 2015, Preliminary depositional and provenance records of

Mesozoic basin evolution and Cenozoic shortening in the High Andes, La Ramada fold-thrust belt, southern-central Andes (32-33°S): American Geophysical Union Fall Meeting.

Mackaman-Lofland, C., Horton, B.K., Fuentes, F., Constenius, K.N. and Stockli, D.F., 2019. Mesozoic to Cenozoic retroarc basin evolution during changes in tectonic regime, southern Central Andes (31–33° S): Insights from zircon U-Pb geochronology. Journal of South American Earth Sciences, 89, pp.299-318.

Maloney, K.T., Geoffrey, L.C., Klepeis, K.A., Quevedo, L., 2013, The Late Jurassic to present evolution of the Andean margin: Drivers and the geologic record: Tectoincs, v. 32, p. 1049-1065, doi:10.1002/tect.200067

Malusà, M.G., Resentini, A., and Garzanti, E., 2016, Hydraulic sorting and mineral fertility bias in detrital geochronology: Gondwana Research, v. 31, p. 1–19.

Maydagán, L., Franchini, M., Chiaradia, M., Pons, J., Impiccini, A., Toohey, J., Rey, R., 2011, Petrology of the Miocene igneous rocks in the Altar region, main Cordillera of San Juan, Argentina. A geodynamic model within the context of the Andean flat-slab segment and metallogenesis: Journal of South American Earth Sciences, v. 32, p. 30-48.

McKay, M.P., Jackson, W.T., Hessler, A.M., 2018, Tectonic stress regime recorded by zircon Th/U: Gondwana Research, v. 57, p. 1-9.

McKenzie, N. R., Hughes, N. C., Myrow, P. M., Banerjee, D. M., Deb, M., and Planavsky, N. J., 2013, New age constraints for the Proterozoic Aravalli–Delhi successions of India and their implications: Precambrian Research, v. 238, p. 120-128.

McKenzie, N.R., Horton, B.K., Loomis, S.E., Stockli, D.F., Planavsky, N.J., and Lee, C.-T.A., 2016, Continental arc volcanism as the principal driver of icehouse-greenhouse variability: Science, v. 352 (6284), p. 444-447, doi:10.1126/science.aad5787.

McKenzie, N.R., Horton, B.K., Loomis, S.E., Stockli, D.F., Planavsky, N.J., Lee, C.-T.A., 2016, Continental arc volcanism as the principal driver of icehouse–greenhouse variability: Science, v. 352 (6284), p.444–447, doi:10.1126/science.aad5787.

McLaurin, B.T. and Steel, R.J., 2007. Architecture and origin of an amalgamated fluvial sheet sand, lower Castlegate Formation, Book Cliffs, Utah. Sedimentary Geology, 197(3-4), pp.291-311.

Miall, A.D., 1977. A review of the braided-river depositional environment. Earth-Science Reviews, 13(1), pp.1-62.

Miall, A.D., 1985. Architectural-element analysis: a new method of facies analysis applied to fluvial deposits. Earth-Science Reviews, 22(4), pp.261-308.

Milana, J.P. and Ruzycki, L., 1999. Alluvial-fan slope as a function of sediment transport efficiency. Journal of Sedimentary Research, 69(3), pp.553-562.

Miliana, J.P., Bercowski, F., and Jordan, T.E., 2003, Paleoambientes y magnetoestrigrafia del Neogeno de la Sierra de Mogna, y su relacion con la Cuenca de Antepais Andina, Revista de la Associacion Geologica Argentina, v. 38, p. 447-473.

Moecher, D.P., and Samson, S.D., 2006, Differential zircon fertility of source terranes and natural bias in the detrital zircon record: Implications for sedimentary provenance analysis: Earth and Planetary Science Letters, v. 247, p. 252-266.

Mpodozis, C. and Kay S.M., 1992, Late Paleozoic to Triassic evolution of the Gondwana margin: Evidence from Chilean Frontal Cordilleran batholiths (28 to 31 S): Geological Society of America Bulletin, v. 104, p. 999-1014.

Mpodozis, C. and Kay, S.M., 1992. Late Paleozoic to Triassic evolution of the Gondwana margin: Evidence from Chilean Frontal Cordilleran batholiths (28 S to 31 S). Geological Society of America Bulletin, 104(8), pp.999-1014.

Mpodozis, C., and Ramos, V.A., 1990, The Andes of Chile and Argentina, in Ericksen, G.E., Cañas Pinochet, M.T., and Reinemund, J.A., eds., Geology of the Andes and its Relation to Hydrocarbon and Mineral Resources: Circum-Pacific Council for Energy and Mineral Resources, Earth Science Series, v. 11, p. 59–90.

Mpodozis, C., Kay, S.M., 1992. Late Paleozoic to Triassic evolution of the Gondwana margin: evidence from Chilean Frontal Cordilleran batholiths (28° to 31° S): Geological Society of America Bulletin v.104, p. 999–1014.

Mulcahy, S.R., Roeske, S.M., McClelland, W.C., Jourdan, F., Iriondo, A., Renne, P.R., Vervoort, J.D., and Vujovich, G.L., 2011, Structural evolution of a composite middle to lower crustal section: The Sierra de Pie de Palo, northwest Argentina: Tectonics, v. 30, TC1005, doi:10.1029/2009TC002656.

Oliveros, V., González, J., Vargas, M.E., Vásquez, P., Rossel, P., Creixell, C., Sepúlveda, F. and Bastias, F., 2018. The Early Stages of the Magmatic Arc in the Southern Central Andes. In The Evolution of the Chilean-Argentinean Andes p. 165-190). Springer, Cham.

Ortiz, G., Alvarado, P., Fosdick, J. C., Perucca, L., Saez, M., and Venerdini, A., 2015, Active deformation in the northern Sierra de Valle Fértil, Sierras Pampeanas, Argentina: Journal of South American Earth Sciences, v. 64, p. 339–350. http://doi.org/10.1016/j.jsames.2015.08.015

Otamendi, J.E., Ducea, M.N., Cristofolini, E.A., Tibaldi, A.M., Camilletti, G.C. and Bergantz, G.W., 2017. U-Pb ages and Hf isotope compositions of zircons in plutonic rocks from the central Famatinian arc, Argentina. Journal of South American Earth Sciences, 76, pp.412-426.

Parada, M.A., Nyström, J.O. and Levi, B.E.A.T.R.I.Z., 1999. Multiple sources for the Coastal Batholith of central Chile (31–34 S): geochemical and Sr–Nd isotopic evidence and tectonic implications. Lithos, 46(3), pp.505-521.

Paterson, S.R. and Ducea, M.N., 2015. Arc magmatic tempos: gathering the evidence. Elements, 11(2), pp.91-98.

Pepper, M.B., Gehrels, G., Pullen, A., Ibanez-Mejia, M., Ward, K.M., and Kapp, P., 2016, Magmatic history and crustal genesis of South America: Constraints from U-Pb Ages and Hf isotopes of detrital zircons in modern rivers: Geosphere, v. 12, p. 1532–1555, doi: 10 .1130 /GES01315 .1.

Pilger, R. , 2018, Radiometric Dates from the Andes - Pentecost 2018 – Link.

Ramos, V. A., 1999, Plate tectonic setting of the Andean Cordillera: Episodes, v. 22(3), p. 183–190.

Ramos, V. A., Aguierre Urreta, M. B. ET AL. 1996a. Geologı´a de la Regio´n del Aconcagua, Provincias de San Juan y Mendoza. Direccio´n Nacional del Servicio Geolo´gico, Anales, 24, 1–510.

Ramos, V. A., and A. Folguera (2009), Andean flat-slab subduction through time, Geol. Soc. Lond. Spec. Publ., 327 (1), 31–54, doi:10.1144/SP327.3.

Ramos, V.A. and Folguera, A., 2009. Andean flat-slab subduction through time. Geological Society, London, Special Publications, 327(1), pp.31-54.

Ramos, V.A. and Kay, S.M., 1991. Triassic rifting and associated basalts in the Cuyo basin, central Argentina. In Andean magmatism and its tectonic setting (Vol. 265, pp. 79-91). Boulder: Geological Society of America.

Ramos, V.A., 2009, Anatomy and global context of the Andes: Main geologic features and the Andean orogenic cycle, in Kay, S.M., Ramos, V.A., and Dickinson, W.R., eds., Backbone of the Americas: Shallow subduction, plateau uplift, and ridge and terrane collision: Geological Society of America Memoir, v. 204, p. 31-65.

Ramos, V.A., 2009, Anatomy and global context of the Andes: Main geologic features and the Andean orogenic cycle: Geological Society of America Memoirs, v. 204, p. 31-65, doi: 10.1130/2009.1204 (02)

Ramos, V.A., Cristallini, E.O, and Perez, D.J., 2002, The Pampean flat-slab of the Central Andes: Journal of South American Earth Sciences, v. 15, p. 59-78.

Ramos, V.A., Cristallini, E.O. and Pérez, D.J., 2002. The Pampean flat-slab of the Central Andes. Journal of South American earth sciences, 15(1), pp.59-78.

Ramos, V.A., Cristallini, E.O., and Perez, D.J., 2002, The Pampean flat-slab of the Central Andes: Journal of South American Earth Sciences, v. 15, p. 59-78.

Ramos, V.A., Kay, S.M., Page, R. and Munizaga, F., 1989. La ignimbrita Vacas Heladas y el cese del volcanismo en el Valle del Cura, Provincia de San Juan. Revista de la Asociación Geológica Argentina, 44(1-2), pp.336-352.

Ramos, V.A., Litvak, V.D., Folguera, A., and Spagnuolo, M., 2014, An Andean tectonic cycle: From crustal thickening to extension in a thin crust (34°–37°SL): Geoscience Frontiers, v. 5, p. 351–367, doi:10.1016/j.gsf.2013.12.009.

Rapela, C.W., Verdecchia, S.O., Casquet, C., Pankhurst, R.J., Baldo, E.G., Galindo, C., Murra, J.A., Dahlquist, J.A., Fanning, C.M., 2016. Identifying Laurentian and SW Gondwana sources in the Neoproterozoic to Early Paleozoic metasedimentary rocks of the Sierras Pampeanas: Paleogeographic and tectonic implications. Gondwana Res. 32, 193-201.

Reat, E.J. and Fosdick, J.C., 2018. Basin evolution during Cretaceous-Oligocene changes in sediment routing in the Eastern Precordillera, Argentina. Journal of South American Earth Sciences, 84, pp.422-443.

Regnier, M., Chatelain, J.L., Smalley Jr, R., Chiu, J.M., Isacks, B.L. and Araujo, M., 1992. Seismotectonics of Sierra Pie de Palo, a basement block uplift in the Andean foreland of Argentina. Bulletin of the Seismological Society of America, 82(6), pp.2549-2571.

Reynolds, J.H., Jordan, T.E., Johnson, N. M., Damanti, J.F., and Tabbutt, K.D., 1990, Neogene deformation of the flat-subduction segments of the Argentine-Chilean

Andes: Magnetostratigraphic constraints from Las Juntas, La Rioja province, Argentina, Geological society of America Bulletin, v.102, p.1607-1622.

Rivano, S., Sepúlveda, P., Boric, R., Espiñeira, D., 1993. Hoja Quillota y Portillo. V Región. Mapa escala 1:250,000

Roberts, N.M. and Spencer, C.J., 2015. The zircon archive of continent formation through time. Geological Society, London, Special Publications, 389(1), pp.197-225.

Rolleri, E. O., and Criado Roque, P., 1968, La cuenca triásica del Norte de Mendoza: in Actas Terceras Jornadas Geológicas Argentinas, Buenos Aires: Asociación Geológica Argentina, v. 1, p. 1-76.

Romans, B.W., Castelltort, S., Covault, J.A., Fildani, A., and Walsh, J.P., 2016, Environmental signal propagation in sedimentary systems across timescales: Earth-Science Reviews, v. 153, p.

Satkoski, A. M., Wilkinson, B. H., Hietpas, J., and Samson, S. D., 2013, Likeness among detrital zircon populations — An approach to the comparison of age frequency data in time and space: Geological Society of America Bulletin, v.125, p.1783–1799. http://doi.org/10.1130/B30888.1

Sato, A.M., Llambías, E.J., Basei, M.A. and Castro, C.E., 2015. Three stages in the Late Paleozoic to Triassic magmatism of southwestern Gondwana, and the relationships with the volcanogenic events in coeval basins. Journal of South American Earth Sciences, 63, pp.48-69.

Saylor, J. E., and Sundell, K. E., 2016, Quantifying comparison of large detrital geochronology data sets: Geosphere, v. 12, p. 203–220. http://doi.org/10.1130/GES01237.1

Saylor, J.E., Knowles, J.N., Horton, B.K., Nie, J., and Mora, A., 2013, Mixing of source populations recorded in detrital zircon U-Pb age spectra from modern river sands: Journal of Geology, v. 121, p. 17-33.

Schellart, W.P., 2017, Andean mountain building and magmatic arc migration driven by subduction-induced whole mantle flow, Nature Communications, v. 8, DOI: 10.1038/s41467-017-01847-z

Schwartz, J.J., Gromet, L.P., and Miro, R., 2008, Timing and Duration of the Calc-Alkaline Arc of the Pampean Orogeny: Implications for the Late Neoproterozoic to Cambrian Evolution of Western Gondwana: Journal of Geology, v. 116, p. 39-61, DOI: 10.1086/524122

SEGEMAR, 1999, Geologia Argentina, scale 1:3,000,000, version digital en CD-ROM.

SEGEMAR, 2012. Sistema de Información Geográfica del Servicio Geológico Minero Argentino [WWW Document] (URL sig.segemar.gov.ar).

Sernageomin, 2003. Mapa geologico de chile: version digital. Mapa escala 1:1,000,000. Publ. Geol. Digit. 4, 25.

Smith, G.A. and Lowe, D.R., 1991. Lahars: Volcano hydrologic-events and deposition in the debris flow—Hyperconcentrated flow continuum.

Snyder, D.B., Ramos, V.A. and Allmendinger, R.W., 1990. Thick-skinned deformation observed on deep seismic reflection profiles in western Argentina. Tectonics, 9(4), pp.773-788.

Stazzere, L., Gregori, D.A., and Dristas J.A., 2006, Genetic evolution of Permo-Triassic volcaniclastic sequences at Uspallata, Mendoza Precordillera, Argentina: Gondwana Research, v. 9, p. 485-499.

Steel, R.J., Næhle, S., Nilsen, H., Røe, S.L. and Spinnangr, A., 1977. Coarsening-upward cycles in the alluvium of Hornelen Basin (Devonian) Norway: Sedimentary response to tectonic events. Geological Society of America Bulletin, 88(8), pp.1124-1134.

Stevens Goddard, A.L. and Carrapa, B., 2018. Using basin thermal history to evaluate the role of Miocene–Pliocene flat-slab subduction in the southern Central Andes (27° S–30° S). Basin Research, 30(3), pp.564-585.

Thomas, W.A, Astini, R. A., Mueller, P.A., and McClelland, W., 2015, Detrital-zircon geochronology and provenance of the Ocloyic synorogenic clastic wedge, and Ordovician accretion of the Argentine Precordillera terrane: Geosphere, v. 11, p. 1749-1769, doi:10.1130/GES01212.1.

Tripaldi, A. and Limarino, C.O., 2005. Vallecito Formation (Miocene): The evolution of an eolian system in an Andean foreland basin (northwestern Argentina). Journal of South American Earth Sciences, 19(3), pp.343-357.

Uliana, M.A., and Biddle, K.T., 1988, Mesozoic–Cenozoic paleogeographic and geodynamic evolution of southern South America: Revista Brasileira de Geociencias, v. 18, p. 172–190.

Val, P., Hoke, G.D., Fosdick, J.C. and Wittmann, H., 2016. Reconciling tectonic shortening, sedimentation and spatial patterns of erosion from 10Be paleo-erosion rates in the Argentine Precordillera. Earth and Planetary Science Letters, 450, pp.173-185.

Verges, J., Ramos, E, Seward, D., Busquets, P., Colombo, F., 2001, Miocene sedimentary and tectonic evolution of the Andean Precordillera at 31°S, Argentina, Journal of South American Earth Sciences, v. 14, p. 735-750.

Vermeesch, P., 2012. On the visualisation of detrital age distributions. Chemical Geology, 312, pp.190-194.

von Gosen, W., 1992, Structural evolution of the Argentine Precordillera: The Rio San Juan section: Journal of Structural Geology, v. 6, p. 643-667.

Von Gosen, W., 1992. Structural evolution of the argentine precordillera: The Río San Juan section. Journal of Structural Geology, 14(6), pp.643-667.

Vujovich, G.I., van Staal, C.R., and Davis, W., 2004, Age constraints on the tectonic evolution and provenace of the Pie de Palo complex, Cuyania composite terrane, and the Famatinian orogeny in the Sierra de Pie de Palo, San Juan, Argentina: Gondwana Research, v. 7, p. 1041-1056.

Wiedenbeck, M.A.P.C., Alle, P., Corfu, F., Griffin, W.L., Meier, M., Oberli, F.V., Quadt, A.V., Roddick, J.C. and Spiegel, W., 1995. Three natural zircon standards for U-

Th-Pb, Lu-Hf, trace element and REE analyses. Geostandards newsletter, 19(1), pp.1-23.

Xia, X., Sun, M., Geng, H., Sun, Y., Wang, Y. and Zhao, G., 2011. Quasi-simultaneous determination of U-Pb and Hf isotope compositions of zircon by excimer laser-ablation multiple-collector ICPMS. Journal of Analytical Atomic Spectrometry, 26(9), pp.1868-1871.

Yakymchuk, C., Kirkland, C.L. and Clark, C., 2018. Th/U ratios in metamorphic zircon. Journal of Metamorphic Geology, 36(6), pp.715-737.

Yáñez, G.A., Ranero, C.R., Huene, R. and Díaz, J., 2001. Magnetic anomaly interpretation across the southern central Andes (32–34 S): The role of the Juan Fernández Ridge in the late Tertiary evolution of the margin. Journal of Geophysical Research: Solid Earth, 106(B4), pp.6325-6345.

Zapata, T.R. and R. W. Allmendinger (1996), Thrust-front zone of the Precordillera, Argentina: a thick-skinned triangle zone, AAPG Bull., 80, 359-381.

Zhang, J.Y., Yin, A., Liu, W.C., Ding, L., and Xu, X.M., 2016, First geomorphological and sedimentological evidence for the combined tectonic and climate control on Quaternary Yarlung river diversion in the eastern Himalaya: Lithosphere, v. 8, p. 293-316

Zhang, J.Y., Yin, A., Liu, W.C., Wu, F.Y., Ding, L., and Grove, M., 2012, Coupled U-Pb dating and Hf isotopic analysis of detrital zircon of modern river sand from the Yalu River (Yarlung Tsangpo) drainage system in southern Tibet: Constraints on the

transport processes and evolution of Himalayan rivers: Geological Society of America Bulletin, v. 124, p. 1449-1473.